POLITECNICO DI MILANO

Dipartimento di Ingegneria Civile, Ambientale e Territoriale

Corso di Laurea Magistrale in Ingegneria Civile
Orientamento Idraulica

FLUID STRUCTURE SIMULATION FOR THE ASSESSMENT OF ACOUSTIC IMPEDANCE IN FLUID-SOLID SYSTEMS

Relatore :
Prof. Ing. Giuseppe Passoni
Correlatore :
Dott. Ing. Silvia Bozzi

Studente:
Marco Marcon
matr. 802486

Anno Accademico 2013 – 2014

Ai miei genitori

Abstract

This thesis is part of a study with the purpose of designing a technology for underground inspections based on acoustic imaging. A membrane situated in a borehole excavated at high depth in the underground generates pressure signals and detects with sensors the reflected waves travelling backward from the ground. Once the soil acoustic parameters, as well as the amplitudes of those reflected wavelets and their time of travelling are known, the geologic conformation of the inspected ground portion can be reconstructed.
Since my working period started in the preliminary phase of this entire study, a basic acoustic parameter, the acoustic impedance, had to be inspected.
The method of evaluation adopted in this work aims to be applicable in a large variety of engineering problems where the internal structure of materials needs to be inspected in a non-destructive way.
The first part of this thesis deals with the target of identifying the best software for the Fluid-Structure Interaction (FSI) numerical calculations. This is necessary for the correct modeling of the motional response to defined stresses configurations for the solid and fluid matrices.
An exact analytical solution has been used as a test case for the comparison of different FSI solvers, looking for the one who best fitted this known solution.
After that, given the complexity of the simulation domain and the number of factors composing the problem, it has been decided to analyze the influence of simpler models on the desired parameter of the acoustic impedance.
Some representative fluid geometries have been recreated with basic singularities. Given input signals have been tested with the aim of detecting the impedance of precise sections before and after those configurations.
Those fluid domains, in a preliminary phase, have been surrounded by a rigid body fully constraining the interface between the two media and not reacting to the fluid stress waves. Analysis on fluid pressure and velocity fields have been useful in order to understand the behavior of those models to pressure wave solicitations.
Impedance characterization of fixed sections has been performed and compared with some theoretical acoustics cases to prove their validity.
Then, the rigid boundary has been substituted by a linear elastic solid rock reacting to fluid stresses through a contact interface.
FSI simulations have been conducted on the same domains analyzed in the previous part. However, in order to catch the reactions of the solid phase to the fluid stresses, the single fluid domain was charged in the inlet surface.
Results for the fluid phase have been compared with those obtained in the previous part, noticing some different factors affecting the FSI solution.
In the final section of this thesis, different boundary conditions have been imposed on the solid input section with the aim of studying the different influences they had on the stresses propagation fields both in the solid and the fluid domains.
These last considerations permitted some useful insights for the following parts of the entire study, connecting this work with the rest of the analysis.

Estratto in italiano

In molti campi dell'ingegneria è possibile dover affrontare la necessità di operare con strutture la cui conformazione non è omogenea, e può risultare composta da diversi materiali o da diverse fasi in contatto tra loro. Frequentemente l'alternarsi di queste parti non è distinguibile ad una prima analisi e richiede quindi l'utilizzo di metodi speciali per la loro identificazione.
È di fondamentale importanza ad esempio, in molte applicazioni dell'ingegneria geotecnica o strutturale, conoscere le proprietà di materiali, come il calcestruzzo armato o semplicemente il terreno, per poterne riconoscere le capacità di resistenza a determinati sforzi. La loro micro-struttura porosa e l'impossibilità di prelevarne dei campioni rappresentativi in molti casi necessita di prove non distruttive per poterne riconoscere le proprietà effettive. Una tipologia di queste prove può riguardare l'analisi della propagazione di onde sonore all'interno di questi materiali, dei quali può quindi essere necessario conoscerne le principali caratteristiche acustiche.
Non solo, metodi di ispezione tramite segnali acustici sono utilizzati all'interno di altri campi dell'ingegneria come quella meccanica o quella acustica. Per l'individuazione di difetti all'interno di materiali metallici in fase di produzione o in fase di monitoraggio, l'analisi della propagazione di segnali predefiniti può determinare la presenza di imperfezioni che riducono le capacità portanti della struttura. Lo studio dei segnali non è tuttavia utilizzato solamente in fase di controllo, bensì anche in fase di progettazione, come può capitare durante la creazione di materiali fonoassorbenti.
Nel caso di questo studio, il dominio in questione è rappresentato da una porzione di terreno situato in profondità, di cui quindi risulta impossibile o estremamente costoso estrarne un campione per lo studio della sua composizione. L'indagine, tramite strumenti dotati di tecnologia per l'emissione di onde di pressione e il rilevamento delle conseguenti onde riflesse, risulta di conseguenza necessaria per l'individuazione di particolari formazioni sotterranee. Queste possono essere ad esempio giacimenti petroliferi o altre singolarità che possono essere rilevate come deviazioni dalla prevista propagazione di un prefissato segnale.
Per la progettazione di tali strumenti e la loro corretta interpretazione dei dati è necessario conoscere le caratteristiche acustiche di un campione di terreno. Una grandezza fondamentale per la caratterizzazione acustica di un materiale è l'impedenza acustica, e la sua valutazione, attraverso un'analisi della sua struttura complessa rappresentata nella formula sottostante, è affrontabile tramite diversi metodi.

$$z = \frac{\hat{p}}{\hat{v}} = r + ix$$

La simulazione numerica di domini complessi, come può essere ad esempio un campione di terreno poroso, comporta lunghi tempi di calcolo e una notevole difficoltà di interpretazione dei risultati, data la grande quantità di fattori che intervengono alla sua formazione.

Per questi motivi, in questo lavoro, è stato deciso di scomporre il problema in casi elementari ma rappresentativi di ciò che può accadere all'interno di uno di questi domini in seguito all'applicazione di un onda di pressione.

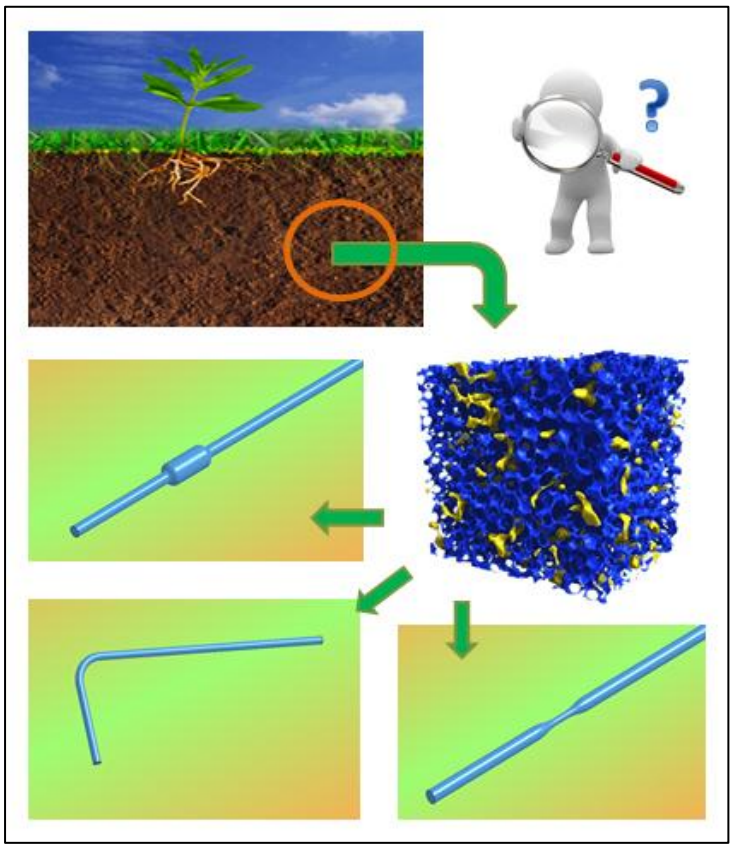

Estrazione di geometrie elementari dal dominio complesso rappresentato dal campione di terreno poroso.

Con questo obiettivo sono state modellate delle particolari geometrie, rappresentanti configurazioni topologiche di base, la cui analisi è stata effettuata tramite una successiva addizione di complessità al problema più semplice. Dalla valutazione di domini fluidi contornati da parti solide rigide e non reattive alle sollecitazioni che si propagano nel fluido, si è poi passati all'assunzione di una matrice solida elastica e quindi reagente attraverso gli sforzi scambiati all'interfaccia solido-fluido, ricavando prima la distribuzione delle pressioni nel solo fluido dovuti all'azione del solido, e infine analizzando i principali fenomeni che contraddistinguono la distribuzione degli stress nel solido.
In prima analisi quindi, sono state approntate simulazioni numeriche su domini fluidi rappresentanti un canalicolo di sezione e sviluppo longitudinale costanti e uno con invece una brusca variazione di sviluppo assiale, l'incontro di un poro in uno di questi canalicoli, assunto come un allargamento della sezione trasversale, e l'incontro, come caso speculare al precedente, di un restringimento. Per il caso dell'allargamento sono inoltre stati considerati due tipi di variazione di sezione: uno più brusco e uno più graduale, con il raggiungimento della sezione allargata dopo una lunghezza maggiore. L'area indisturbata di questi canalicoli è stata mantenuta in tutti i casi con diametro D di 10 μm, utilizzato come dimensione caratteristica per l'adimensionalizzazione spaziale dei risultati.

Su questi domini è stata simulata l'azione di tre treni di onde di pressione monocromatiche a diversa frequenza: 10^6, 10^7, 10^8 Hz. Questo perché l'impedenza acustica è una grandezza funzione della frequenza, ed è quindi corretto analizzarne le variazioni a seconda della frequenza di input considerata.
Sui risultati di pressione e velocità è quindi stata eseguita la trasformata di Fourier per la loro analisi nel campo delle frequenze e infine, dopo aver effettuato il rapporto tra le loro rappresentazioni complesse, sono stati estratti i valori di impedenza per particolari sezioni situate prima, in corrispondenza e successivamente ciascuna analizzata singolarità topologica.
Nella figura sottostante sono riassunte, a titolo di esempio, i risultati di impedenza per la frequenza di 10^7 Hz ottenuti in varie sezioni dei sopra citati domini fluidi.

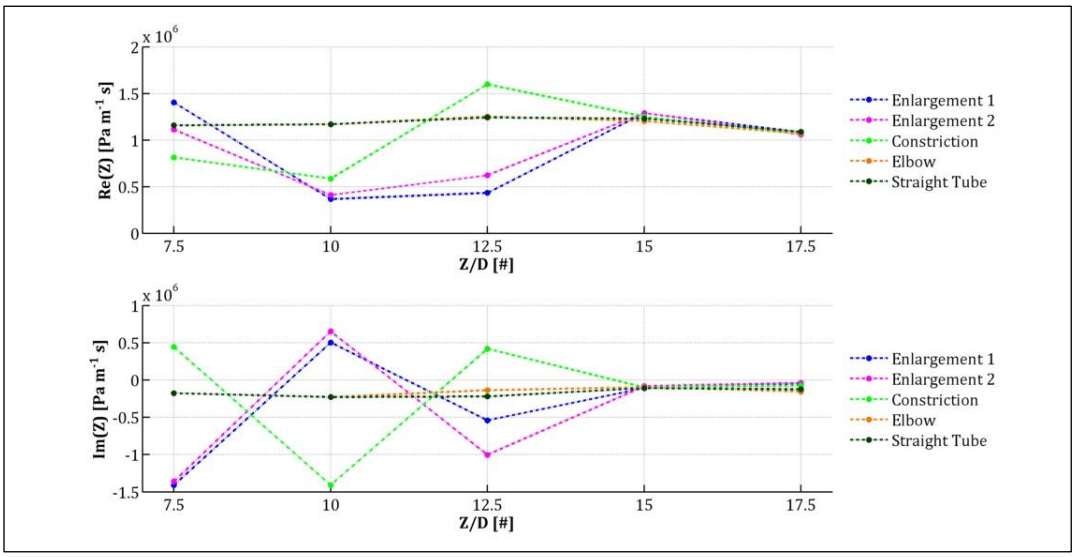

Risultati di parte reale ed immaginaria dell'impedenza per le sezioni osservate ottenuti per geometrie fluide sollecitate con una frequenza di 10^7 Hz.

I comportamenti di parte reale e parte immaginaria sono risultati rappresentativi dei fenomeni in atto all'interno di ciascuna configurazione.
Il valore della parte reale, cioè della parte direttamente proporzionale all'intensità del segnale rilevato e quindi la parte che testimonia il passaggio di energia, risulta, per la geometria del canalicolo rettilineo, stabile attorno al valore ricavabile tramite la semplicistica formulazione dell'impedenza caratteristica data dal prodotto tra densità del materiale e celerità della perturbazione, che in questo caso è circa 10^6 $Pa \cdot m^{-1} \cdot s$, fornendo un indice della correttezza delle simulazioni effettuate.
Non solo, dai risultati emergono comportamenti correttamente speculari tra l'allargamento e il restringimento di sezione. Questo perché l'impedenza si basa sulla forma e l'entità delle onde riflesse e trasmesse da ciascuna sezione considerata. Su queste geometrie è rilevabile come la trasformazione dell'energia, rappresentata tramite variazione della parte immaginaria o reattanza dell'impedenza, avvenga per l'allargamento come una compressione elastica del maggior volume di fluido incontrato, che si traduce in un incremento negativo della reattanza, mentre per il restringimento in un'accelerazione del volume fluido, che si traduce invece in un incremento positivo.

La sensibilità dell'impedenza rispetto alla frequenza di input è stata riscontrata in tutti i domini analizzati, ma rappresentativi sono i risultati per la geometria con variazione di direzione longitudinale, chiamata in questo lavoro "gomito", riassunti dal grafico sottostante.

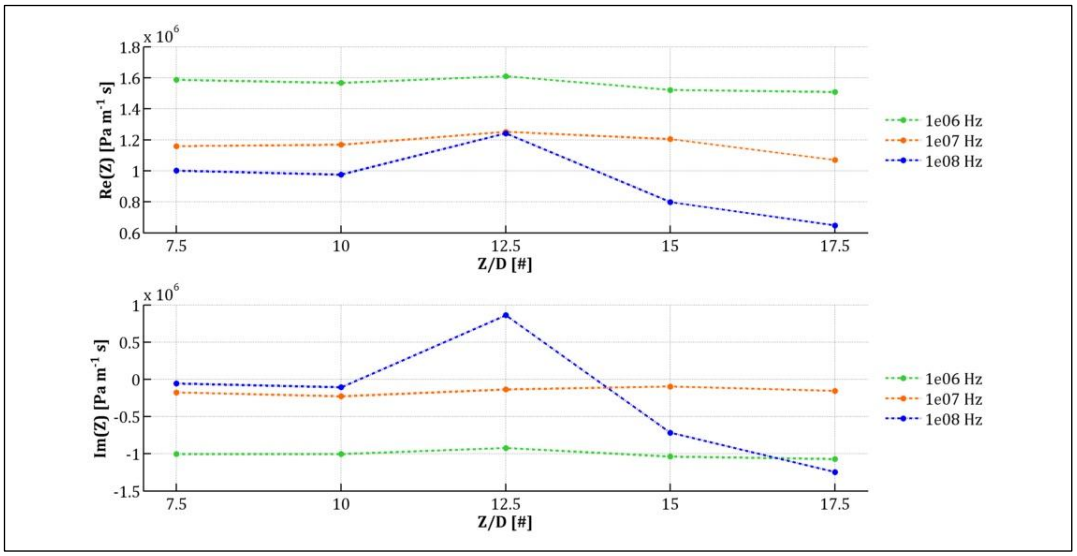

Risultati di parte reale ed immaginaria dell'impedenza per le sezioni osservate ottenuti la geometria fluida rappresentante il cambio di direzione al variare della frequenza di input.

Si è evinto infatti come il gomito si comporti per le frequenze 10^6 e 10^7 Hz come il tubo rettilineo, mentre per 10^8 Hz il segnale inizi a subire l'effetto del cambiamento di direzione. Questo perché, se la lunghezza d'onda del segnale in ingresso risulta comparabile con la dimensione caratteristica del dominio, cioè il diametro, il segnale subisce maggiori riflessioni e quindi si perde la frequenza desiderata in fenomeni di dispersione e dissipazione di energia.
Per tutte le considerate geometrie, inoltre, più la lunghezza d'onda del segnale di input si avvicina alle dimensioni del diametro più l'ampiezza del segnale di pressione diminuisce, indicando una peggiore trasmissione ed una maggiore impedenza di determinate sezioni.
Successivamente è stato considerato il dominio solido circondante il fluido come elastico e quindi reagente alle sollecitazioni esercitate all'interfaccia. Quindi simulazioni FSI sono state effettuate sui domini sopra elencati per poter infine analizzare tramite un confronto l'influenza della FSI sulla valutazione dell'impedenza acustica.
Per comprendere meglio l'azione del fluido sul solido in queste simulazioni solamente la parte fluida è stata caricata con i tre segnali di pressione sopra indicati, trasmettendo la sollecitazione al solido principalmente per effetto Poisson che per il solido considerato, roccia, è determinato da un coefficiente ν uguale a 0,3.
Allargamento, restringimento e tubo dritto sono stati confrontati, ottenendo risultati con andamenti simili a quelli già ottenuti per i soli domini fluidi, come si può notare dalla figura sottostante per la frequenza di 10^7 Hz.

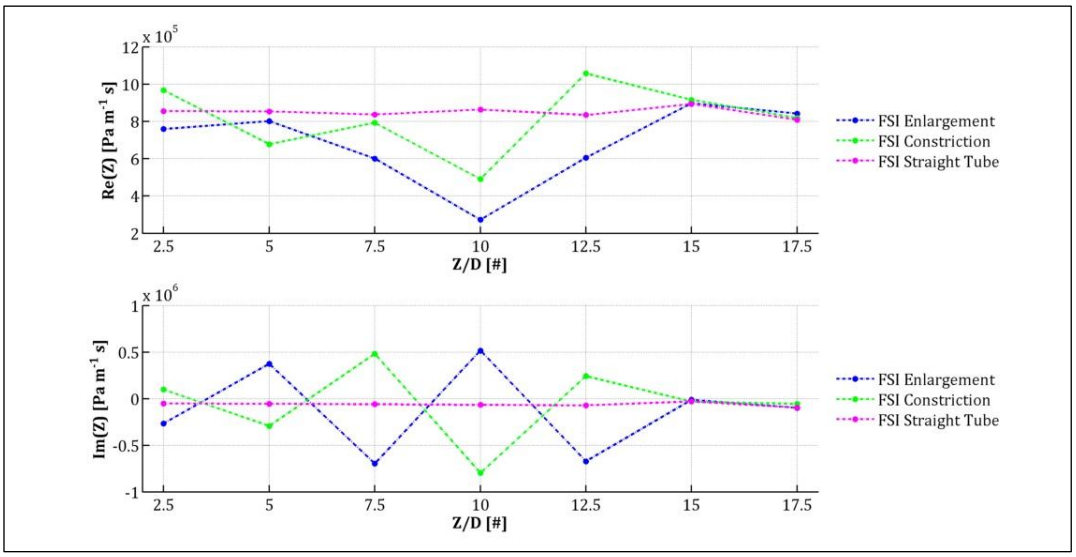

Risultati di parte reale ed immaginaria dell'impedenza per le sezioni osservate ottenuti per geometrie FSI sollecitate con una frequenza di 10^7 Hz.

Come esempio dell'influenza del solido sulla parte fluida si può notare dalla figura seguente l'esistenza della cosiddetta "precursor wave", un'onda creata per effetto Poisson sul solido che, data la maggiore rigidezza di questo, si propaga ad una celerità superiore a quella delle perturbazioni del fluido, sollecitando a sua volta il fluido stesso.

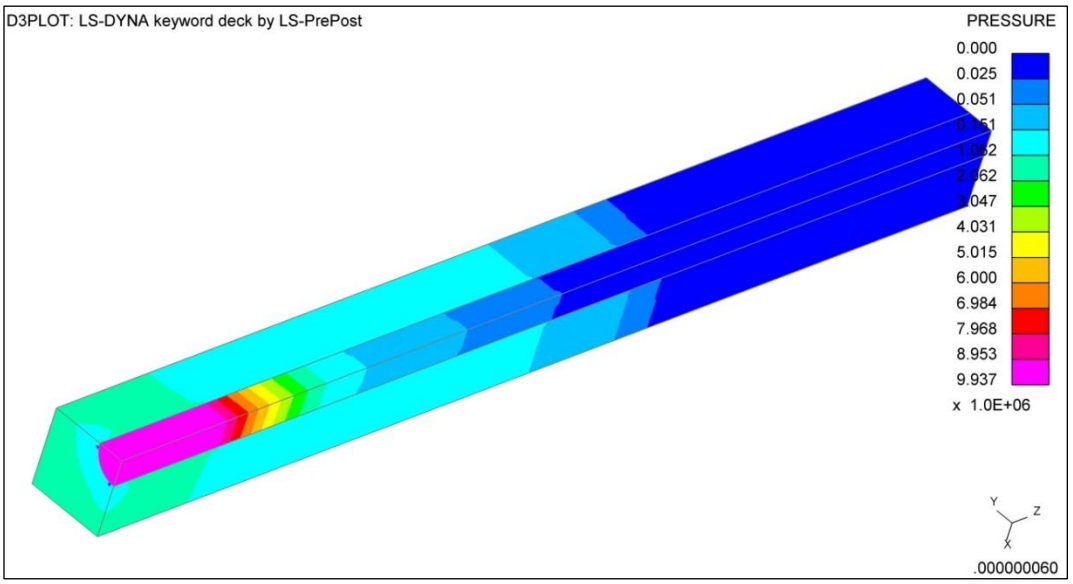

Precursor wave nel solido per la sollecitazione iniziale di 10^7 Hz.

Esempio della differente reazione alla stessa onda in ingresso, e rappresentazione spaziale dell'influenza della geometria sulle grandezze che caratterizzano l'impedenza di una sezione, cioè pressione e velocità, viene fornita della seguente immagine. Ad un fissato istante di tempo si può notare come campi di velocità

speculari vengano creati nelle sezioni antecedenti le singolarità, formando quindi i valori di impedenza sopra presentati.

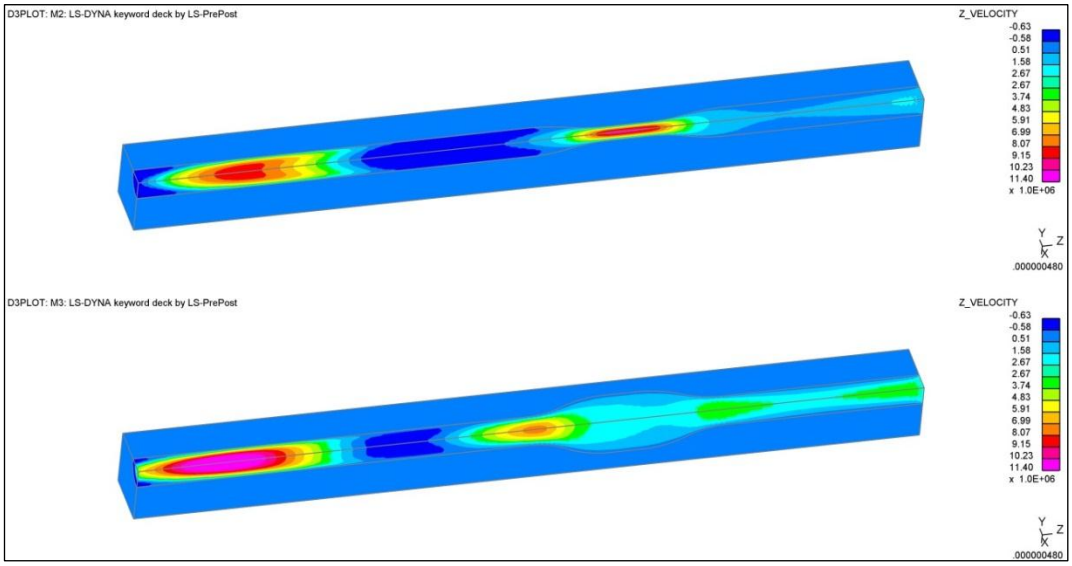

Campi di velocità nei domini FSI per le geometrie rappresentanti l'allargamento e il restringimento sottoposti a una sollecitazione di frequenza 10^7 Hz.

Si sono infine confrontati i risultati ottenuti tramite l'utilizzo di un contorno rigido o di un contorno elastico per ciascuna geometria. Dai grafici, come quello sottostante ricavato per l'allargamento sottoposto al segnale di frequenza 10^7 Hz, è emerso come la reazione del solido elastico porti ad un decremento in generale della parte reale del segnale, indicando peggiore trasmissione. Questa divergenza tra gli andamenti è risultata maggiore in media del 15% in sezioni lontane dalla singolarità analizzata, mentre diventa nettamente minore in corrispondenza di queste ultime.

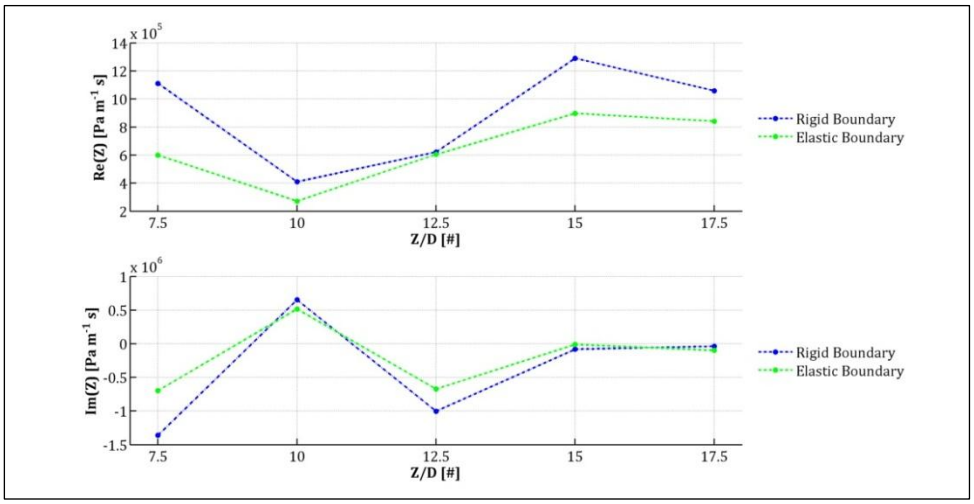

Risultati di parte reale ed immaginaria dell'impedenza per le sezioni osservate ottenuti per l'allargamento simulato con solido rigido ed elastico al contorno, sollecitato con una frequenza di 10^7 Hz.

Questi risultati confermano la bontà del metodo utilizzato per la valutazione dell'impedenza acustica in determinate sezioni, che quindi può essere utilizzato anche in domini più complessi, che comportano però una maggiore difficoltà nella comprensione dei risultati.
In ultima analisi si è osservato il comportamento delle distribuzioni degli stress nella matrice solida in seguito alla sua sollecitazione in fase iniziale assieme alla parte fluida. Alle simmetrie sulle superfici laterali a priori imposte per rappresentare l'infinita continuità spaziale del dominio creato, sono state considerate differenti condizioni di vincolo alla traslazione longitudinale del sistema.
Due principali fenomeni sono stati riscontrati. Il primo è l'aumento dell'ampiezza della precursor wave funzione della maggior mobilità del sistema, data da inferiori nodi del dominio solido vincolati, come si può riscontrare dal grafico sottostante ottenuto vincolando il solido alla traslazione longitudinale solamente negli angoli esterni.

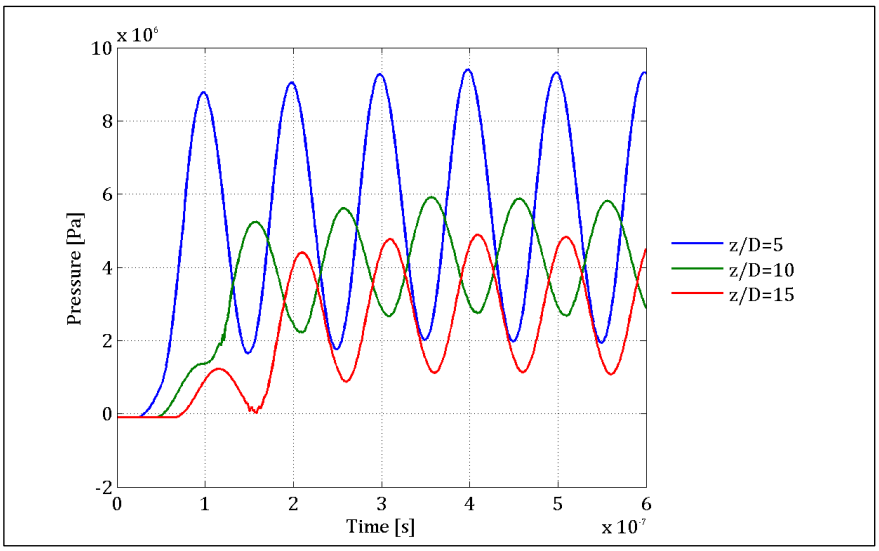

Segnali di pressione per tre sezioni osservate nel caso di nodi agli angoli esterni della sezione solida di input vincolati. Dominio sollecitato con una frequenza di 10^7 Hz.

Mentre il secondo è riscontrabile dalla rappresentazione degli sforzi nel solido al variare del tempo per le fissate sezioni considerate, esemplificata nella figura di seguito per il caso con gli angoli esterni della sezione di input vincolati. L'effetto Poisson genera infatti onde longitudinali nel solido che riflettono sui nodi vincolati e provocano onde che modulano longitudinalmente la distribuzione degli sforzi nel solido. Infine si noti come la viscosità del fluido fa si che le oscillazioni in ampiezza degli stress nel solido si stabilizzino solo dopo un transitorio iniziale.

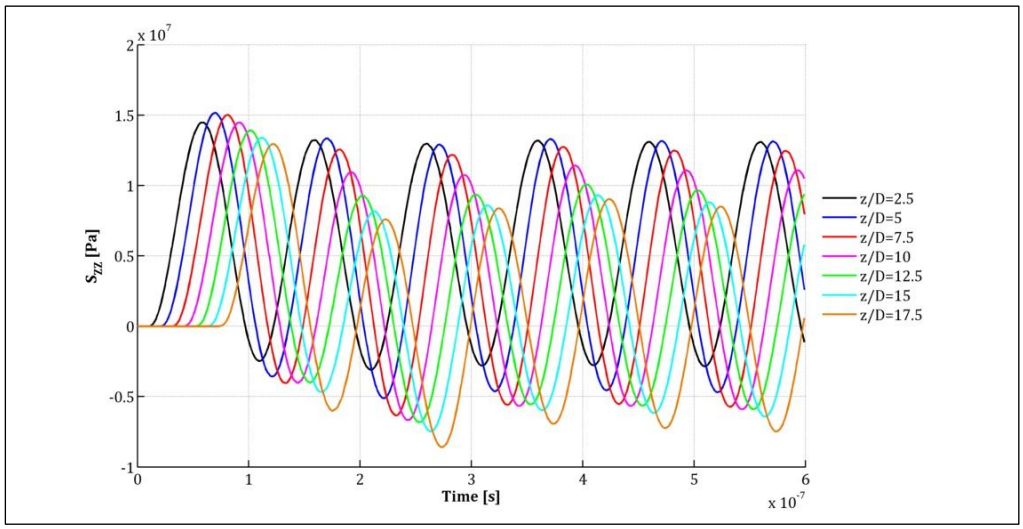

Sviluppo temporale della componente longitudinale dello stress S_{zz} nel solido per le diverse sezioni osservate. Dominio sollecitato con una frequenza di 10^7 Hz.

Gli studi intrapresi dal gruppo di ricerca in cui questo lavoro si è inserito continueranno inserendo sempre più gradi di complessità al problema finora presentato. Pertanto questa tesi può essere considerata come un passaggio all'interno della ben più lunga analisi da effettuare per arrivare al risultato finale, cioè la caratterizzazione dell'impedenza acustica per un dominio complesso come un solido poroso. Tuttavia, come è noto ai più, per raggiungere la cima della scala è prima obbligatorio percorrerla gradino per gradino, e questo lavoro mira a rappresentare uno di questi gradini.

Contents

List of figures

List of tables

1 Introduction

Nowadays underground investigations have become one of the primary interest for the companies producing energy with sources deriving from hydrocarbons. Geologic explorations represent the way to improve production and as a consequence economic power in the most important markets.
The costs of these research operations get balanced only with sure earnings from future production, that's why the aim of tracing soil's structure is to get maps of the geologic configuration as large and precise as possible.
This requires high levels of knowledge of the physics and material properties of the underground sections of interest, which are in most of the cases not directly available because of the great depths of reservoirs. Main coefficients and parameters used to solve the motion equations of solid and fluid media are in that way not achievable.
However, this lack of information can be filled acting on this problem with another prospective: the acoustic logging of the subsoil through the acoustic impedance tracing.
Chapter two provides brief explications on how these investigations are performed in most of the cases.
In Chapter 3, this work aims to understand variations of this acoustic parameter in a different way from the mainstream theories, which are mainly based on semi-empirical models for impedance formulations [1], reflection coefficients calculations [2] or simply observing the behavior of the phase velocity into desired materials after the imposition of a pressure signal [3]. The acoustic impedance is in fact evaluated through the simple pressure and velocity signals to estimate its basic variations in sections of fluid and solid domains.
Since pressure and velocity are measurable quantities in many fluid and solid domains, this approach can be adopted simply extracting those variables, with suitable technologies, also for other similar problems which imply an impossibility to analyze experimentally a part of physic material.
In a large variety of engineering problems in fact there is the need to inspect material non visible properties.
For example, in underground engineering a preliminary geological investigation, similar to the one needed for oil extractions, has to be completed before starting ground movements, and acoustic technologies are frequently employed to detect particular formations or the presence of water.
With regard to structural engineering, non-destructive testing is necessary for faults inspection of structural parts, such as concrete blocks or metal components. Pipelines require also in the monitoring phase acoustic inspections for leakage detection and flow obstructions.
Furthermore, for soundproof materials design [4], the structure is similar to the one present in a porous ground, and an impedance characterization is necessary for those complex domains.
One of the main purposes of this study is, consequently, to identify a numerical solver and with proper modeled domains and boundary conditions able to solve

these kind of engineering problems, including the porous acoustic characterization one.
In order to correctly set up numerical simulations and properly model those types of issues, in chapter 4 is described the method adopted to find the fluid-structure interaction solver which best fitted the results of an exact analytical FSI solution. This one has been obtained from the theories concerning pipelines design, with regard to the stress calculations after a suddenly imposed pressure condition such as the case of water hammer waves.
Once found the best solver, in chapter 5 is provided the acoustic impedance analysis of some representative fluid geometries, ideally surrounded by a rigid solid body. Proofs of reliability of the obtained results have been provided by many theoretical examples, taken from the acoustic engineering for waveguides and confined fluids.
These acoustic impedance values have been adopted as a comparison case for the investigations performed in the following chapter.
Chapter six in fact reports the analysis of the same fluid geometries previously treated, without neglecting the interaction between fluid and solid matrices. The solid portion is, in this case, considered as linear elastic with predefined properties. A final comparison of results obtained in chapter five and six is then provided.
As a further evaluation, in chapter seven the influence of various boundary conditions combinations on the stress distribution in the solid matrix is then performed.
The final conclusions this study led to are reported in chapter eight and, as already said, they are applicable not only for inspections in the field where this research is started, but also in many other similar contexts.

2 Basics and methods for subsurface geological interpretation

2.1 Reservoirs geometry and geology

The efficient extraction of oil and gas requires that the reservoir is visualized in 3D space. Engineers need a conceptual model of reservoirs. Conceptual models are an integral part of the decision-making process, whether that process involves selecting perforations or forecasting future production. However, most engineering measurements made on reservoirs have little or no spatial information. For example, a core measurement has no dimensional information, wireline logs and continuous core measurements are 1D, and production data and pressure information are volumetric but with unconstrained spatial information. Geologic information, on the other hand, contains valuable spatial information that can be used to visualize the reservoir in 3D space. Therefore, engineers should understand the geologic data that can improve their conceptual model of the reservoir and, thus, their engineering decisions [5].

The most important geologic information is the external geometry of the reservoir, defined by flow barriers called "seals" that inhibit the migration of hydrocarbons, forming a hydrocarbon trap. The buoyancy force produced by the difference in density between water and hydrocarbons drives migration. Migration will cease, and a hydrocarbon reservoir will form, only where hydrocarbons encounter a trap.

To visualize the reservoir in petrophysical terms, the engineer must be able to equate measurements (log, core, or production) with geologic models because the measurements themselves do not contain spatial information. Linking engineering measurements with geologic descriptions is best done at the rock-fabric level because rock fabric controls pore-size distribution, which, in turn, controls porosity, permeability and capillary properties. Rock fabrics can be tied directly to stratigraphic models and, thus, to 3D space.

Hydrocarbons are formed by anaerobic decomposition of organic matter that accumulates from the deposition of plankton in deep ocean basins. Oil and gas are generated as the sediments are buried and the temperature rises. Oil is the first hydrocarbon to be generated, followed by wet gas, and lastly by dry gas. Once generated, oil and gas flow vertically and laterally through overlying sediments because of the density difference between hydrocarbons and formation water and they migrate through permeable formations until they encounter a reservoir trap in which oil and gas accumulate. Oil will fill the traps first because it is first to be generated. Higher temperatures resulting from continued burial cause gas to be generated. Migrating gas will displace oil from the traps because gas has a lower density. The displaced oil will migrate further updip and fill any trap encountered.

Traps filled with hydrocarbons are often referred to as pools. However, engineers normally use the term reservoir instead of pool for an oil and gas accumulation. A field is composed of one or more reservoirs in a single area. A trap is defined by the geometry of its seals, which are formations with very low permeability and

very small pores that will impede or stop the flow of hydrocarbons. To trap migrating hydrocarbons, seals must contain flow in 3D: the seals must form a closure. In the simplest terms, a trap is similar to a box with its bottom removed. The box is the seal composed of top and lateral seals. A trap may also contain a bottom seal. Imagine a smaller box inserted into the base of the original box. The smaller box is also a seal and confines the reservoir to a layer within the larger box.

Seals may be in the form of impermeable lithologies or faults (Figure 2.1). The simplest traps are convex structures in which the sealing layer dips in all directions from a central structural high, forming domes or doubly dipping anticlines. More complex structural traps are formed when convex structures are truncated by faults or when faulting occurs around a piercement structure. Many traps are combinations of structural uplift, faulting, and stratigraphy, such as an updip pinchout of a sand body into an impermeable shale. A purely stratigraphic trap may form when deposition creates a topographic high that is encased by impermeable lithology, such as shale or salt.

The volume of oil and gas that can accumulate is defined partly by the height of the trap because any additional hydrocarbons will spill out the bottom. The base of the trap is therefore called the spill point. The trap may not be full because the height of the oil column will be controlled by the capacity of the seal to impede flow and the volume of oil that migrates to the trap. In addition, oil/water contacts need not be horizontal because subsurface fluids are rarely static, and the flow can cause the oil/water contact to tilt in the direction of flow.

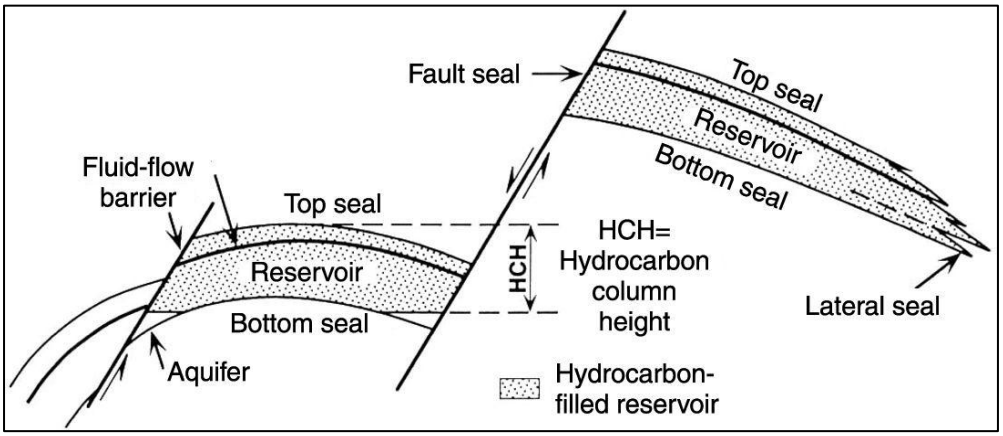

Figure 2.1 - Some typical seals; HCH is the hydrocarbon-column height that the weakest seal will hold (Figure courtesy of Sneider Exploration Inc.).

2.2 Acoustic logging

Petroleum applications of acoustic-wave-propagation theory and physics include both: surface-geophysical methods, borehole-geophysical methods. Acoustic logging is a subset of borehole-geophysical acoustic techniques.
Historically, the primary and the most routine uses of acoustic logs in reservoir engineering have been: porosity determination, identification of gas-bearing intervals, cement evaluation.
Continuing developments in tool hardware and in interpretation techniques have expanded the utility of these logs in formation evaluation and completion (fracture) design and evaluation.
A virtual explosion in the volume of acoustic research conducted over the past 20 years has resulted in significant advances in the fundamental understanding of downhole acoustic measurements. These advances, in turn, have greatly influenced practical logging technology by allowing logging-tool designs to be optimized for specific applications.
Acoustic-wave data-acquisition methods cover a broad range of scales from millimeters to hundreds of meters, as shown in Figure 2.2.

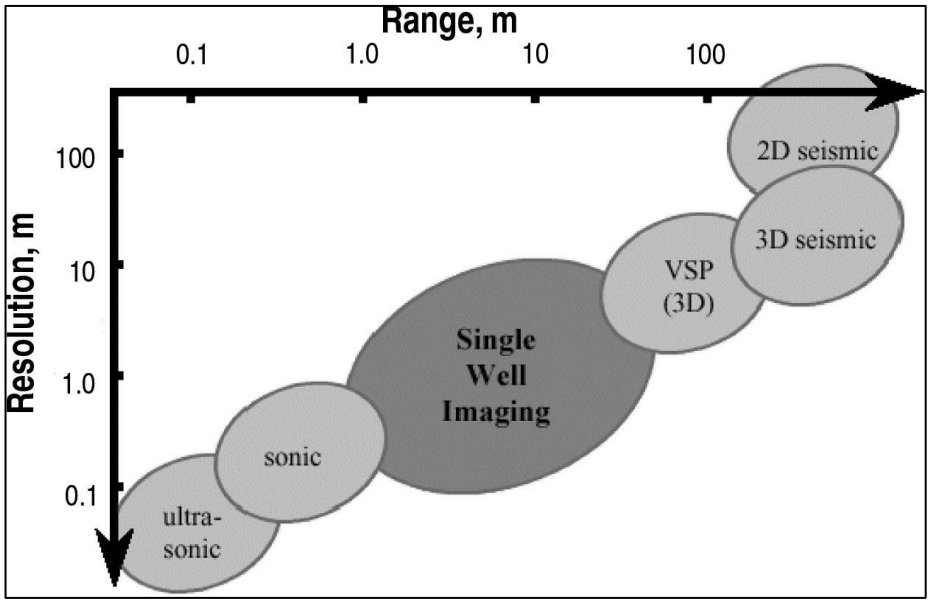

Figure 2.2 - Diagram showing the maximum and minimum ranges vs. the resolution for various acoustic methods (PetroWiki, http://petrowiki.org/PetroWiki).

For the first 4 or 5 decades that seismic-reflection data were acquired, sources and receivers were deployed along the same straight line to create 2D seismic profiles. Two-dimensional seismic data do not yield a correct image of subsurface stratigraphy when a 2D seismic line crosses a complex subsurface structure because the acquisition geometry cannot distinguish reflections that originate from outside the profile plane from reflections that occur within the 2D vertical image plane.
This imaging deficiency of 2D seismic profiling has been remedied by the implementation of 3D seismic data acquisition, which allows data processing to migrate reflections to their correct image coordinates in 3D space. Industry

largely abandoned 2D seismic profiling in the 1990s and now relies almost entirely on 3D seismic data acquisition.
In some reservoir applications, seismic data are acquired with downhole sources and receivers. If the receiver is stationed at various depth levels in a well and the source remains on the surface, the measurement is called vertical seismic profiling (VSP). This technique produces a high-resolution, 2D image that begins at the receiver well and extends a short distance (a few tens of meters or a few hundred meters, depending on the source offset distance) toward the source station. This image, a 2D profile restricted to the vertical plane passing through the source and receiver coordinates, is useful in tying seismic responses to subsurface geologic and engineering control.
If the source is deployed at various depth levels in one well and the receiver is placed at several depth stations in a second well, the measurement is called crosswell seismic profiling (CSP) as shown in Figure 2.3. Images made from CSP data have the best spatial resolution of any seismic measurement used in reservoir characterization because a wide range of frequencies is recorded. CSP data are useful for creating high-resolution images of interwell spaces and for monitoring fluid movements between wells. However, a CSP image is also a 2D profile with the image limited to the vertical plane that passes through the source and receiver coordinates.

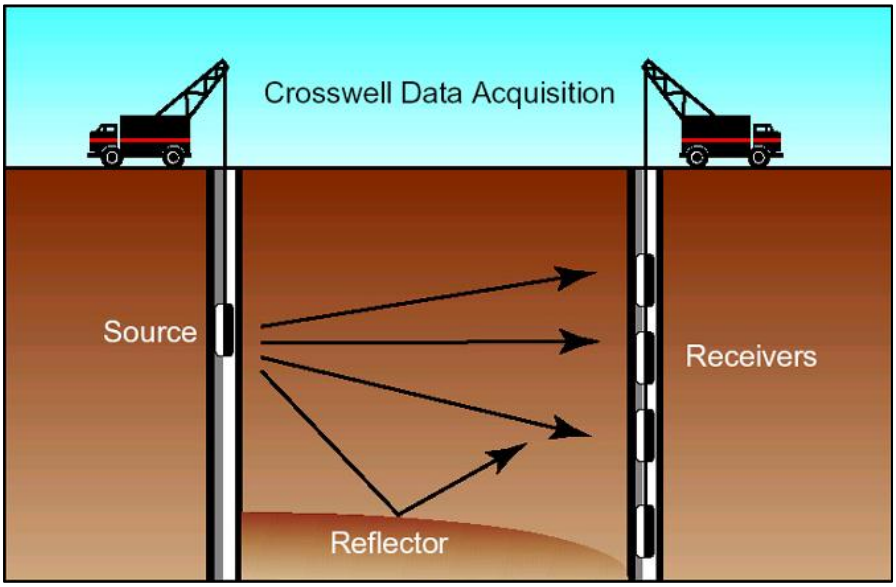

Figure 2.3 – Crosswell imaging (http://en.openei.org/wiki/Single-Well_And_Cross-Well_Seismic_Imaging).

Borehole acoustic-logging measurements are used in a wide variety of geophysical, geological, and engineering applications and play an important role in the undertakings resumed in the following picture (Figure 2.4).

Discipline Application	Geophysics	Geology	Formation Evaluation	Production Engineering	Reservoir Engineering	Well Completion	Drilling	Enhanced Recovery
Synthetic seismogram	X	X	X					
VSP analysis	X	X	X					
AVO calibration	X	X	X		X			X
Porosity evaluation	X	X	X		X	X		X
Lithology estimate	X	X	X		X	X		X
Saturation evaluation		X	X	X	X			X
Gas detection	X	X	X	X	X	X	X	X
Hydrocarbon typing	X	X	X		X		X	X
Fracture analysis	X	X	X		X	X	X	X
Permeability index		X	X		X	X		X
Abnormal pressure		X	X	X	X	X	X	
Wellbore stability		X	X	X		X	X	
Perforation stability			X	X	X	X		X
Anisotropy	X	X	X	X	X	X	X	X
Cement evaluation			X	X	X	X		X

Figure 2.4 - Applications of borehole acoustic data to specific disciplines (PetroWiki, http://petrowiki.org/PetroWiki).

Modern logging tools include conventional borehole-compensated (BHC) monopole devices as well as the newer array devices—both monopole and multipole (monopole/dipole)—and logging-while-drilling (LWD) acoustic services. These logging tools provide acoustic measurements in all borehole mud types (but not in air- or foam-filled boreholes) in vertical, deviated, and horizontal wells, in both open and cased hole. They are combinable with other logging devices and are available in a variety of sizes to accommodate a range of borehole and casing diameters.

In every cited case, acoustic-log data provide a fundamental and essential element of modern seismic reservoir characterization.

Acoustic data acquired using modern array tools can provide high-resolution (0.5 m), microscale "seismic" 2D and 3D images of structural features in the near-borehole region (10 to 15 m). Conventional seismic-processing techniques, including filtering and migration, are used to extract compressional and shear reflections from the acoustic data. The reflections are then used to image geological features near the borehole. This technique allows the imaging of bed boundaries, thin beds (stringers), fractures, faults in open hole and cased wells, and the results is an image similar to Figure 2.5.

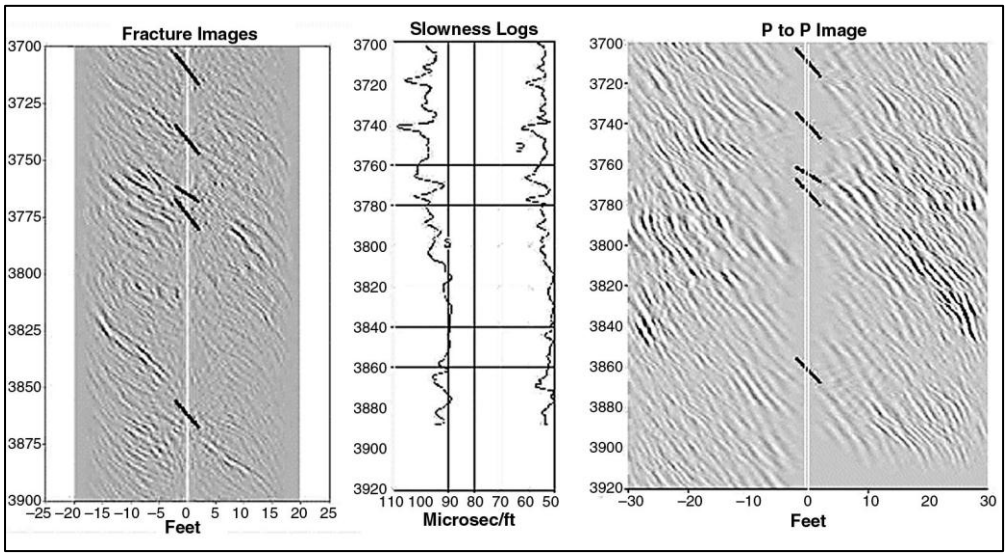

Figure 2.5 - Near-well acoustic image of a fractured reservoir using direct (compressional) (right panel) and converted (shear) (left panel) acoustic modes (PetroWiki, http://petrowiki.org/PetroWiki).

2.3 Borehole imaging

Acoustic borehole-imaging devices are known as "borehole televiewers." They are mandrel tools and provide 100% coverage of the borehole wall. The first borehole televiewer, operating at a relatively high ultrasonic frequency of 1.35 MHz, was developed by Mobil Corp. in the late 1960s. Since then, a succession of improvements have been made, principally through advances in digital instrumentation and computer-image enhancement. Modern tools contain a magnetometer to provide azimuthal information.

The borehole televiewer operates with pulsed acoustic energy so that it can image the borehole wall in the presence of opaque drilling muds. Short bursts of acoustic energy are emitted by a rotating transducer in pulse-echo mode. These travel through the drilling mud and undergo partial reflection at the borehole wall. Reflected pulses are received by the transducer. The amplitudes of the reflected pulses form the basis of the acoustic image of the borehole wall. These amplitudes are governed by several factors. The first is the shape of the borehole wall itself: irregularities cause the reflected energy to scatter so that a weaker reflected signal is received by the transducer. Examples of these irregularities are fractures, vugs, and breakouts. Moreover, the reflected signal is degraded in elliptical and oval wellbores because of non-normal incidence. The second factor is the contrast in acoustic impedance between the drilling mud and the material that makes up the borehole wall. Acoustic impedance provides an acoustic measure of the relative firmness of the formations penetrated by the wellbore material and, thus, it has the capability of discriminating between different lithologies, with high acoustic impedance giving rise to high reflected amplitudes. Borehole televiewers work best where the borehole walls are smooth and the contrast in acoustic impedance is high. The third factor is the scattering or absorption of acoustic energy by particles in the drilling mud. This problem is more serious in heavily weighted muds, which are the most opaque acoustically, and it gives rise to a loss of image resolution.

The borehole televiewer can provide a 360° image in open or cased holes. It can operate in all downhole environments other than gas-filled holes. The travel time for the acoustic pulse depends on the distance between the transducer and the borehole wall, as well as the mud velocity. Modern televiewers allow some independent method of measuring the mud velocity. Thus, the borehole televiewer also operates as an acoustic caliper log. For best results, the tool should be centered, although correction algorithms have been developed for eccentered surveys.

An example of a modern ultrasonic imaging tool is Schlumberger's Ultrasonic Borehole Imager (UBI™), which is based on the cased-hole USI with two hardware modifications: a focused transducer was fitted for improved resolution, and an openhole centralizer was added. The tool incorporates a rotating transducer within a subassembly. The size of the subassembly is selected on the basis of the diameter of the hole that is to be logged. The direction of rotation of the subassembly governs the orientation of the transducer. There are two positional modes: the standard measurement mode with the transducer facing the borehole wall (Figure 2.6), the fluid-property mode with the transducer facing a target within the tool.

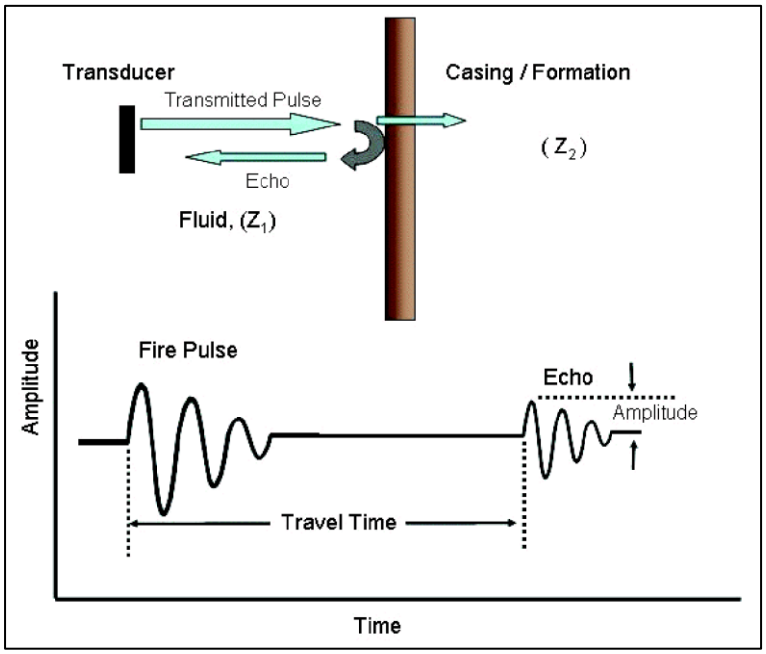

Figure 2.6 - A simplified representation of the path of the televiewer pulse-echo signal (upper) and the measurements made (lower) (PetroWiki, http://petrowiki.org/PetroWiki).

Data are usually presented as depth plots of enhanced images of amplitude and borehole radius. Applications include: fracture detection, analysis of borehole stability, identification of breakouts.
Figure 2.7 shows an example of breakout identification using an ultrasonic borehole televiewer. The data presented are from the Cajon Pass scientific borehole in southeastern California. The aim was to investigate the orientation and magnitudes of in-situ stresses using borehole-image data. The televiewer has superseded multiarm dipmeter calipers for these applications. Although the caliper can reveal the orientation of breakouts, the tool provides little information about their size and, more generally, about the overall shape of the borehole wall. The ultrasonic televiewer can detect much smaller features than the multiarm caliper and can distinguish between features that are stress induced and those that are drilling artifacts.

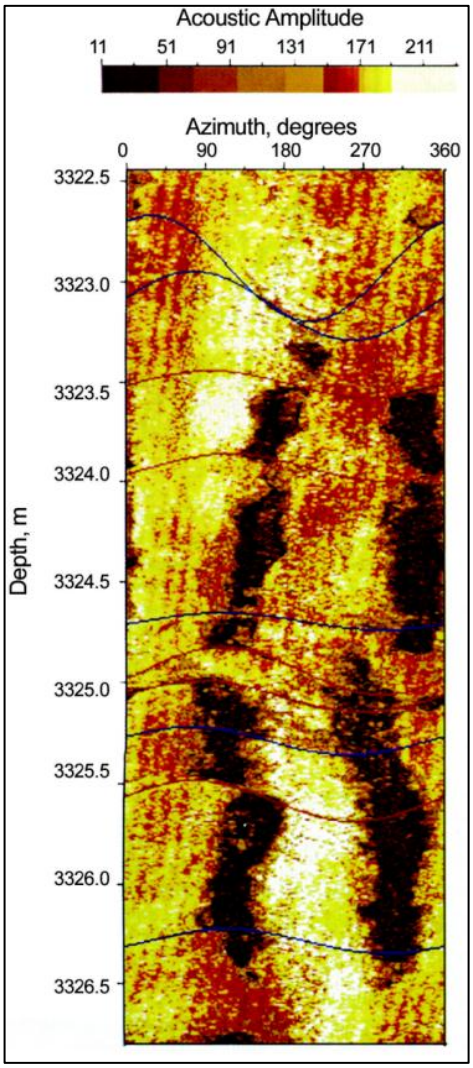

Figure 2.7 - Example of breakout detection using an ultrasonic borehole televiewer. Breakouts are indicated by the low acoustic amplitude of the reflected signal, shown here as darker areas. The breakouts are rotated because of a drilling-induced slippage of localized faults (Courtesy of SPWLA.).

3 Acoustic Impedance : definitions and methods of evaluation

3.1 Acoustics and impedance definition

Although the acoustic behavior of most commonly encountered materials in the audio-frequency range may be analyzed without explicit reference to their molecular nature, it may be helpful to analyze briefly the different molecular structures of solids, liquids and gases. The molecules that form material substances attract each other except where they are in very close proximity, when they exert strong forces of mutual repulsion. Therefore, when molecules approach each other under the influence of the mutually attractive force, they lose potential energy. At the point where the interaction force changes from attractive to repulsive, the sum of the potential energies associated with the two forces is a minimum, known as the 'pair dissociation energy'. This state of equilibrium may be disturbed by the impact of other molecules. If the average kinetic energy of the intruder is much less than the dissociation energy it will be captured, and eventually a large conglomerate of bound atoms will form: this is the case in the solid phase of matter. On the other hand, if the average kinetic energy greatly exceeds the dissociation energy, molecules will never 'bond' for any significant time: this is the gaseous phase of matter. Liquids fall in between these two states where 'bonds' are temporarily made and then broken by encounter with molecules of higher than average energy [2].
The spacing of molecules in solids is such that the shape of the structure is maintained by strong attractive forces. The molecules simply undergo very small vibrational motions unless they acquire so much energy due to heating that they break free of the attractive forces to form a liquid (or, where supplied with sufficiently high thermal energy, to sublime directly into a vapor). In liquids, the molecules move relative to each other in complex paths under the combined influence of forces of attraction and repulsion, allowing the fluid readily to undergo large changes of geometric form under the action of applied forces, so that they adapt their shape to conform to that of a rigid container. In gases, the average spacing of the molecules is so large that attractive forces are very weak; any individual molecule may translate over a substantial distance before coming sufficiently close to another for the force of repulsion to produce a rapid exchange of momentum, in analogy with the collision of billiards balls.
The term 'fluid' implies flow. Flow is usually spatially non-uniform in that it entails relative motion of different elements of the medium and frequently involves intermixing of fluid elements. A principal distinction between fluids and solids is that the former cannot resist steady applied shear forces, which act so as to 'slide' adjacent layers of material over each other. Liquids and gases are therefore both fluids. Solids react to steady shear forces by undergoing shear distortion, which generates proportional opposing forces, so that a state of static equilibrium is attained. Fluids produce no equivalent reaction to steady shear. However, in common with solids, fluids resist changes of volume occupied by any fixed mass of molecules (volumetric strain); this property is essential to the phenomenon of sound in fluids. Fluids also exhibit fluid friction, or viscosity, whereby they resist relative

'sliding' motion associated with differential velocities of adjacent elements; this acts most noticeably in boundary layers close to bodies moving through fluids. The principal mechanism of viscosity in liquids is intermolecular attraction. The principal mechanism is an exchange of mean (time-average) molecular momentum via random molecular transport between adjacent fluid layers moving at different mean velocities. Molecules moving from a fluid element possessing a certain mean velocity into one having lower mean velocity bring with them greater mean momentum than those in the slower element. Satisfaction of conservation of momentum in the absence of external forces requires that the mean momentum of the slower element increases, and vice versa. The effect is to reduce the relative velocities between the elements; the associated rates of change of momentum may be attributed to an internal viscous stress. Fluid viscosity has profound effects within the fibrous and porous materials and that's why they're frequently used as sound absorbers.
Furthermore, if we consider also geometry variations of the considered domains as curves or section variations, we would see how those changes are also obstacles for sound propagation, and correctly evaluating their impact would be a non trivial purpose. One of the typical problems in acoustics is to analyze and predict the acoustical and vibrational behavior of systems consisting of assemblages of structural components surrounded by, and/or containing, one or more types of fluid.
The former support vibrational waves of various types and the latter support acoustic waves. The dynamic behavior of a system is determined partly by the properties of the individual components and partly by the dynamic interactions between them. These interactions involve the incidence of vibrational or acoustic waves upon the junctions, connections and interfaces between components, together with their reflection and transmission. Wave energy may also be dissipated into heat at interfaces such as metal-to-metal joints, bolted, riveted or screwed connections, and by gaskets between engine components and seals of all sorts. It is of the essence of wave-bearing systems that the dynamic response of any one element or component to external excitation is influenced by the dynamic properties of all directly, or indirectly, connected components; this influence will tend to decrease with increase of separation distance through the agencies of dissipation and diffusion. The degree to which waves incident upon junctions are scattered, transmitted and dissipated depends upon the dynamic behaviors of both connected components. This is where the concept of 'impedance', and its companion 'mobility', come into play. They characterize the dynamic behavior of components in such a manner that the system that they form can be represented as a network. Mathematical expression of the impedances, together with the conditions governing forces and motions at connections, produce a set of equations that can be solved once the external excitation mechanisms are specified.
In acoustics, impedance relates the complex amplitude of fluid pressure, or the corresponding force, to the complex amplitude of fluid particle velocity or volume velocity: the ratio of particle velocity to sound pressure is termed 'admittance', instead of mobility. Transfer impedances and mobilities may also be defined: these relate forces at one point to velocities at another. These quantities may only be employed to describe the dynamic behavior of linear systems. In most practical cases, excitations and responses are not harmonic, and not necessarily even time-stationary; but application of the Fourier integral transform, which expresses arbitrary time dependence in terms of a superposition of time-harmonic components, allows us to exploit the concept of impedance in all linear cases.

3.2 Impedance formulation from acoustic energy in fluids

The acoustic energy definition is not so trivial when considering the acoustic field in its linearized equations [6]. Considering the acoustics of a steady fluid, the Kirchhoff approach is based on the following linearized equations (3.1).

$$\frac{1}{c_0^2}\frac{\partial^2 p'}{\partial^2 t} - \nabla^2 p' = q$$
$$q = \frac{(\partial p/\partial s)_\rho}{\rho_0 c_0^2 T_0}\frac{\partial Q_w}{\partial t} - \nabla \cdot \boldsymbol{f} \tag{3.1}$$

where p' is the pressure perturbation, s is the entropy, and Q_w is the source term. The source term represents with its first part a dilatation caused by a heat transfer, while with the second part the production of sound dued by an external non-stationary force field (f is related to the variation in time of the velocity perturbation $\boldsymbol{v}'$. If the source term is zero, the sound is related only to initial and boundary conditions.
After a few passages this can lead to the acoustic energy equation (3.2):

$$\frac{\partial E}{\partial t} + \nabla \cdot \boldsymbol{I} = -\mathcal{D} \tag{3.2}$$

where the acoustic energy E and the intensity I are defined by the following relations (3.3).

$$E = \frac{1}{2}\rho_0 v'^2 + \frac{1}{2}\frac{p'^2}{\rho_0 c_0^2}$$
$$\boldsymbol{I} = p' \tag{3.3}$$

The dissipation $\mathcal{D}$ is the power for unit volume given by the acoustic field to the sources (3.4)

$$\mathcal{D} = -\frac{1}{\rho_0 c_0^2}\left(\frac{\partial p}{\partial s}\right)_\rho p'\frac{\partial s'}{\partial t} - \boldsymbol{f}\cdot\boldsymbol{v}' \tag{3.4}$$

Considering harmonic fields varying with time as $p' = \hat{p}e^{i\omega t}$ and $\boldsymbol{v}' = \boldsymbol{v}e^{i\omega t}$, the time average energy $\langle E\rangle$ is obviously time independent, reducing equation (3.4) to the following relation (3.5)

$$\nabla \cdot \boldsymbol{I} = \langle \mathcal{D} \rangle \tag{3.5}$$

From the integration of this equation on a volume including the sources, the expression of the source power can be found (3.6):

$$\langle P \rangle = -\int_V \langle \mathcal{D} \rangle dV = \int_S \langle \boldsymbol{I} \rangle \cdot n dS \qquad (3.6)$$

where **n** is the outward normal of the control surface *S*.
Finally it can be chosen as boundary condition for this surface, the acoustic impedance of this surface, which can be represented as (3.7):

$$Z(\omega) = \frac{\hat{p}}{\hat{\boldsymbol{v}} \cdot \boldsymbol{n}} \qquad (3.7)$$

having this expression for the acoustic intensity.

$$\langle \boldsymbol{I} \rangle \cdot n = \frac{1}{2} Re(Z) |\hat{\boldsymbol{v}} \cdot \boldsymbol{n}|^2 \qquad (3.8)$$

This last equation has an important meaning. In fact it can be easily seen that the real part of the acoustic impedance is associated with the energy transport through the surface *S*.

3.3 Complex acoustic impedance

As seen before, acoustic impedance is the measure of the opposition that a system presents to an acoustic flow when an acoustic pressure is applied to it.
In quantitative terms, it is the ratio of the complex acoustic pressure applied to a system to the resulting complex acoustic volume flow rate through a surface perpendicular to the direction of this acoustic pressure at its point of application. There is a close analogy with electrical impedance, the ratio of the complex electrical voltage applied to a system to the resulting complex electrical current intensity [7].

3.3.1 Complex definition

Acoustic impedance is the complex representation (also called analytic representation) of acoustic resistance. It is the ratio of the complex acoustic pressure applied to a system to the resulting complex acoustic volume flow rate through a surface perpendicular to the direction of this acoustic pressure at its point of application.
Acoustic impedance, denoted Z and measured in $Pa \cdot m^{-3} \cdot s$ or in $rayl_{MKS} \cdot m^{-2}$, is given by the (3.9):

$$Z = \frac{\hat{p}}{\hat{Q}} = R + iX \qquad (3.9)$$

where:

$\hat{p}$ = complex acoustic pressure [Pa];
$\hat{Q}$ = complex acoustic volume flow rate [$m^3 \cdot s^{-1}$];
R = acoustic resistance [$Pa \cdot m^3 s^{-1}$];
X = acoustic reactance [$Pa \cdot m^3 s^{-1}$];

Sometimes is useful to set a value for the impedance which is independent from the surface on which it is calculated, that's why the specific acoustic impedance is defined.
Specific acoustic impedance is the complex representation of specific acoustic resistance. It is the ratio of the complex acoustic pressure applied to a system to the resulting complex particle velocity, and not particle flux as before, in the direction of this acoustic pressure at its point of application.
Specific acoustic impedance, denoted z and measured in $Pa \cdot m^{-1} \cdot s$ or in $rayl_{MKS}$ is given by (3.10):

$$z = \frac{\hat{p}}{\hat{v}} = r + ix \qquad (3.10)$$

The relation between these two impedance is now explained.
Consider a one dimensional wave passing through an aperture with area A. The acoustic volume flow rate Q is the volume of medium passing per second through the aperture. If the acoustic flow moves a distance dx = vdt, then the volume of medium passing through is dV = Adx. The acoustic impedance Z is the ratio of complex acoustic pressure to complex acoustic volume flow rate, so provided that the wave is only one-dimensional, it yields:

$$Q = \frac{dV}{dt} = A\frac{dx}{dt} = Av$$
$$Z = \frac{\hat{p}}{\hat{Q}} = \frac{\hat{p}}{A\hat{v}} = \frac{z}{A} \tag{3.11}$$

With the aim of estimate the acoustic impedance for a plane wave travelling in an infinite medium [8], the solution of the sound wave equation can be used (3.12).

$$u = \frac{\partial y}{\partial t} = -y_m \omega \cos(kx - \omega t)$$
$$p = -\kappa \frac{\partial y}{\partial x} = -\kappa y_m k \cos(kx - \omega t) \tag{3.12}$$

where:
κ =adiabatic bulk modulus [Pa];
A = signal amplitude [Pa];
y = displacement coordinate [m];
x = domain coordinate [m];

Having defined the specific impedance as the ratio of the pressure and the velocity, it can be derived the value of the so called "characteristic" specific acoustic impedance (3.13):

$$z = \frac{\kappa k}{\omega}$$
$$z = \rho c \tag{3.13}$$

considering $\kappa = \rho c^2$ and $c = \omega/k$.
However, the characteristic specific acoustic impedance represents only the real resistive part of the whole impedance, and it is not enough to completely characterize the problem. That's why it is necessary to introduce and describe the values and the physics behind the imaginary part, which doesn't transport energy but plays an important role in these phenomena.

3.3.2 Acoustic inertance

As mentioned above Z usually depends strongly on frequency. When a small volume is compressed by a sound wave, the volume flow acts to compress the air and raise its pressure. So it acts as a compliance, strictly related to the stiffness of the material. When a small volume is accelerated by the difference in sound pressure, acoustic flow is determined by pressure difference and we have an acoustic inertance [9].
Acoustic inertance and acoustic compliance introduce two very important special cases. Both use the idea of a compact region: a region whose dimensions are much smaller than the wavelengths we are considering. As a consequence, the variation in the phase of the sound wave is small in the region, and so the pressure is approximately uniform.
A small cylinder with area A and length L is vibrating due to an acoustic pressure difference p applied across it.

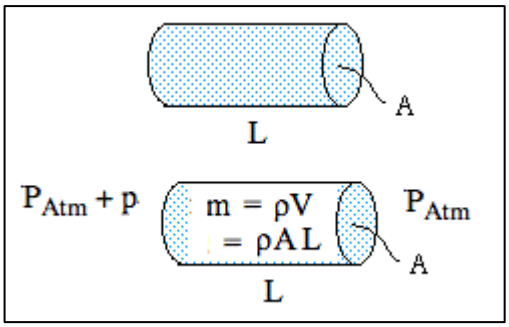

Figure 3.1 – Elementary domain for inertance example (School of Physics, Sydney Australia, http://www.animations.physics.unsw.edu.au).

Let it vibrate in the x direction with position $y = y_m cos\ \omega t$, so its acceleration and its velocity are is (3.14):

$$a = \frac{\partial^2 y}{\partial t^2} = -\omega^2 y_m \cos \omega t$$
$$U = Au = -A\omega y_m \sin \omega t \qquad (3.14)$$

From the definition of density ρ = mass/volume, the mass of the cylinder is ρV = ρAL. The net force acting on it is pA. So substitution in Newton's second law (F = ma) gives (3.15):

$$pA = \rho AL(-\omega^2 y_m \cos \omega t) =$$
$$= -(p_m \cos \omega t)A \qquad (3.15)$$

which tells us that p and U are 90° out of phase, and also their ratio, that is to say the impedance. When the inertia of the material plays an important role in this phenomenon we would see the pressure preceding the flow, because of the positive phase of 90°.
Impedance due to inertia in this case will assume the following form, resolving the ratio of p and U (3.16).

$$Z = \frac{j\omega\rho L}{A} \qquad (3.16)$$

This relation states that vibration at higher frequency requires greater acceleration and therefore greater acoustic pressure.

3.3.3 Acoustic compliance

Now let's consider a small volume *V*, this time, the applied pressure will compress it, so let's imagine a cylinder of air in a duct with cross section *A*, that is closed at the right hand end. We apply an acoustic pressure p at the left hand end.

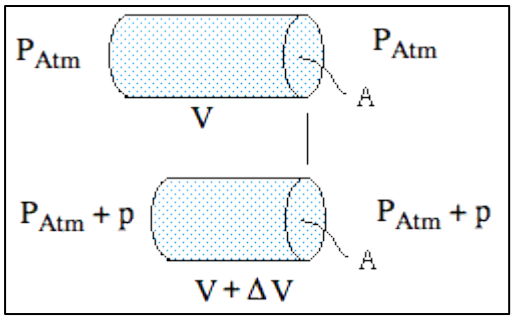

Figure 3.2 – Elementary domain for compliance example (School of Physics, Sydney Australia, http://www.animations.physics.unsw.edu.au).

This compresses it with an oscillating displacement, at the left end only, $y = y_m \cos \omega t$. At the instant of my sketch, p is positive and ΔV negative. The volume is changed over time by (3.17):

$$\Delta V = y_m \cos \omega t = (\Delta V)_m \cos \omega t$$
$$Q = -\frac{\partial}{\partial t}(\Delta V)_m \cos \omega t \qquad (3.17)$$

The pressure change p required to produce fractional volume change ΔV/V in a gas initially at pressure P is (3.18):

$$p = \gamma P \Delta V / V \qquad (3.18)$$

where γ is the adiabatic factor.
Now the pressure at equilibrium is atmospheric pressure P_A. So the fractional change in pressure is (3.19):

$$\frac{p_m}{P_A} = -\gamma (\Delta V)_m \cos \omega t / V \qquad (3.19)$$

where we observe that the pressure (a minus cosine function) is 90° behind the flow (a sine function). In complex notation, we would write this as (3.20):

$$Z = -\frac{j\gamma P_A}{\omega V} = \frac{1}{j\omega C} \qquad (3.20)$$

where C is the acoustic compliance.
Here, it is gas flowing in that increases the pressure. That's why Z is inversely proportional to omega: vibration at higher frequency has a shorter period, so the amount of gas that flows in during the half period for which flow is inwards is smaller, and produces a smaller pressure. The air in the confined volume acts like a spring. In analogy with mechanical compliance, a compact enclosed volume is called a compliance and an acoustical impedance in which the pressure lags the flow by 90° is called a compliant impedance.

3.4 Forms of impedance for mechanical solid systems

The term 'mechanical impedance' relates principally to solid structures, although, as we have already seen, the reaction forces imposed by fluids on vibrating structures may also be expressed in terms of an equivalent mechanical impedance [2]. Vibrational excitation generates a number of different forms of wave in solid structures; those most important in vibroacoustics are illustrated in Figure 3.3.

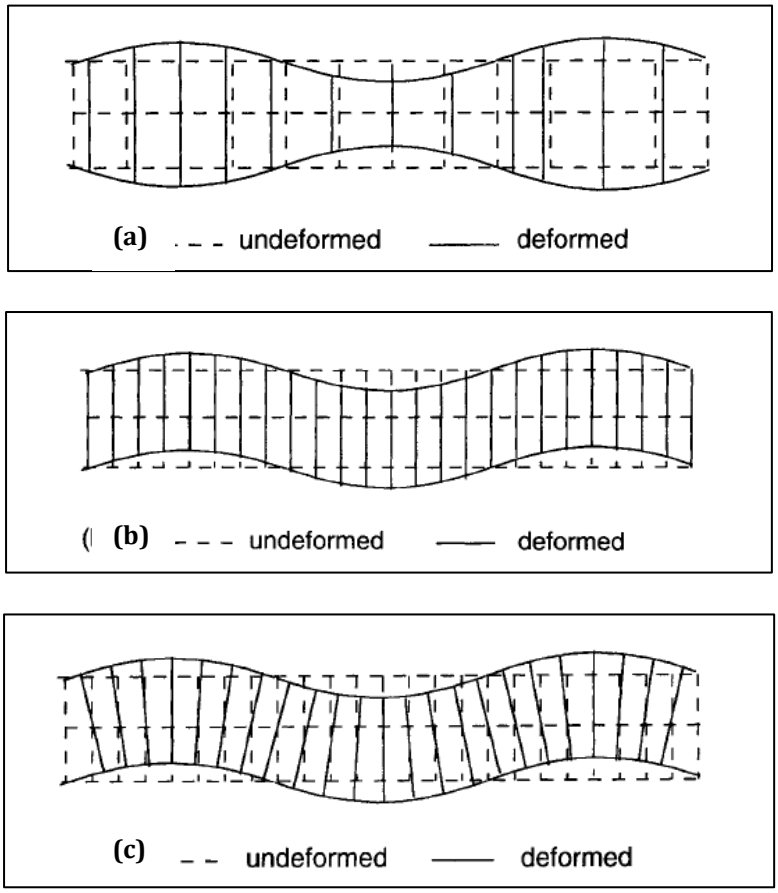

Figure 3.3 - a) beam under longitudinal wavelet; b) beam under shear wavelet; c) beam under bending (flexural) wavelet (Frank J. Fahy, Foundations of Engineering Acoustics*, 2001).*

As shown previously in this chapter, the same concept referred to a region of fluid which has dimensions very much less than an acoustic wavelength may be applied to structural lumped mass systems.
In fact the most elementary vibrational model consists of a lumped mass connected to a rigid 'earth' by means of a lumped, linear, massless spring element. More complex systems may be modeled as networks of masses and springs, which is how J. L. Lagrange first modeled wave motion in a stretched string. The mechanical impedance of a lumped mass is defined as the ratio of complex amplitude of the net harmonic force on the body to that of the associated velocity (Figure 3.4).

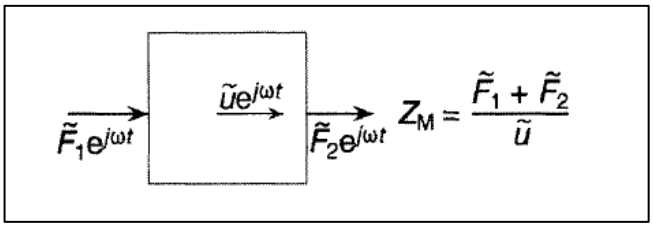

Figure 3.4 - Lumped mass system (Frank J. Fahy, Foundations of Engineering Acoustics*, 2001).*

The relation between the net force on the mass and its acceleration is the following (3.21).

$$F = M\frac{d^2x}{dt^2} = M\frac{du}{dt} \qquad (3.21)$$

The mechanical impedance of the mass under harmonic excitation $\tilde{F}exp(j\omega t)$ is (3.22):

$$Z_m = \tilde{F}/\tilde{u} = j\omega M = Z_M \qquad (3.22)$$

where the inertial impedance is characteristically imaginary, proportional to ω and, if the harmonic motion is represented by $exp(j\omega t)$, positive.
The stiffness of a massless elastic spring is defined as the inverse of the net change of length per unit applied force: the internal force must necessarily be uniform throughout the spring (Figure 3.5).

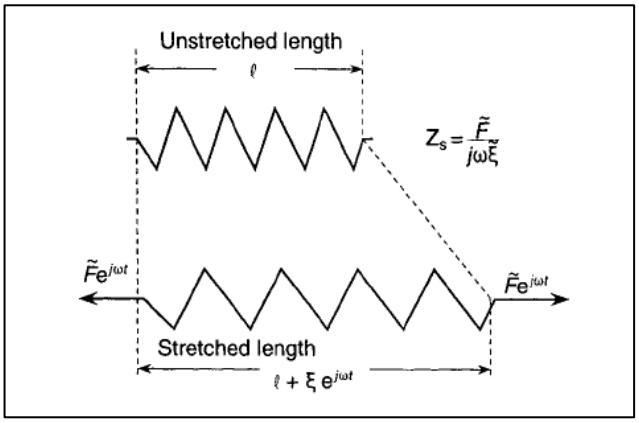

Figure 3.5 - Lumped striffness system (Frank J. Fahy, Foundations of Engineering Acoustics*, 2001).*

The impedance is defined as the ratio of the complex amplitude of the force applied at one end to that of the associated differential velocity of the two ends (3.23).
Hence it is

$$Z_m = \tilde{F}/j\omega\Delta\tilde{x} = -jK\omega = Z_s \qquad (3.23)$$

where K is the spring stiffness. Elastic impedance is characteristically imaginary, inversely proportional to ω, and negative. These models have acoustic analogues in fluids as shown before.

We now consider how mathematical expressions can be derived for combinations of inertial and elastic elements.
For this work it's useful consider how mathematical expressions can be derived for combinations of inertial and elastic elements. Figure 3.6 shows a rigid inertial lumped element 'attached' to an arbitrary system having an impedance Z_t .

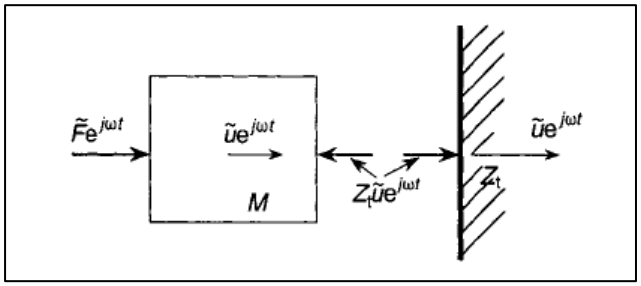

Figure 3.6 - Impedance 'seen through' a rigid mass (Frank J. Fahy, Foundations of Engineering Acoustics*, 2001).*

Equilibrium gives (3.24):

$$\tilde{F} - Z_t\tilde{u} = j\omega M\tilde{u} \qquad (3.24)$$

and the impedance of the combined system 'seen through' the mass is (3.25):

$$Z_m = \tilde{F}/\tilde{u} = Z_t + Z_M \qquad (3.25)$$

In electrical terminology, the two components are connected in series because they share the same velocity, so that the impedances simply sum.

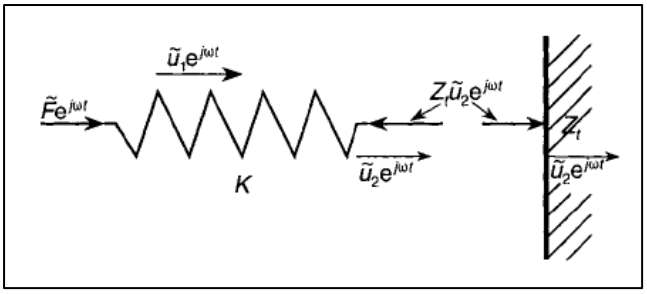

Figure 3.7 - Impedance 'seen through' a spring (Frank J. Fahy, Foundations of Engineering Acoustics*, 2001).*

Figure 3.7 shows an elastic spring terminated by a system of impedance Z_t. The spring force is given by (3.26):

$$\tilde{F} = Z_t\widetilde{u_2} = Z_t(\widetilde{u_1} - \widetilde{u_2}) \qquad (3.26)$$

Elimination of $\widetilde{u_2}$ gives the impedance of the combined system 'seen through' the spring as (3.27):

$$Z_m = \tilde{F}/\widetilde{u_1} = Z_tZ_s/(Z_t + Z_s) \qquad (3.27)$$

In electrical terms, the components are in parallel because they share the same force.

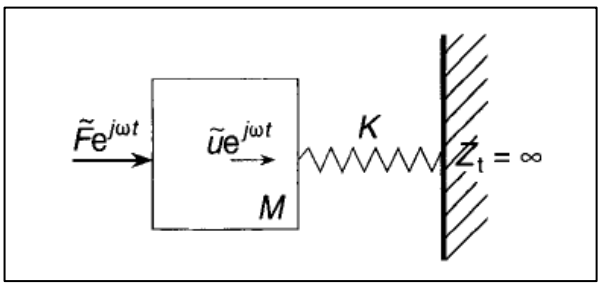

Figure 3.8 - Earthed mass-spring system (Frank J. Fahy, Foundations of Engineering Acoustics*, 2001).*

The impedance of the earthed mass-spring system shown in Figure 3.8 is the sum of the impedance of the mass and of the spring with Z_t put to infinity in (3.28):

$$Z_m = \tilde{F}/\tilde{u} = j(\omega M - K/\omega) \qquad (3.28)$$

The natural frequency of free vibration ω_0 is given by the condition that the Z_m is zero - no driving force necessary. Hence it's trivial to achieve (3.29).

$$\omega_0 = (K/M)^{1/2} \qquad (3.29)$$

At frequencies well below ω_0 , Z_s dominates; at frequencies well above ω_0 , Z_M dominates.
A further generic lumped element may be added to the mass-spring system in the form of a linear, massless, viscous damper (Figure 3.9).

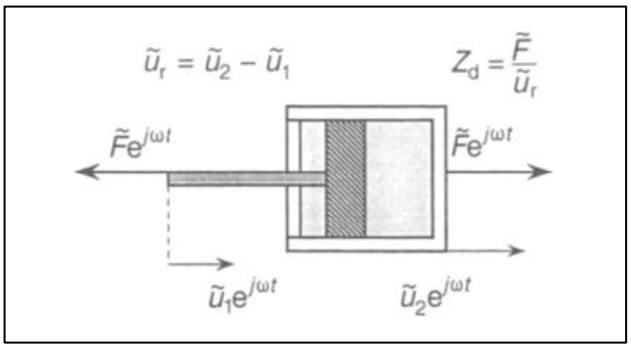

Figure 3.9 - Ideal viscous damper element (Frank J. Fahy, Foundations of Engineering Acoustics*, 2001).*

Its damping rate (or coefficient) C is given by the inverse of the differential velocity u_r of its terminals per unit force applied to either terminal. Hence it can be derived (3.30):

$$Z_m = \tilde{F}/\Delta\widetilde{u_r} = C = Z_d \qquad (3.30)$$

It is characteristically real and positive. It is conventional to represent structural damping by assuming the elastic modulus (or spring stiffness) to be a complex quantity of which the imaginary part is called the 'loss factor'. It represents a

dissipative force proportional to displacement but in phase with velocity. Care should be exercised in using this model because it is strictly invalid for all except harmonic motion.
The impedance of the viscously damped single-degree-of-freedom (s-d-o-f) system is finally explained by the (3.31):

$$Z_m = C + j(\omega M - K/\omega) \qquad (3.31)$$

The resonance frequency of the damped s-d-o-f system, defined as the excitation frequency which produces maximum displacement response, is obtained by maximizing the modulus of the inverse $j\omega Z_m$.

4 The choice of the solver : ANSYS and LSDYNA comparison

4.1 Test case for the comparison

With the aim of numerically simulating flow and stress distributions in the domain object of the study, a previous analysis to choose the software which best reproduced the physics of the real case has been performed. There are many commercial software able to solve computational mechanics and fluid-dynamics problems, already tested by their own producers with classical analytical solutions or benchmark cases to demonstrate that numerical models rightly fit the physics of the real problems. However, considering problems concerning Fluid-Structure Interaction (FSI), most methods and solvers are still to be robustly proved, and so some a priori examinations have to be performed before choosing the right software for each case.

For these reasons, since a Fluid-Structure Interaction issue has to be approached, it has been decided to calibrate some commercial software with a so called "test case" whose exact analytical solution was already provided by previous studies. This case has to nearly represent the details that interested the study assessments but with a simpler model, permitting to recognize which product correctly simulates the nature of the study case with numerical models.

Since this problem involves pressure waves in a porous portion of solid material, whose pores are filled with fluid, it's been necessary to look for a typical benchmark case which similarly treats this Fluid-Solid Interaction due to pressure waves propagating in a fluid fully covered by a solid shell. One of the most popular cases in the Hydraulics about Fluid-Structure Interaction is the study of the propagation of water-hammer waves in conduits. Typically these conduits are filled with water, with a cylindrical geometry and a circular cross section, which can be considered as a thin shell ring of solid material. Those conditions seem to be simpler from the point of view of the geometry and the physics than the original problem, and this allows to proceed with a reliable comparison of the numerical models applied by different software.

Generally FSI solvers use systems of coupled equation between solid and fluid portion. This led to the instance of verifying also which single mechanics and fluid-dynamics solver provided the best set of boundary conditions, in terms of how they numerically approach real cases. In particular, one of the objects of this comparison, is the pursuit of a condition which prevented, or strongly decreased, reflections after the passing of a wave front. That aspect permitted furthermore to compare the results given by numerical models with exact analytical solutions such as the cases of pressure waves propagating in an infinite homogeneous solid bar of circular cross section and in a cylindrical infinite fluid domain.

From these statements it's been decided to divide this first part of the study into three main sections: the analysis of the single solid problem, the examination of the single fluid part, and then the comparison in the FSI field with the conjunction of the two main parts.

4.2 Exact analytical solutions

4.2.1 Fluid-Structure Interaction part

As mentioned before the case of water hammer pressure waves propagation in conduits can nearly represent some important details needed to test in our primary investigation. That's why it has been necessary to look for an exact analytical solution for this type of problem, and with this aim it has been found strongly probative the case analyzed and by Richard Skalak in 1956 with the article "An extension of the theory of water hammer" [10], referring to the previous basic theory of Joukowsky. This theory is in fact considered as a milestone for those fluid-structure interaction problems, and permitted developments such as those promoted by Tijsseling and Zhang with different constraint conditions and pipe thickness [11] [12] [13] [14] [15], and also many numerical codes [16] [17].
The object of his theory was to calculate the magnitude and the speed of pressure waves in both the fluid and the solid part of the system composed by a flexible conduit fully filled with liquid flowing under pressure.
Stress waves in the solid are generated when water hammer waves force the tube to expand radially and therefore, thanks to the so called Poisson effect, creating longitudinal stress waves which are usually faster the those in the fluid, because of the higher density of the solid material.
Skalak primarily made some approximations. He assumed this unsteady problem as one-dimensional, considering the tube domain axisymmetric and infinitely long with radius a and thickness h, the fluid non viscous and both liquid and solid parts were treated as linear elastic bodies. This model also neglects axisymmetric shear deformations and lobar (non-circular) modes of wall vibration. The influence of lobar modes on axial vibration is small at low frequencies because there is no significant oval–axial interaction mechanism. Coupling effects between solid and fluid equations are assumed ruled by the Poisson effect, which links radial expansion of the fluid, due the propagation of the pressure wave, to longitudinal stresses in the tube.
A final constraint has been considered: he obtained this solution for large values of the ratio ct/a , where c is the stress wave speed and t is the time instant. This means that this solution is valid for large distances from the edges of the domain.
Skalak got an analytical solution for this initial-value problem but the expressions are quite complex and almost all subsequent research on water hammer has used a simplified version. This simplified model shown in the equations below, is also called "four equation model" (4.1) and was recently used by Arris S. Tijsseling, from the Department of Mathematics and Computer Science of the Eindhoven University of Technology, to predict water hammer and precursor waves speed and magnitude [18].

$$\frac{\partial V}{\partial t} + \frac{1}{\rho_f}\frac{\partial P}{\partial z} = 0;$$

$$\frac{\partial V}{\partial z} + \left(\frac{1}{K} + \frac{2a}{Eh}\right)\frac{\partial P}{\partial t} - \frac{2\nu}{E}\frac{\partial \sigma_z}{\partial t} = 0; \tag{4.1}$$

$$\frac{\partial \dot{u}_z}{\partial t} - \frac{1}{\rho_s}\frac{\partial \sigma_z}{\partial z} = 0;$$

$$\frac{\partial \dot{u}_z}{\partial z} - \frac{1}{E}\frac{\partial \sigma_z}{\partial t} + \frac{v}{E}\frac{a}{h}\frac{\partial P}{\partial t} = 0 .$$

So far, applied to water hammer problems, Tijsseling demonstrated the validity of this model giving same wave speeds of the complete model, and according also to measured pressures and stresses (Dynamic Failure of Materials and Structures, Arun Shukla, Guruswami , 2009).
In the simple model bending stresses, shear effects and rotatory inertia are neglected. But the main difference is the absence of an equation of motion for the radial inertia of the tube, and so radial stresses are converted into longitudinal stresses directly by the Poisson coefficient. This equation led in the full model to dispersive effects and to the spreading of the wave front sharpness with time, while in the simple model the front remain sharp.
In his work, Skalak considered a fluid of density ρ_0 and elasticity K, the tube wall material has density ρ_s, elasticity E and a Poisson's ratio of ν.
The assumed non-equilibrium situation at time t = 0 is shown in (Figure 4.1).

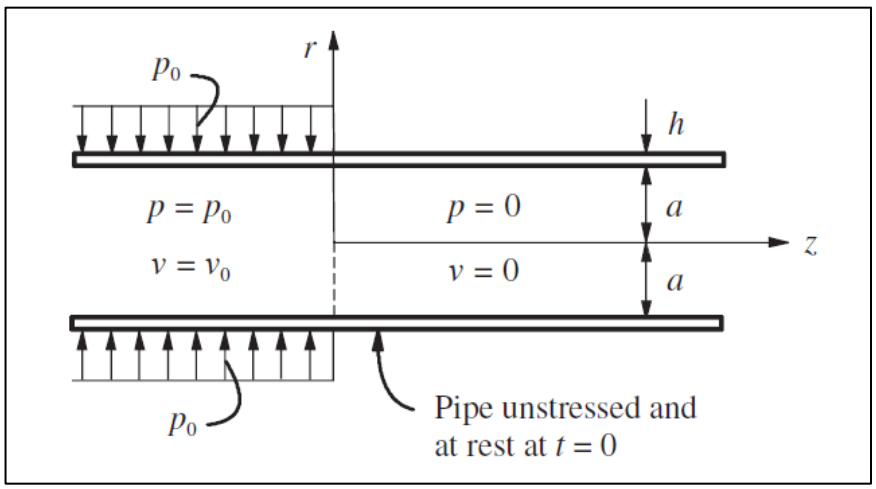

Figure 4.1 - Non-equilibrium situation at time t = 0 (A. Tijsseling, "Skalak's extended theory of water hammer",2008).

The pressure p and axial fluid velocity v have positive initial values p_0 and v_0 in the left half of the tube (z<0), respectively, related by (4.2):

$$p_0 = \rho_0 c v_0 \qquad (4.2)$$

where c is given by (4.3)

$$c = \sqrt{\frac{K}{\rho_0}}. \qquad (4.3)$$

All other pressures, velocities and displacements are zero. These initial conditions correspond to a step wave moving in the positive axial direction (z=0) at speed c. The wave would propagate in an unchanged form in a pipe with entirely rigid walls, but not so in a pipe with elastic walls.
Skalak used the following data in his test problem: a = 0.3048 m, h = 4.857 mm, ρ_0 = 999.8 kg/m^3, K = 2.322 GPa, ρ_s = 7849 kg/m^3, E = 206.8GPa, ν = 0.3, and herein p_0 = 100 kPa. Thus, c = 1524 m/s and v_0 = 0.06563 m/s.
Skalak applied Fourier and Laplace transforms to find dispersion relationships for the modes of free vibration of the coupled fluid–pipe system. He applied inverse Fourier and Laplace transforms to arrive at solutions in the form of single indefinite integrals of real-valued functions. The integrals were too difficult to solve exactly, but Skalak was able to find asymptotic solutions for large values of axial distance z and time t. He calculated the speed of water hammer and precursor waves (4.4), in this work indicated respectively with index 1 and 2:

$$c_{1,2} = c\left\{\frac{2AR + R + R^2(1-\nu^2) \mp \sqrt{[2AR + R + R^2(1-\nu^2)]^2 - 4R^2(1-\nu^2)(2A+R)}}{2(2A+R)}\right\}^{1/2} \tag{4.4}$$

where c_1 has the minus sign and c_2 the plus sign, and where

$$A = \frac{\rho_0}{\rho_s}\frac{a}{h}\,, R = \left(\frac{c_0}{c}\right)^2 \tag{4.5}$$

with c_0 defined below (4.6).
To be sure about the reliability of these values, Tijsseling provided the following relations [19] previously used to evaluate the wave speed in the fluid and in the solid domains,

$$c_e = \frac{c}{\sqrt{1 + (2Ka/Eh)}}\,, c_0 = \sqrt{\frac{E}{\rho_s(1-\nu^2)}} \tag{4.6}$$

where c_e is the Korteweg formula, and we can see that c_1 is an extended version of this expression, and c_0 is the common form for the wave speed in thin plates.
Considering these oscillations with a non-dimensional approach, Skalak introduced a dimensionless distance relative to the wave front, expressed as follows (4.7) where index n = 1,2.

$$z_n^* = (z - c_n t)/\sqrt[3]{d_n t} \tag{4.7}$$

The constants d_n are defined by the relation (4.8)

$$d_n = ca^2\left\{\frac{(A+4)[(c_n/c)^5 - (c_n/c)^3(1+R) + (c_n/c)R\,]}{-16(c_n/c)^2(2A+R) + 8R(2A+1) + 8R^2(1-\nu^2)}\right\} \tag{4.8}$$

He also expressed (4.9) the wave height with the non-dimensional parameter $I(\beta_n)$ with $Ai(\xi)$ expressing the Airy function of the first type:

$$I(\beta_n) = \frac{1}{2} - \frac{1}{\pi}\int_0^{\pm\infty} \frac{\sin(\eta + \beta_n \eta^3)}{\eta} d\eta \qquad (4.9)$$

$$= \frac{1}{3} - \int_0^{1/\sqrt[3]{3\beta_n}} Ai(\xi) d\xi$$

which has been drawn as a function of $z_n^* = 1/\sqrt[3]{3\beta_n}$ with

$$\beta_n = \frac{d_n t}{(z - c_n t)^3} \qquad (4.10)$$

The upper bound in the first integral is $+\infty$ for $\beta_n > 0$ and $-\infty$ for $\beta_n < 0$. Three integrals can be calculated analytically and their results are shown below (4.11).

$$I(0^-) = 1, I(0^+) = 0 \ \ and \ I(\pm\infty) = {}^1/_3 \qquad (4.11)$$

Plotting these two dimensionless variable Skalak obtained the following wave form, as we can see from the chart of figure (Figure 4.2).

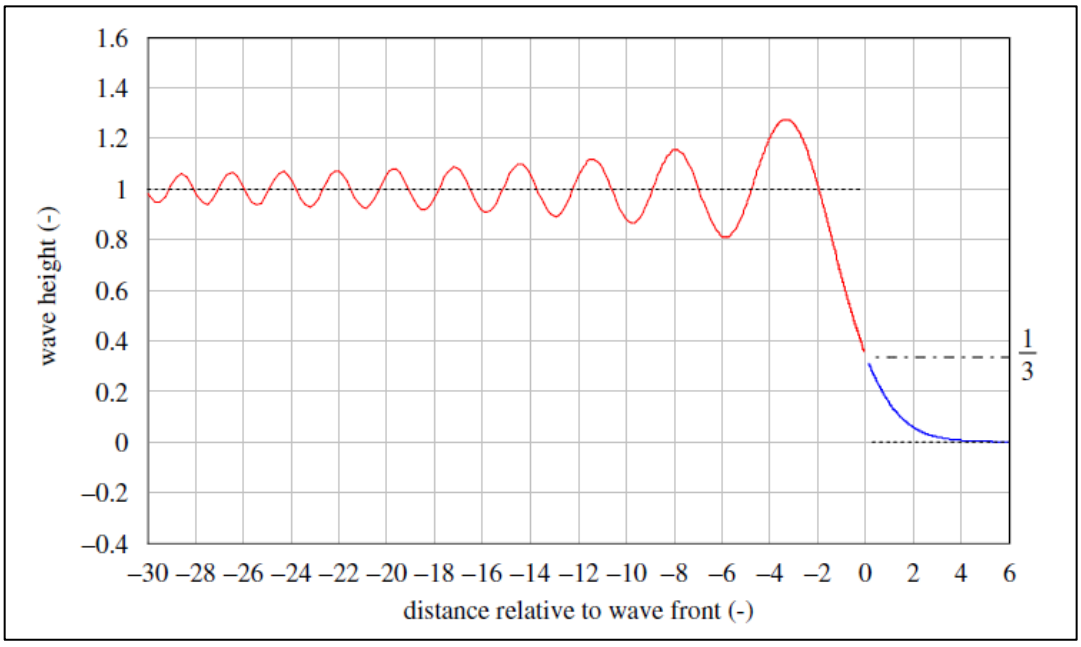

Figure 4.2 - Dimensionless wave height (A. Tijsseling, "Skalak's extended theory of water hammer",2008).

The dimensional pressure for water hammer (n = 1) and precursor (n = 2) waves travelling in the positive z direction is finally evaluated through the relations below (4.12) (up to a constant, vertical shift):

$$p_n(\beta_n) = Cp_n Cw_n \int_0^{\pm\infty} \frac{\sin(\eta + \beta_n \eta^3)}{\eta}\, d\eta \qquad (4.12)$$

with

$$Cp_n = 2\rho_0 c_n^2/a[(c_n^2/c^2) - 1], \quad Cw_n = p_0/\pi\rho_s h(c_n/c - 1)\, D_n\,, \qquad (4.13)$$

$$D_n = 4\rho_0 c_n^4/\rho_s h c^2 a\left((c_n^2/c^2) - 1\right)^2 + 2c_0^2[\nu^2/(1 - c_0^2/c_n^2)^2 + 1 - \nu^2]/a^2$$

4.2.1.1 Solid part

In engineering applications, for example in machinery, it is often required to transmit a signal from one position to another. Very often the transmission is accomplished through a cylindrical rod. In such cases it may be necessary to take into account wave propagation effects if the signal varies rapidly in time. The most elementary theory capable of describing the propagation of longitudinal pulses in a rod, composed by a linear elastic solid material, is governed by the following equation (4.14), based on the assumption of a one-dimensional state of stress in the rod [20].

$$\frac{\partial^2 w}{\partial z^2} = \frac{\rho}{E} \frac{\partial^2 w}{\partial t^2} \tag{4.14}$$

Here *w* is the axial displacement, z is the space axial coordinate, ρ and *E* are the mass density and Young's modulus, respectively. Since this is a simple one-dimensional wave equation with no damping terms, it predicts that a pulse does not change shape as it propagates along the rod.
Skalak [20] [21] [22] chose a system of cylindrical coordinates with the z-axis coinciding with the axis of the cylinder. The expressions relating the radial displacement *u(r,z,t)* and the axial displacement *w(r,z,t)*, components of the displacement vector *u*, to the displacement potentials getting the expressions (4.15):

$$\begin{aligned} u &= \frac{\partial \varphi}{\partial r} - \frac{\partial \psi}{\partial z} \\ w &= \frac{\partial \varphi}{\partial z} - \frac{1}{r} \frac{\partial (r\psi)}{\partial r} \end{aligned} \tag{4.15}$$

where φ and ψ are the scalar and the vector potentials respectively, defined by the following relation.

$$\boldsymbol{u} = \nabla\varphi + \nabla \times \boldsymbol{\psi} \tag{4.16}$$

Potentials must satisfy the previous wave equation giving (4.17),

$$\begin{aligned} \nabla^2 \varphi &= \frac{1}{c_L^2} \frac{\partial^2 \varphi}{\partial t^2} \\ \nabla^2 \psi - \frac{1}{r^2} \psi &= \frac{1}{c_T^2} \frac{\partial^2 \psi}{\partial t^2} \end{aligned} \tag{4.17}$$

where

$$\nabla^2 = \frac{\partial^2}{\partial r^2} + \frac{1}{r} \frac{\partial}{\partial r} + \frac{\partial^2}{\partial z^2} \tag{4.18}$$

is the Laplace operator in cylindrical coordinates, and

$$c_L^2 = \frac{\lambda + 2\mu}{\rho}$$
$$c_T^2 = \frac{\mu}{\rho} \tag{4.19}$$

are the longitudinal and the transverse wave speed respectively (4.19), with λ and μ Lamè parameters. The pertinent components of the stress tensor are (4.20):

$$\tau_r = \lambda\nabla^2\varphi + 2\mu\frac{\partial}{\partial r}\left[\frac{\partial\varphi}{\partial r} - \frac{\partial\psi}{\partial z}\right]$$
$$\tau_{rz} = \mu\left[\frac{\partial}{\partial z}\left(\frac{\partial\varphi}{\partial r} - \frac{\partial\psi}{\partial z}\right) + \frac{\partial}{\partial r}\left[\frac{\partial\varphi}{\partial z} - \frac{1}{r}\frac{\partial(r\psi)}{\partial r}\right]\right] \tag{4.20}$$
$$\tau_z = \lambda\nabla^2\varphi + 2\mu\frac{\partial}{\partial z}\left[\frac{\partial\varphi}{\partial z} - \frac{1}{r}\frac{\partial(r\psi)}{\partial r}\right].$$

Solutions to these equations must satisfy boundary conditions at the end of the rod and at the lateral surface. From this we have (4.21).

$$\begin{aligned} &\text{at } z = 0\,, \quad 0 \le r \le a && \tau_z(r,0,t) = -PH(t) \\ & && u(r,0,t) = 0 \\ &\text{at } r = a\,, \quad z \ge 0 && \tau_z(r,a,t) = 0 \\ & && \tau_{rz}(r,a,t) = 0\,. \end{aligned} \tag{4.21}$$

Where *H(t)* is the common Heaviside step function. A further condition is that the displacements and the stresses, hence the potentials vanish at infinity ($z \to \infty$). Since the rod is at rest prior to time t = 0 the initial conditions (4.22) are

$$\varphi(r,z,0) = \dot{\varphi}(r,z,0) = \psi(r,z,0) = \dot{\psi}(r,z,0) \equiv 0\,. \tag{4.22}$$

Combining these relations together, the boundary conditions for this problem at *z = 0* can be subsequently written as follows (4.23).

$$\rho\ddot{\varphi} = -PH(t)$$
$$\frac{\partial\psi}{\partial z} = 0 \tag{4.23}$$

The particle velocity in the axial direction,

$$V(r,z,t) = \frac{\partial w}{\partial t} \tag{4.24}$$

has been considered in some detail. In terms of the displacement potentials, V assumes this form:

$$V(r,z,t) = \frac{\partial}{\partial z}\left(\frac{\partial\varphi}{\partial t}\right) + \frac{1}{r}\frac{\partial}{\partial r}\left(r\frac{\partial\psi}{\partial t}\right). \tag{4.25}$$

In his analysis Skalak applied the cosine Fourier transform, the Laplace transform, and then he inverted the two transforms to obtain, passing through the frequency equation of longitudinal motions of a rod (Pochhammer-Chree equation), this exact relation for the particle velocity:

$$V = \frac{\lambda}{\lambda+2\mu}\frac{P}{\mu}\sum_{n=1}^{\infty} I_n \tag{4.26}$$

where

$$I_n = -\frac{4i}{\pi}\int_0^{\infty} \xi^2 M_n(\omega_n\xi)\sin(\omega_n t)\cos(\xi z)d\xi \tag{4.27}$$

with M_n function of the n-th mode of vibration ω_n and the wave number ξ.
Evaluating this equation for large times and for low frequencies, Skalak deduced the following expression for the lowest longitudinal mode:

$$I_1 = -\frac{\mu}{\lambda}\frac{c_L^2}{c_b}\left[J_1 + J_2\right] \tag{4.28}$$

with c_b speed of a wave propagating in an infinite rod defined as $\sqrt{E/\rho}$.
The terms J_1 and J_2 are respectively:

$$J_1 = \frac{1}{\pi}\int_0^{\infty}\frac{\sin[\xi(z-c_b t)+\gamma\xi^3 t]}{\xi}d\xi$$
$$J_2 = \frac{1}{\pi}\int_0^{\infty}\frac{\sin[-\xi(z+c_b t)+\gamma\xi^3 t]}{\xi}d\xi \tag{4.29}$$

with

$$\gamma = \frac{1}{4}\nu^2 c_b a^2 \tag{4.30}$$

and operating a change of variable become:

$$\begin{aligned} J_1 &= \frac{1}{\pi}\int_0^\infty \frac{\sin[q_1\eta + \eta^3/3]}{\eta}\,d\eta \\ J_2 &= \frac{1}{\pi}\int_0^\infty \frac{\sin[q_2\eta + \eta^3/3]}{\eta}\,d\eta \end{aligned} \tag{4.31}$$

where

$$q_1 = \frac{z - c_b t}{(3\gamma t)^{\frac{1}{3}}} \quad , \quad q_2 = -\frac{z + c_b t}{(3\gamma t)^{\frac{1}{3}}} \tag{4.32}$$

Recognizing the Airy integrals of the first type

$$Ai(q_i) = \frac{1}{\pi}\int_0^\infty \cos(q_i\eta + \eta^3/3)\,d\eta \tag{4.33}$$

then he evaluated J_1 and J_2 as

$$\begin{aligned} J_1 &= \int_0^{q_1} Ai(s)ds + \frac{1}{6} \\ J_2 &= \int_0^{q_2} Ai(s)ds + \frac{1}{6}. \end{aligned} \tag{4.34}$$

Once evaluated the particle velocity *V*, Skalak plotted his results obtaining the following chart (Figure 4.3).

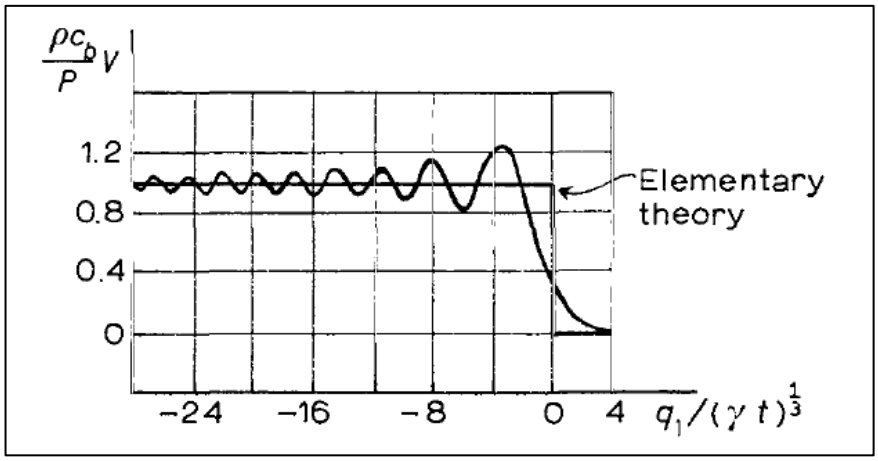

Figure 4.3 - Comparison between Skalak's theory and elementary theory (J. D. Achenbach, "Wave propagation in elastic solids", 1973) [20].

For small values of t the integrals vanish. Thus, the results show that some distance ahead and some distance behind the wave front $z = c_b t$ the improved approximation agrees with the elementary theory.
Then the stress in the axial direction is finally estimated with the following relation [22]:

$$\sigma_z(z,t) = c_b \rho \, V(z,t) \tag{4.35}$$

4.2.1.2 Fluid part

With the aim of calibrating the fluid solvers, it has been decided to find an exact solution for the problem involving the one dimensional propagation of pressure waves into an homogeneous domain, which in our case is a fluid domain.
This problem has been solved by J. B. d'Alembert in 1747 [23], obtaining a solution (4.37) for the the following general one dimensional equation for propagating sound waves (4.36):

$$\frac{\partial^2 u}{\partial z^2} = \frac{\rho}{E} \frac{\partial^2 u}{\partial t^2} \tag{4.36}$$

which is

$$u(z,t) = \frac{1}{2}[f(z-ct) + f(z+ct)] \tag{4.37}$$

with $c = \sqrt{E/\rho}$ expressing the wave speed in an homogeneous medium.
Since pressure waves can be considered as sound waves, then equation (4.38) can be accepted also with the pressure *p(x,t)* as unknown, therefore our solution has to be in the form:

$$p(z,t) = \frac{1}{2}[f(z-ct) + f(z+ct)] \tag{4.38}$$

where $f(z-ct)$ and $f(z+ct)$ are both wave functions, the first representing a progressive wave and the second a regressive one, with *f* assuming the form of the decided perturbation.
In the other test cases the propagation of an Heaviside step function has been considered, then in this situation the function *f(z,t)* has the following form:

$$f(z,t) = \begin{cases} P, & z - ct \leq 0 \\ 0, & z - ct > 0 \end{cases} \tag{4.39}$$

However this function has a discontinuity in z = 0, as it can be seen from (4.39), which is difficult for computer solvers to treat, that's why a representation through a Fourier integral series of continuous harmonics has been adopted.

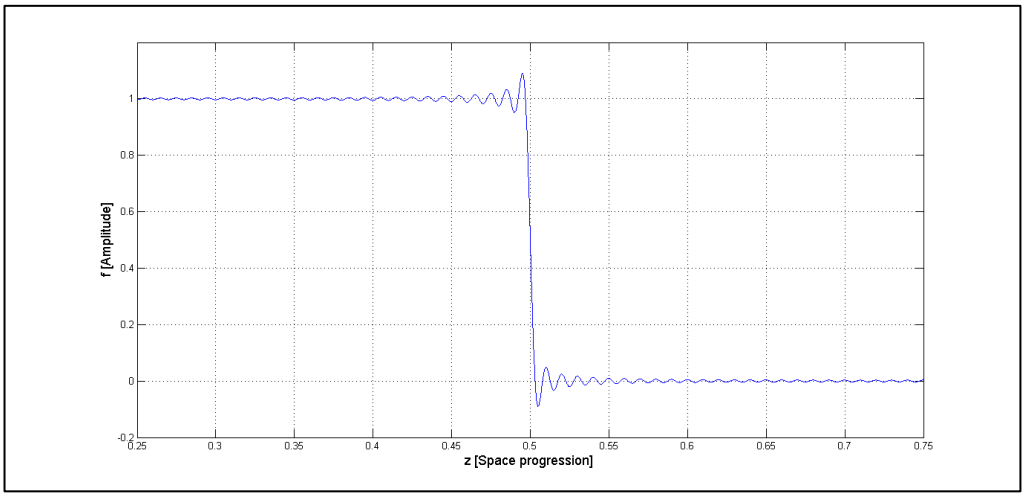

Figure 4.4 - Representation of f(z-ct) in a fixed time t.

As shown in the picture before (Figure 4.4), the Fourier expansion into harmonic functions produces oscillations in the sections after the arrival of the wave front and also before, which are not truly representing what really happens in the fluid (Figure 4.5). With the expansion of the term *f(z+ct)* oscillations around zero are obtainable, at a fixed time, in all the z-coordinates in the proximities of the wave front and therefore also before the wave front. Also those oscillations are not physically possible, but, taking the number of harmonics to infinite, which is numerically impossible, it would result the ideal solution of a moving step of assigned amplitude along the domain.

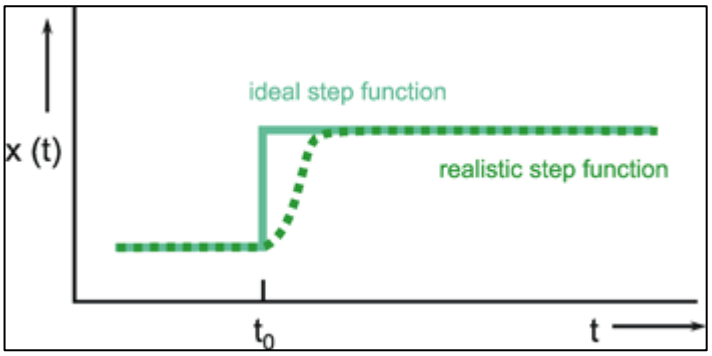

Figure 4.5 - Difference between what really happens when a step perturbation is applied and what should theoretically happen, here varying in time with a fixed space coordinate (http://www.brains-minds-media.org).

That's why it has been decided to use, as an analytical comparison with the numerical results, the Skalak's FSI solution with particular conditions, which reduces to zero the spurious oscillations before the incoming of the wave front, and permits to analyze correctly what happens behind it.
Therefore, taking into account our FSI solution, provided by the analysis of Skalak and Tijsseling previously described in this work, if a particular geometry for the solid tube is considered it is observable that the solid domain no longer effects the fluid domain, yielding to the exact researched solution.

As a matter of fact it can be seen from the previously cited Korteweg formula that taking the Young's Modulus of the tube to infinity the wave speed the value of c is obtainable, which is the wave speed in a fluid domain with a rigid solid boundary.
Then, with the same method illustrated in the FSI exact solution analysis but inserting these new data for the solid domain, it can again be reached the same non-dimensional chart for the wave height illustrated in Figure 4.2.
Than we needed to evaluate the fluid pressure with the product of the coefficients C_{p1} and C_{w1} presented in the FSI analysis.
Acting like this it is finally obtained the desired solution for the one dimensional propagation of pressure waves into a fluid undisturbed domain.

4.3 Overview of the software

With regard to this comparison, it has been decided to use two different commercial software. One, which is the more commonly used for numerical computations of this type, is the ANSYS package of software, with ANSYS Mechanical for the resolution of the solid part of our model and ANSYS CFX for the fluid part. The other is LS-DYNA, less known than the first, but useful for those type of transient dynamics problems for both fluid and solid domains.

4.3.1 ANSYS Mechanical

ANSYS Mechanical solves most of the typical solid mechanics problems thanks to the presence of many packages approaching in different ways the variety of possible issues. Since we can consider our original porous soil sample small with respect to the wave pressure speeds and periods taken in count, we needed a package containing a boundary condition which prevented from reflection, or significantly decreased it, of a wave encountering a wall of our domain. We found this boundary condition in the pack named Explicit Dynamics.
The Explicit Dynamics system enable the possibility to simulate nonlinear structural mechanics application involving impacts, stress wave propagation, high frequency dynamic response, shock wave propagation through liquid and solid domains and rigid or flexible bodies [24]. This system (4.40) solves the partial differential equations, shown below, that express the conservation of momentum, relating the acceleration to the stress tensor.

$$\begin{aligned} \rho\ddot{x} &= b_x + \frac{\partial\sigma_{xx}}{\partial x} + \frac{\partial\sigma_{xy}}{\partial y} + \frac{\partial\sigma_{xz}}{\partial z} \\ \rho\ddot{y} &= b_y + \frac{\partial\sigma_{yx}}{\partial x} + \frac{\partial\sigma_{yy}}{\partial y} + \frac{\partial\sigma_{yz}}{\partial z} \\ \rho\ddot{z} &= b_z + \frac{\partial\sigma_{zx}}{\partial x} + \frac{\partial\sigma_{zy}}{\partial y} + \frac{\partial\sigma_{zz}}{\partial z} \end{aligned} \qquad (4.40)$$

These are combined with the conservation of energy expressed via (4.41):

$$\ddot{e} = \frac{1}{\rho}\left(\sigma_{xx}\dot{\varepsilon}_{xx} + \sigma_{yy}\dot{\varepsilon}_{yy} + \sigma_{zz}\dot{\varepsilon}_{zz} + 2\sigma_{xy}\dot{\varepsilon}_{xy} + 2\sigma_{yz}\dot{\varepsilon}_{yz} + 2\sigma_{zx}\dot{\varepsilon}_{zx}\right) \qquad (4.41)$$

Through the nodes notion and the mesh deformation the solver obtains the strains. These, thanks to the material properties and to constitutive laws, are used to get stresses, which are in turn included, with body forces from boundary conditions, in the conservation of the momentum to extract the accelerations. Integrating these explicitly in time with discrete time steps we finally obtain velocities and displacements. This is clearly a cycle which is repeated for each element of the model until a user defined time is reached.

4.3.2 ANSYS CFX

ANSYS CFX is a computer-based tool for simulating the behavior of system involving fluid flow, heat transfer of other related problems. It works by solving the equations of fluid flow over a region of interest with specified conditions on the boundary of that region. Those equations are the unsteady Navier-Stokes in their conservation form [25]. The instantaneous equations of mass, momentum and energy conservation can be written as follows (4.42).

$$\frac{\partial \rho}{\partial t} + \nabla \cdot (\rho \boldsymbol{U}) = 0$$

$$\frac{\partial (\rho \boldsymbol{U})}{\partial t} + \nabla \cdot (\rho \boldsymbol{U} \otimes \boldsymbol{U}) = -\nabla p + \nabla \cdot \tau + \boldsymbol{S}_M \tag{4.42}$$

$$\frac{\partial (\rho h_{tot})}{\partial t} - \frac{\partial p}{\partial t} + \nabla \cdot (\rho \boldsymbol{U} h_{tot}) = \nabla \cdot (\lambda \nabla T) + \nabla \cdot (\boldsymbol{U} \tau) + \boldsymbol{U} \cdot \boldsymbol{S}_M + \boldsymbol{S}_E$$

Where h_{tot} is the total enthalpy related to static enthalpy h(T,p) by :

$$h_{tot} = h + \frac{1}{2}\boldsymbol{U}^2 \tag{4.43}$$

ANSYS CFX gives numerical solution to Navier-Stokes equation through algebraic approximations. It uses an element-based finite volume method which discretize the spatial domain with a mesh. Equations are integrated over each control volume after discretizing in time volumes and surfaces integrals.

4.3.3 LS-DYNA

LS-DYNA is a general purpose finite element code for analyzing the large deformation static and dynamic response of structures including structures coupled to fluids. The main solution methodology is based on explicit time integration. A contact-impact algorithm allows difficult contact problems to be easily treated with heat transfer included across the contact interfaces. By a specialization of this algorithm, such interfaces can be rigidly tied to admit variable zoning without the need of mesh transition regions [26].
The governing equations in the first formulation are the three balance equations that describe the conservation of mass, momentum and energy, combined with constitutive relations of the material. The numerical solution is achieved thanks to discretization in space (Finite Elements) and time (central difference 2nd order accurate time integration scheme). In this case the nodes of the mesh are attached to the imaginary material "points" and move and deform with the material.
In the Eulerian and ALE-formulations the nodes do not follow the material flow, but there is flux of material between the elements. So, LS-DYNA first computes the Lagrangian time derivative and updates the history variables. Subsequently the relative motion between mesh and material is computed and the history variables are updated once more (mesh smoothing and advection step). Both spatially 1st and 2nd order accurate advection algorithms are available. Furthermore in Eulerian and ALE-formulation it is possible to allow two or more materials in one element in a

fixed mesh (Multi Material ALE – MMALE – method). This last resource is often used in fluid-structure interaction, where two (or more) materials have to be defined within the Eulerian/ALE mesh: the first one in the elements constrained by the Lagrangian structure and the second one in the surrounding elements.
In fluid-structure interaction is generally suitable to treat parts of a model as Lagrangian and other parts as Eulerian or with an ALE-formulation. Since the two types of mesh don't share nodes, a coupling algorithm is needed to define the contact interfaces between the Lagrangian mesh and the materials defined in the Eulerian mesh.

4.4 Fluid Dynamics solver evaluation

4.4.1 Fluid domain and mesh

In order to compare the analytical solution to a numerical computation of a shock wave propagating in a compressible inviscid fluid, contained in an infinite long pipe with rigid walls, the domain shown in
Figure 4.6 has been created. The pipe length is assumed to be 100 times the diameter of the tube to simulate the infinite length condition. Since the problem is axially symmetrical, the domain is reduced to one quarter and the appropriate symmetry conditions are defined. The fluid has initially null velocity and the pressure is equal to the reference pressure. A coarse mesh (Figure 4.7) and a finer mesh (Figure 4.8) have been simulated.

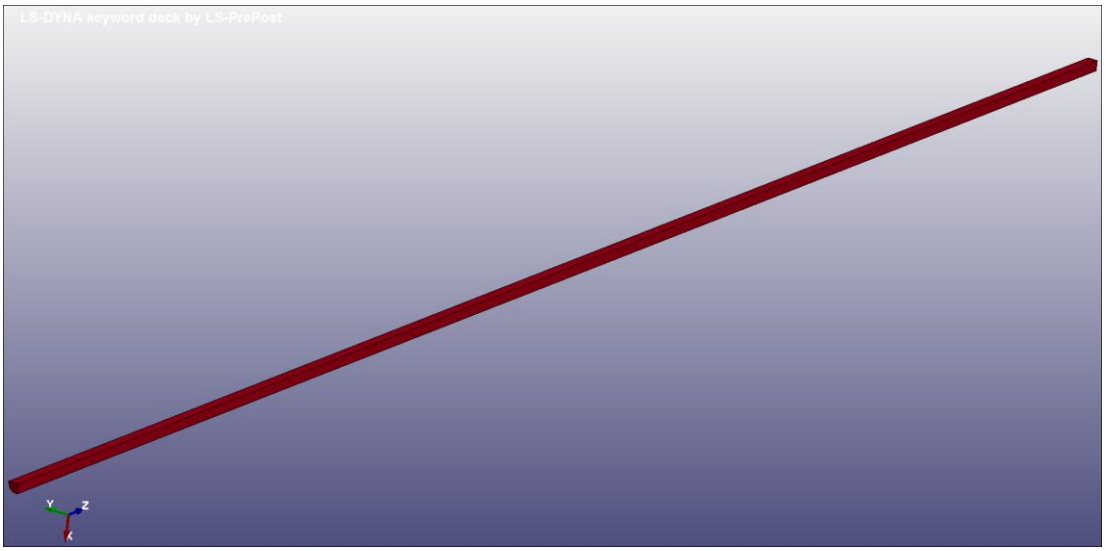

Figure 4.6 - LS-DYNA long pipe fluid domain.

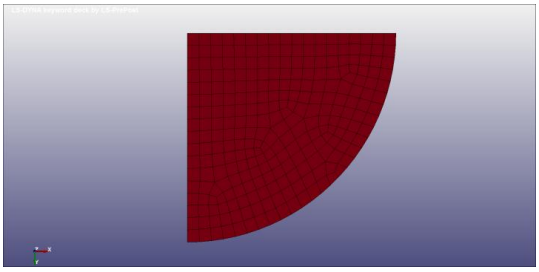

Figure 4.7 - LS-DYNA coarser fluid mesh.

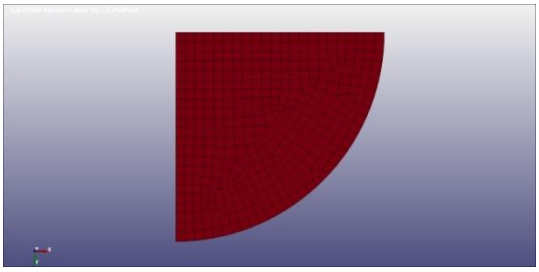

Figure 4.8 - LS-DYNA finer fluid mesh.

Geometry and material properties

The geometrical dimensions of the domain and the fluid properties used in the simulations are listed in Table 4.1. Since the analyzed fluid is compressible, an equation of state has been chosen. Liquids in LS-DYNA may be modeled, if deformation is in the nonlinear range, using Gruneisen EOS, that relates the change in pressure to the change in the corresponding specific internal energy. The general form of the equation is reported in (4.44):

$$p = \frac{\rho_0 C^2 \mu \left[1 + \left(1 - \frac{\gamma_0}{2}\right)\mu - \frac{a}{2}\mu^2\right]}{\left[1 - (S_1 - 1)\mu - S_2 \frac{\mu^2}{\mu+1} - S_3 \frac{\mu^3}{(\mu+1)^2}\right]^2} + (\gamma_0 + a\mu)E \qquad (4.44)$$

Where C is the intercept of the v_s-v_p curve (shock velocity-particle velocity); S_1, S_2 and S_3 are the slope dimensionless coefficients of the v_s-v_p curve; γ_0 is the dimensionless Gruneisen gamma; a is the first order volume correction to γ_0; and $\mu = \rho/\rho_0 - 1$. In Figure 4.9 is shown the comparison between two different equations of state for the analyzed fluid: Gruneisen and Tait EOS.

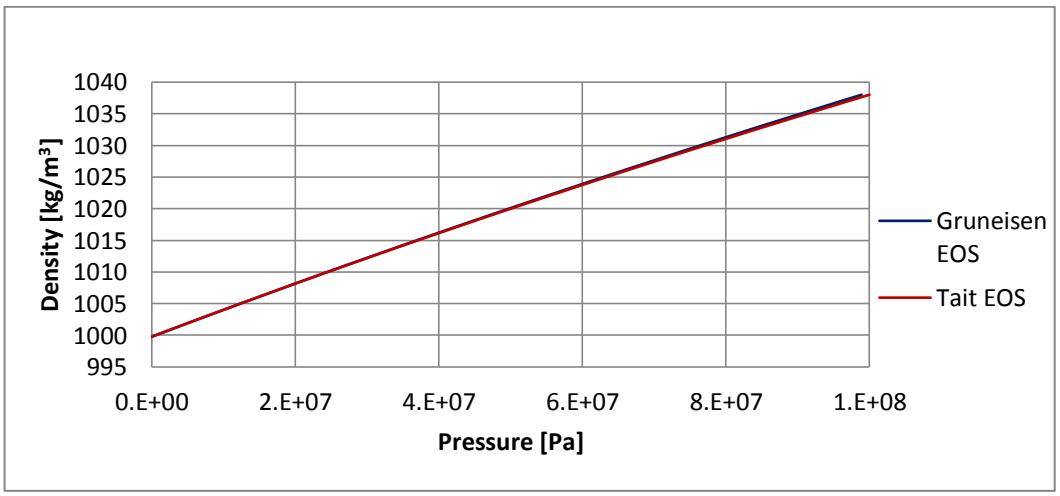

Figure 4.9 - Comparison between two different equations of state. The graph is obtained using the properties of water in Table 4.1.

Quantity	Symbol	Value	Unit
Length	L	60	m
Radius	R	0.3048	m
Diameter	D	0.6096	m
Density	ρ	999.8	kg/m^3
Dynamic viscosity	μ	0	kg/(m·s)
Equation of state	EOS	Gruneisen	-
Sound velocity of material	C	1524	m/s
Coefficients of the slope of the v_s-v_p curve	S1	1.92	-
	S2 = S3	0	-
Gruneisen gamma	γ_0	0.1	-
Volume correction to γ_0	a	0	-
Initial internal energy	E_0	1.00E+06	Pa
Initial relative volume	V_0	1	-
Reference pressure	P_{ref}	1.00E+05	Pa

Table 4.1 - Geometry of the simulated domain and material properties.

4.4.2 Mesh

In Table 4.2 are reported the main properties of the two discretizations of the domain, such as number, size and type of cells.

	Mesh 1	Mesh 2
Nr. of nodes	970194	1851984
Nr. of elements	863247	1680112
Max characteristic length [m]	0.018	0.014
Element type	Hexahedron	Hexahedron
Nr. of elements on radius	18	22
Nr. of elements on axial length	3333	4286

Table 4.2 - Features of the two simulated meshes.

4.4.3 Loads and boundary conditions

Table 4.3 describes the pressure load (Figure 4.10) due to the shock wave and the boundary conditions.

Location	Boundary condition/load	Features
Inlet	Shock wave of magnitude 1.00E+05 Pa	See Figure 4.10
Outlet	Non-reflecting boundary condition	Acts on dilatational and shear waves
XZ plane	Symmetry	1 translational constraint (y-direction) 3 rotational constraint
YZ plane	Symmetry	1 translational constraint (x-direction) 3 rotational constraint
Symmetry axis	Symmetry	2 translational constraint (x and y dir.) 3 rotational constraint
Wall	No slip	Fixed nodes

Table 4.3 - Applied loads and boundary conditions.

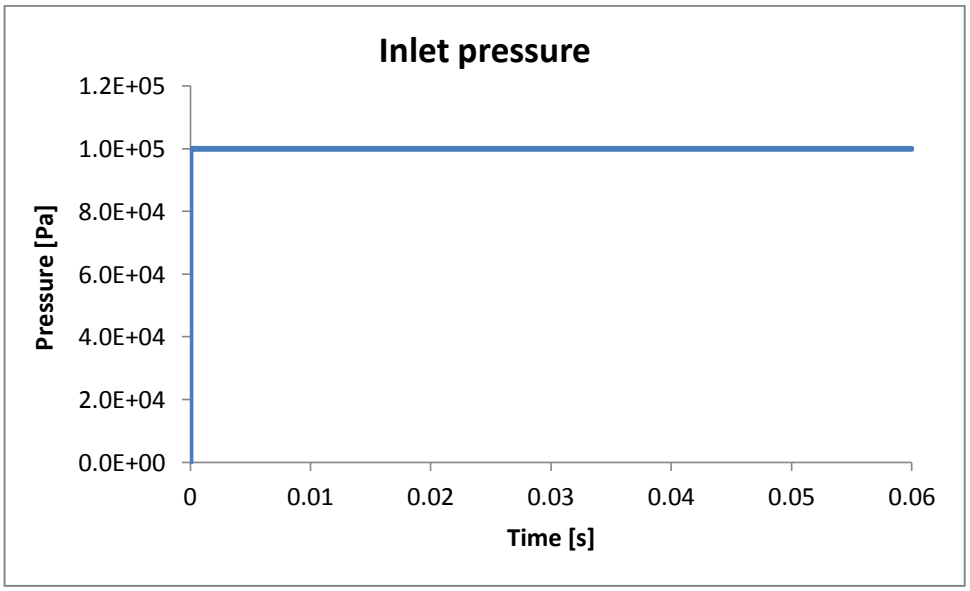

Figure 4.10 - Pressure load applied at inlet.

4.4.4 Simulation settings

In Table 4.4 the numerical methods and the time discretization are reported.

End time	0.06 s
Time step	Mesh 1 : 5.45E-06 s Mesh 2 : 4.63E-06 s
Integration method (time)	Central difference 2nd order accurate scheme
Advection method (space)	Van Leer, 2nd order accurate method
Element formulation	ALE multi-material element

Table 4.4 - Main settings of the simulations.

4.4.5 Computational aspects

Table 4.5 shows the computational costs related to the core number and mesh size.

	Mesh 1	**Mesh 2**
Execution	Distributed memory parallel (MPP)	Distributed memory parallel (MPP)
Core number	4	4
Precision	Double	Double
Simulation time	14156 s = 3.9 h	25981 s = 7.2 h
Mesh size	$\sim 9 \times 10^5$ elements	$\sim 2 \times 10^6$ elements

Table 4.5 - Main characteristics of the simulation process.

4.4.6 Results

In Figure 4.11 are shown the results obtained with the software LS-DYNA with two different meshes compared with the exact analytical solution. It can be seen from the chart that with a finer mesh, in our case mesh 2, the numerical solution tend to the exact one. Since the analytical solution is obtained by fixing the hypothesis that the tube is infinitely rigid, which in practical models is impossible to realize, it can stated that the wave speed difference seen in the chart between numerical and exact solution is mainly due to the inability to create a model with the same features of the theoretical one, but refining the mesh it is only possible to tend and not to reach the analytical solution.

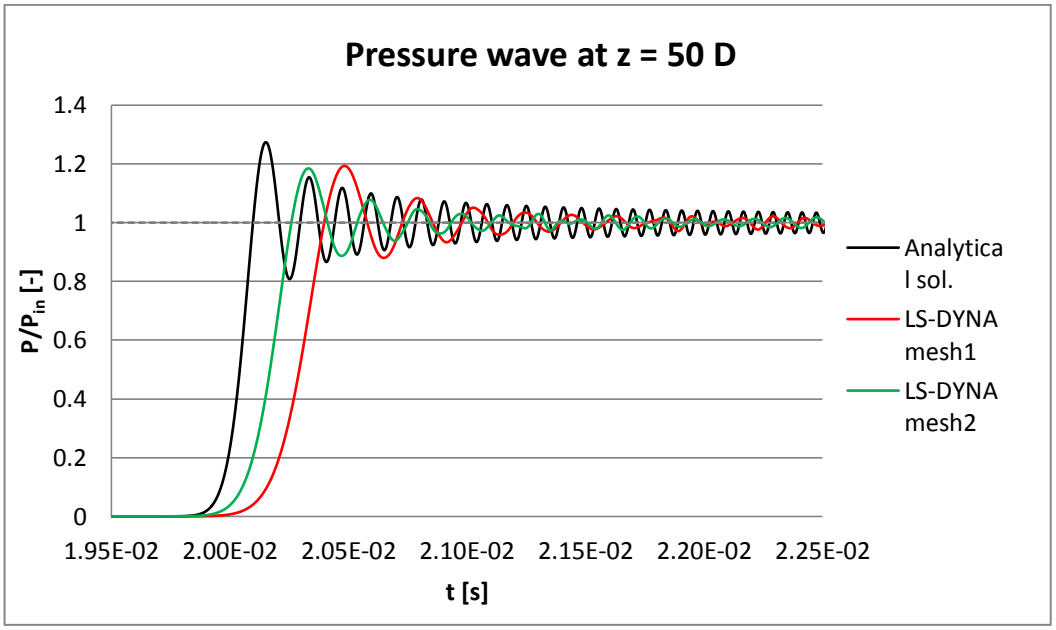

Figure 4.11 - Normalized fluid pressure at the cylinder axis (z = 50D): comparison between analytic solution and LS-DYNA simulations with different meshes.

4.4.7 ANSYS CFX simulation description

The same shock wave propagating in the fluid contained in a rigid wall pipe has been analyzed with ANSYS CFX. In order to obtain analogous results, the geometry of the domain, the material properties, the loads, the boundary conditions and the mesh are identical (the finer mesh was chosen for the comparison, indicated as Mesh 2). The main difference lies in the simulation process. For more details, refer to Table 4.6 and Table 4.7.

End time	0.01 s
Time step	Mesh 2 : 1.00E-05 s
Integration method (time)	Second Order Backward Euler
Advection method (space)	High Resolution

Table 4.6 - Main settings of CFX simulation.

Execution	HP MPI Local Parallel
Core number	8
Precision	Double
Simulation time	3.60E+05 s = 100 h
Mesh size	~2x10^6 elements

Table 4.7 - Main characteristics of CFX simulation process.

4.4.8 Comparison between LS-DYNA, ANSYS CFX and exact analytical solution

In Figure 4.12 are resumed the results obtained for the previous descripted simulations with the chosen numerical solvers and the exact analytical solution for this problem. A gauge point at the distance of twenty diameters from the inlet section has been chosen to see the main differences between the three series. It can be seen that ANSYS CFX almost captured the position of the wave front but there are spurious oscillations which would lead us to refine the mesh with consequent bigger simulation times. By the other hand LS-DYNA also catch quite well the front position but without spurious oscillations.

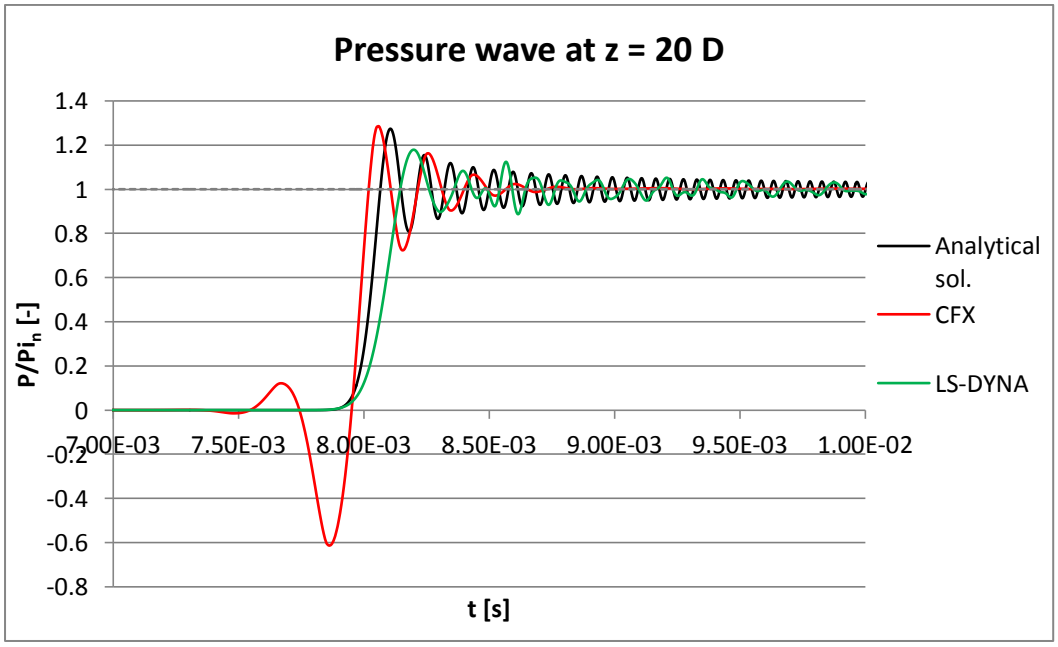

Figure 4.12 - Normalized fluid pressure at the cylinder axis (z = 20D): comparison between analytic solution, CFX and LS-DYNA simulations.

4.5 Structural Mechanics solver evaluation

4.5.1 Structure domain and mesh

A cylindrical beam of a linear elastic material and with theoretical infinite length has been assumed. In order to render this last condition, the longitudinal length is set 100 times the diameter (Figure 4.13). The beam, originally at rest, is constrained at outlet and the simulation stops before the wave front reaches the end of the domain, preventing reflections. Again, a coarse mesh (Figure 4.14) and a finer mesh (Figure 4.15) have been simulated.

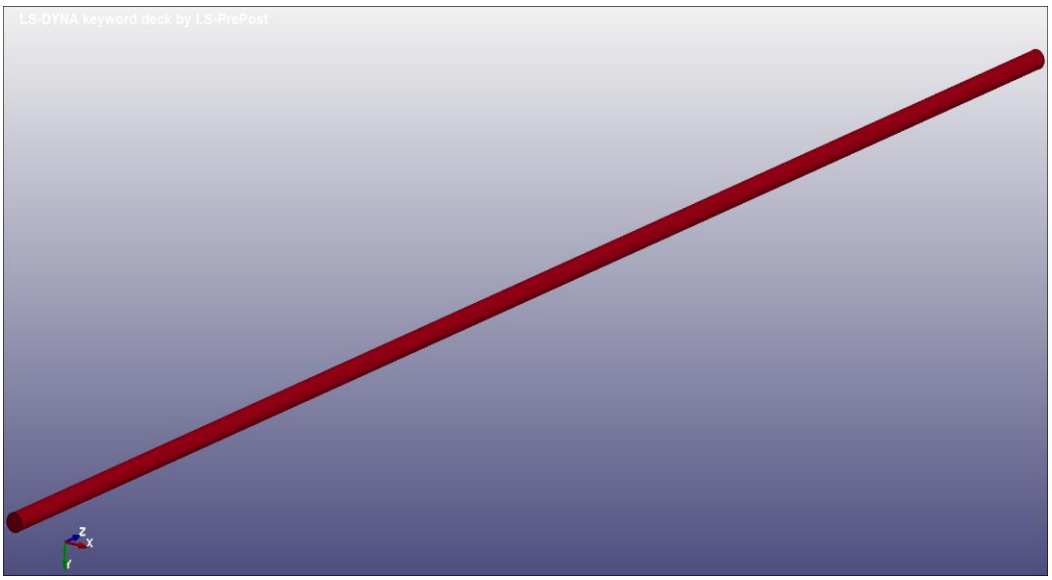

Figure 4.13 - Solid domain.

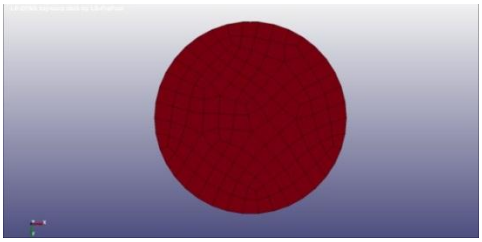

Figure 4.14 - LS-DYNA coarser solid mesh.

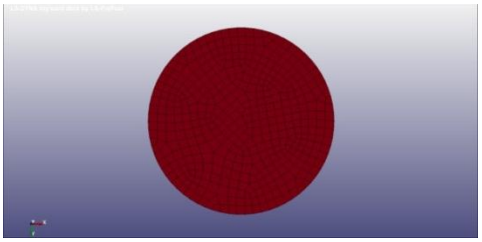

Figure 4.15 - LS-DYNA finer solid mesh.

4.5.2 Geometry and material properties

Geometry and material properties of the domain are listed in Table 4.8.

Quantity	Symbol	Value	Unit
Length	L	2000	μm
Radius	R	10	μm
Diameter	D	20	μm
Density	ρ	2300	kg/m^3
Young's modulus	E	1.05E+10	Pa
Poisson's ratio	ν	0.3	-

Table 4.8 - Geometry of the simulated domain and material properties.

4.5.3 Mesh

In Table 4.9 are reported the main features of the two types of discretization of the domain.

	Mesh 1	Mesh 2
Nr. of nodes	190284	1081550
Nr. of elements	165907	1000821
Max characteristic length	1.65 μm	0.9 μm
Element type	Hexahedron	Hexahedron
Nr. of elements on diameter	13	23
Nr. of elements on axial length	1211	2229

Table 4.9 - Features of the two simulated meshes.

4.5.4 Loads and boundary conditions

In Table 4.10 are listed the pressure load at inlet (Figure 4.16) and the solid constraints.

Location	Boundary condition/load	Features
Inlet	Shock wave of magnitude 1.4E+06 Pa	See Figure 4.16
Outlet	Fixed nodes	3 translational constraint 3 rotational constraint

Table 4.10 - Applied load and boundary condition.

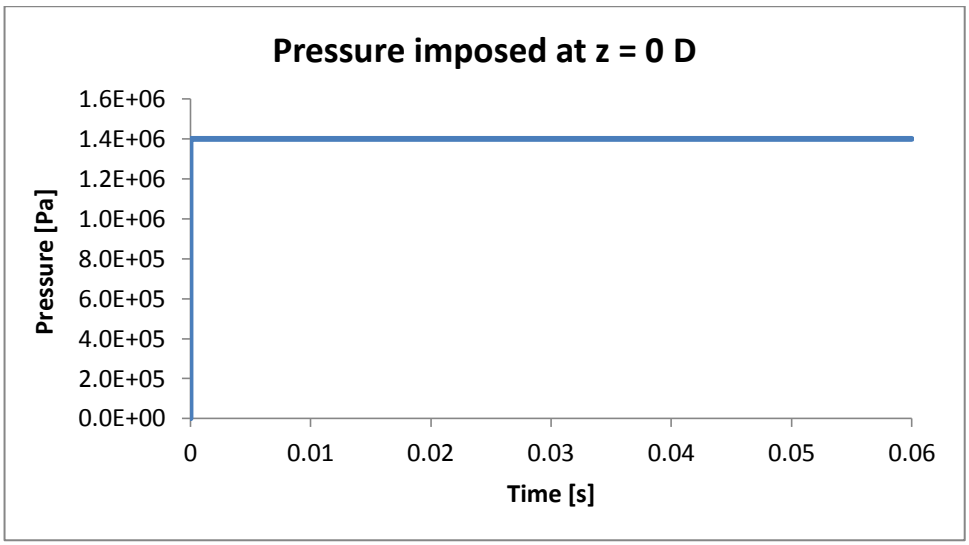

Figure 4.16 - Pressure load applied at inlet.

4.5.5 Simulation settings

Table 4.11 are resumed the numerical methods and the time discretization used for this simulation.

End time	1.5E-06 s
Time step	Mesh 1: 3.18E-11 s Mesh 2: 1.68E-11 s
Integration method (time)	Central difference 2nd order accurate scheme
Element formulation	Fully integrated S/R solid

Table 4.11 - Main settings of the simulations.

4.5.6 Computational aspects

With Table 4.12 are reported the computational costs related to the core number and mesh size.

	Mesh 1	**Mesh 2**
Execution	Distributed memory parallel (MPP)	Distributed memory parallel (MPP)
Core number	4	4
Precision	Double	Double
Simulation time	14156 s = 3.9 h	25981 s = 7.2 h
Mesh size	~2x10^5 elements	~1x10^6 elements

Table 4.12 - Main characteristics of the simulation process.

4.5.7 Results

The figures of the main results are shown below. In Figure 4.17 and Figure 4.18 the images of the strain and stress waves effects on the bar at time 4.6E-07 seconds are represented and it can be easily seen how the wave front propagates along the bar.
From Figure 4.19 it can be stated that there is agreement between numerical and analytical results from the point of view of the wave front speed, the value of the imposed pressure at inlet, and the lowest frequency oscillations, but behind the front it can be seen that high frequencies are not exactly evaluated by the software. This probably because of the presence of the constraint, which in the exact solution is at infinite distance from the pressure application point and for modeling reasons in the numerical model is obviously not, or because of a software highest frequencies automatic cutoff.
Finally it can be stated that mesh 2, which is finer than mesh 1, can better catch the evolution of the high frequencies stress oscillations than mesh 1.

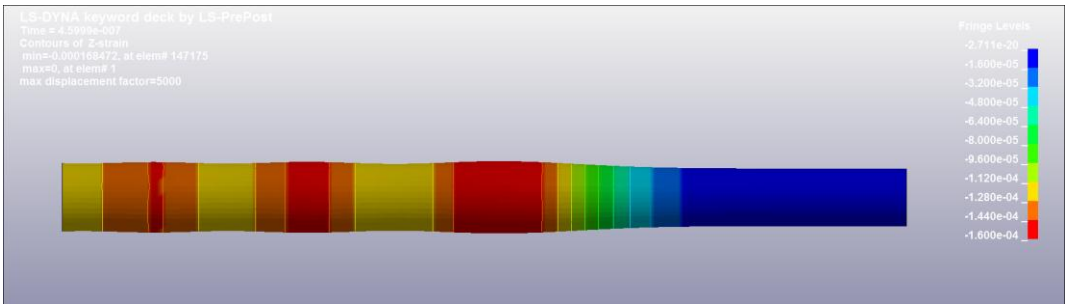

Figure 4.17 - Longitudinal strain.

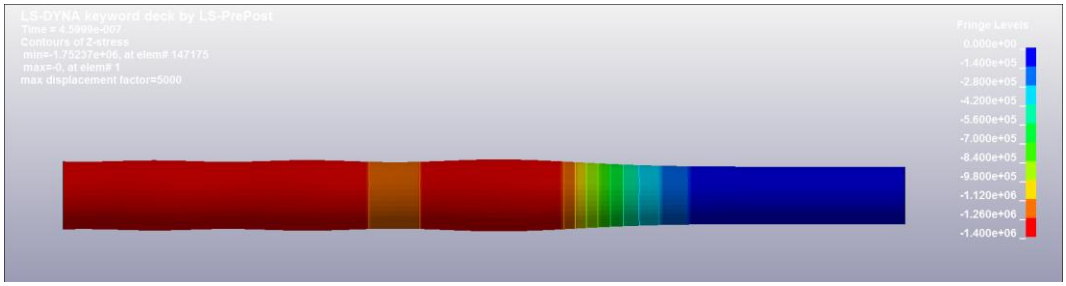

Figure 4.18 - Longitudinal stress.

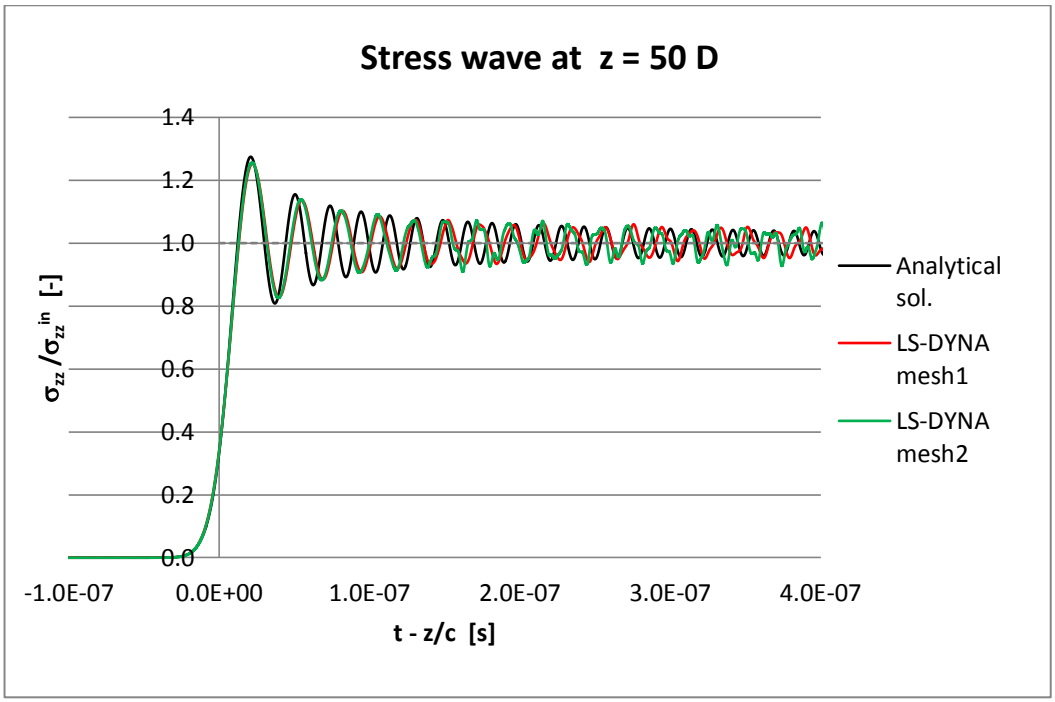

Figure 4.19 - Normalized longitudinal stress at the beam axis (z = 50D): comparison between analytic solution, LS-DYNA simulation and ANSYS simulation.

4.5.8 ANSYS Mechanical simulation description

The same problem has been analyzed with ANSYS Explicit Dynamics. The simulation settings are close to LS-DYNA ones, in order to obtain comparable results. So, the geometry of the domain, the material properties, the load and the boundary conditions are identical. Some differences arise in the characteristics of the mesh and in the simulation process. For more details, refer to Figure 4.20, Table 4.13, Table 4.14 and Table 4.15.

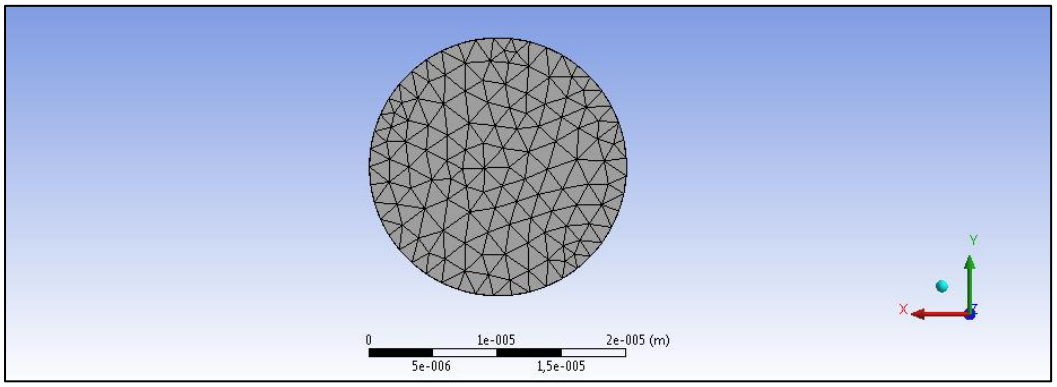

Figure 4.20 - View of XY-plane.

Nr. of nodes	185590
Nr. of elements	882065
Max characteristic length	1.65 µm
Element type	Tetrahedrons
Nr. of elements on diameter	18
Nr. of elements on axial length	3465

Table 4.13 - Features of the mesh simulated in ANSYS.

End time	1.1E-06 s
Time step	1E-10 s
Integration method (time)	Central difference 2nd order accurate scheme
Element formulation	Average Nodal Pressure Tetrahedral Element

Table 4.14 - Main settings of ANSYS simulation.

Execution	Serial
Core number	8
Precision	Double
Simulation time	5,6 h
Mesh size	~$9x10^5$ elements

Table 4.15 - Main characteristics of ANSYS simulation process.

4.5.9 *Comparison between LS-DYNA, ANSYS Mechanical and exact analytical solution*

Both software seem to accurately calculate the wave front speed and the imposed pressure at z=0, as we can see from . Therefore also ANSYS Explicit Dynamics presents the same problems than LS-DYNA, in fact the back of the perturbation seems to be correctly caught only in the low frequencies. This because of automatic software high frequencies cutoff or the impossibility of representing the model of an infinite solid bar.
However, for what concerns the main purposes and aims of our study, these results seem to be quite reliable for both the software, which have also comparable calculation times for the same problem.

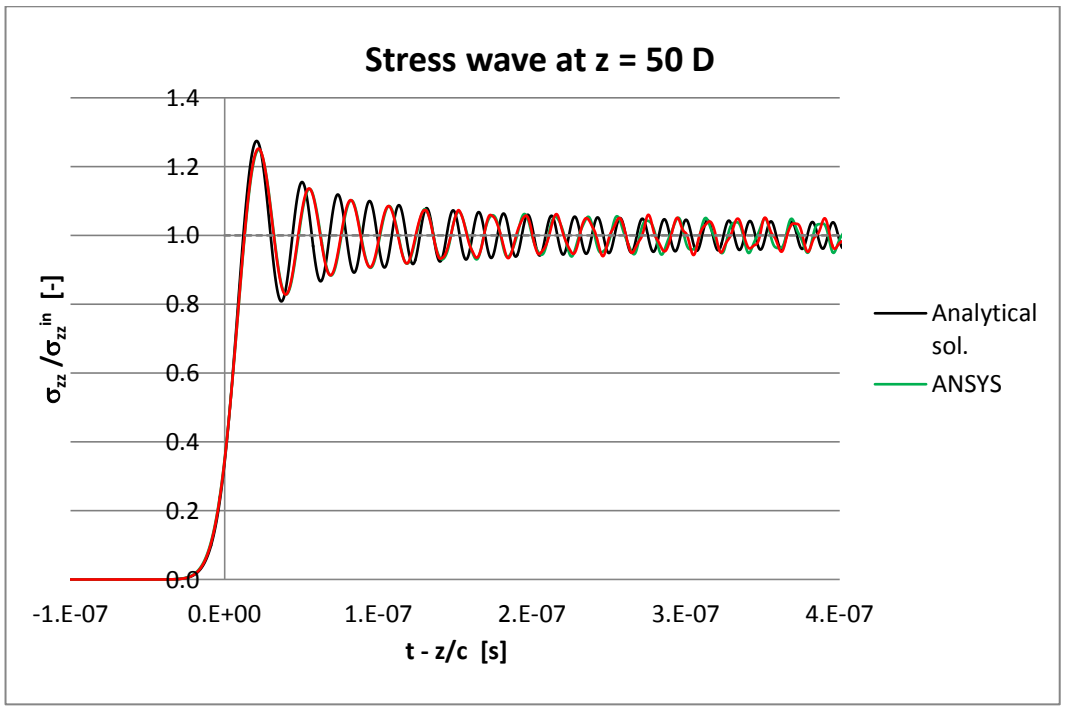

Figure 4.21 - Normalized longitudinal stress at the beam axis (z = 50D): comparison between analytical solution, LS-DYNA simulation and ANSYS simulation.

In Figure 4.22 the wave forms are plotted with respect to time for two gauge points, fifty and eighty diameters of distance from the inlet section. It is clear that both LS-DYNA and ANSYS catch the right wave speed evaluated with expression $c = \sqrt{E/\rho} =$ 2136 m/s with a negligible error.

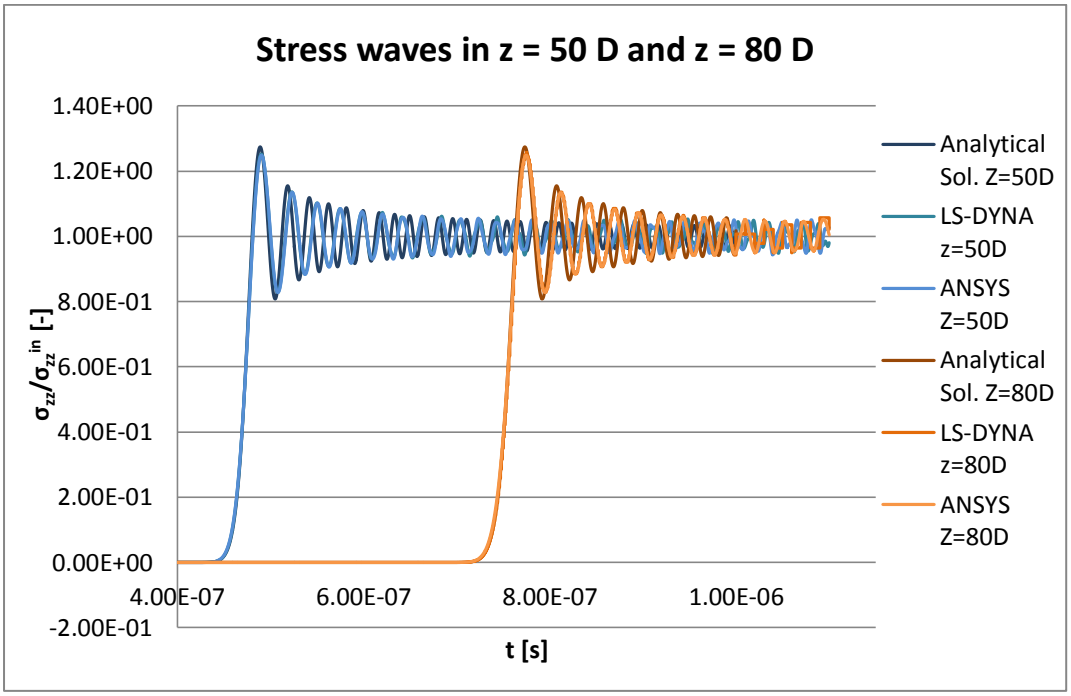

Figure 4.22 - Normalized longitudinal stress at the beam axis (z = 50D, z =80D): comparison between analytical solution, LS-DYNA simulation and ANSYS simulation.

4.6 Fluid – Structure Interaction solver evaluation

4.6.1 Domain and mesh

The problem consists in an infinitely long tube filled with fluid (Figure 4.23), which has a step pressure wave moving in the positive axial direction as initial condition. Initially the fluid velocity is null and the pressure is equal to the reference pressure. The inlet edge of the pipe is fixed. The domain axial length is assumed to be 100 times the diameter of the tube to simulate the infinite length condition. Since the problem is axially symmetrical, the domain is reduced to one quarter and the appropriate symmetry conditions are imposed.
To simulate a fluid-structure interaction, LS-DYNA needs an ALE mesh that contains the Lagrangian mesh. The ALE mesh, so, could be divided in two parts: the first one describes the water that is constrained by the Lagrangian structure (that is "immersed" in the fluid mesh) and the second one includes the surrounding elements, characterized by a very low density material. The two meshes do not share nodes. Figure 4.24, Figure 4.25 and Figure 4.26 show the three different simulated meshes. In particular, it can be identified the internal fluid (red), the external fluid (blue) and the thin pipe (the white marks indicate the nodes of the Lagrangian mesh).

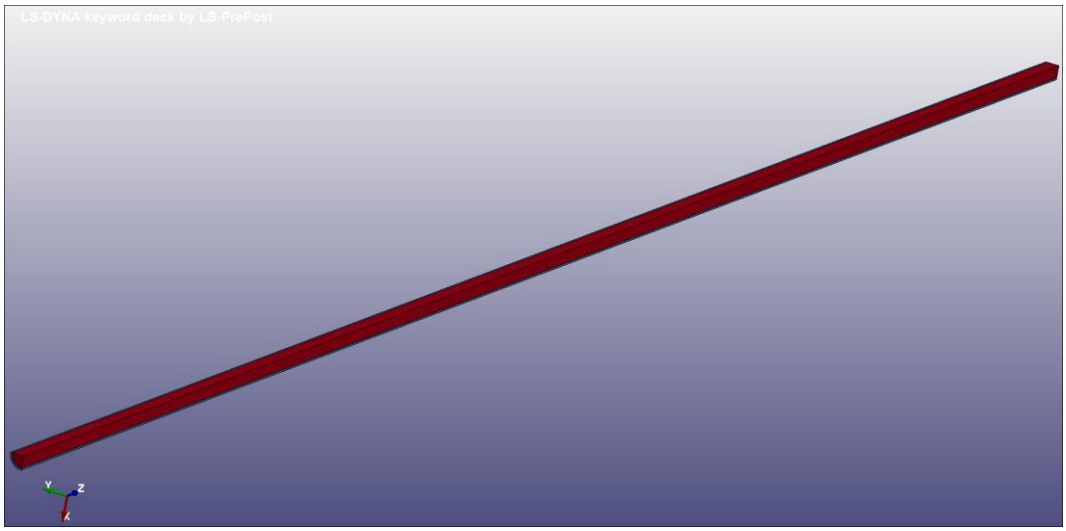

Figure 4.23 - Model domain.

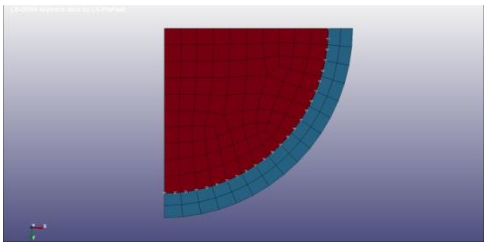

Figure 4.24 - View of XY-plane, mesh 1.

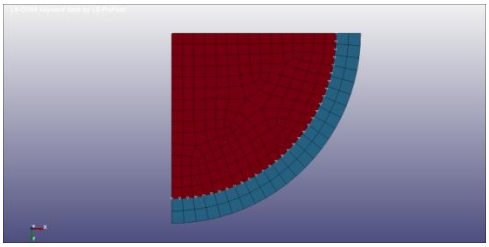

Figure 4.25 - View of XY-plane, mesh 2.

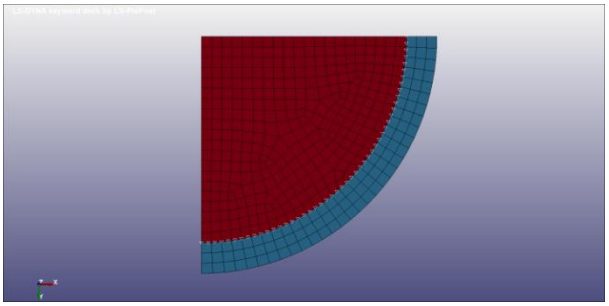

Figure 4.26 - View of XY-plane, mesh 3.

4.6.2 Geometry and materials properties

The geometry of the problem and the properties of fluid and solid materials are listed in Table 4.16.
The internal fluid (water) is compressible and inviscid, the solid structure is composed of a linear elastic material and the external fluid is a low density, incompressible fluid.

Quantity	Symbol	Internal fluid	Solid structure	External fluid	Unit
Length	L	60	60	60	m
Radius	R	0.3048	-	-	m
Diameter	D	0.6096	-	-	m
Thickness	h	-	0.004857	0.0452	m
Density	ρ	999.8	59156	0.0012	kg/m^3
Dynamic viscosity	μ	0	-	0	kg/(m·s)
Equation of state	EOS	Gruneisen[1]	-	-	-
Reference pressure	P_{ref}	1.00E+05	-	1.00E+05	Pa
Young's modulus	E	-	2.07E+14	-	Pa
Poisson's ratio	ν	-	0.3	-	-

Table 4.16 - Geometry of the simulated domains and materials properties.

[1] The parameters used in the Gruneisen EOS for internal fluid are the same of the fluid simulations in Table 4.1 - Geometry of the simulated domain and material properties.

4.6.3 Mesh

For each simulation, Table 4.17 describes the main features of the three types of discretization of the domain.

		Mesh 1	**Mesh 2**	**Mesh 3**
Total domain	*Nr. of total nodes*	363169	936301	2166517
	Nr. of total elements	318000	842000	2000000
Internal fluid	*Nr. of nodes*	220110	654218	1476369
	Nr. of elements	182000	570000	1328000
	Element type	Brick (Hexahedron)	Brick (Hexahedron)	Brick (Hexahedron)
	Max characteristic length	0.03 m	0.02 m	0.015 m
	Nr. of elem. on diameter	10	15	20
	Nr. of elem. on axial length	2000	3000	4000
Solid structure	*Nr. of nodes*	75025	132033	294049
	Nr. of elements	72000	128000	288000
	Element type	Shell (Quadrilateral)	Shell (Quadrilateral)	Shell (Quadrilateral)
	Max characteristic length	0.02 m	0.015 m	0.01 m
	Nr. of elem. on thickness	1	1	1
	Nr. of elem. on axial length	3000	4000	6000
External fluid	*Nr. of nodes*	102051	225075	528132
	Nr. of elements	64000	144000	384000
	Element type	Brick (Hexahedron)	Brick (Hexahedron)	Brick (Hexahedron)
	Max characteristic length	0.03 m	0.02 m	0.015 m
	Nr. of elem. on thickness	2	2	3
	Nr. of elem. on axial length	2000	3000	4000

Table 4.17 - Features of the three simulated meshes.

4.6.4 Loads and boundary conditions

Table 4.18 describes the pressure load due to the shock wave and the boundary conditions applied both to fluid domain and solid structure.

Location	Boundary condition	Features
Inlet of internal fluid	Shock wave of magnitude 1E+05 Pa	See Figure 4.10
Outlet of internal fluid	Non-reflecting boundary condition	Acts on dilatational and shear waves
Inlet of solid structure	Fixed nodes	3 translational constraint 3 rotational constraint
XZ plane	Symmetry	1 translational constraint (y-direction) 3 rotational constraint
YZ plane	Symmetry	1 translational constraint (x-direction) 3 rotational constraint
Symmetry axis	Symmetry	2 translational constraint (x and y dir.) 3 rotational constraint

Table 4.18 - Applied loads and boundary conditions.

4.6.5 Simulation settings

In Table 4.19 are listed the numerical methods used for fluid and structure and the time discretization.

End time	0.065 s
Time step	Mesh 1: 8.67E-06 s Mesh 2: 6.18E-06 s Mesh 3: 4.44E-06 s
Integration method (time)	Central difference 2nd order accurate scheme
Advection method (space)	Van Leer, 2nd order accurate method
Fluid element formulation	ALE multi-material element
Solid element formulation	Fully integrated S/R solid
FSI coupling method	Penalty coupling

Table 4.19 - Main settings of the simulations.

4.6.6 *Computational aspects*

In Table 4.20 are reported the computational costs related to the core number and mesh size used.

	Mesh 1	**Mesh 2**	**Mesh 3**
Execution	MPP	MPP	MPP
Core number	16	16	16
Precision	Double	Double	Double
Simulation time	2874 s = 0.8 h	8790 s = 2.44 h	31455 s = 8.74 h
Mesh size	~$3x10^5$ elements	~$8x10^5$ elements	~$2x10^6$ elements

Table 4.20 - Main characteristics of the simulation process.

4.6.7 *Results*

In Figure 4.27 and in Figure 4.28 it is shown the instantaneous pressure distribution along the solid tube after 0.02 seconds of simulation generated respectively by the water hammer wave on the contact surface and the precursor wave in the pipe. The latter is the consequence of the propagation of a stress wave in the solid with higher speed than in the fluid domain. For this reason the two images are not referred to the same space interval of the tube, because the precursor wave was, at the same instant of time, much father from the inlet than the water hammer wave.
As might be expected from the results of Skalak, the precursor wave has smaller amplitude than the water hammer wave, but it has still to be considered in tube design because it creates a condition of pre-stress in the fluid-structure system.
The water hammer wave generates a compression wave on the surface of the tube which tends to expand giving the values shown in Figure 4.27.

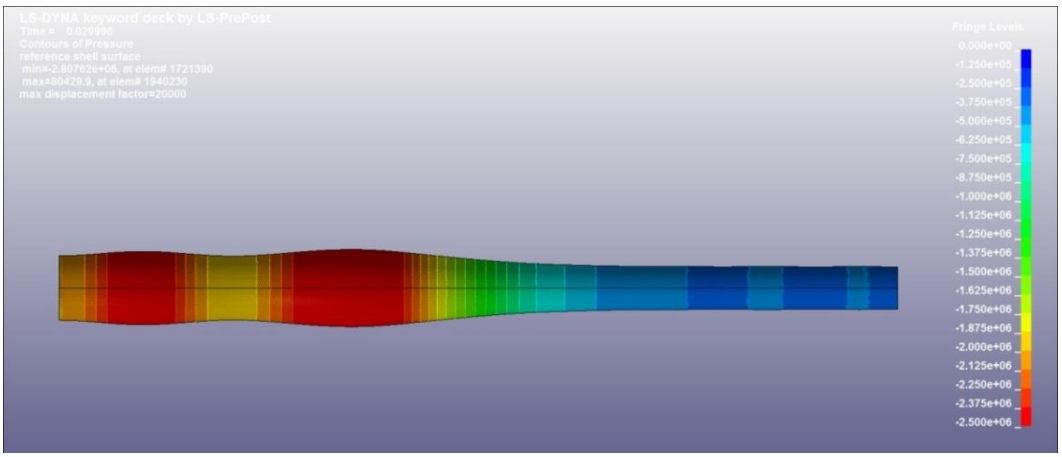

Figure 4.27 - Tube pressure due to water hammer wave.

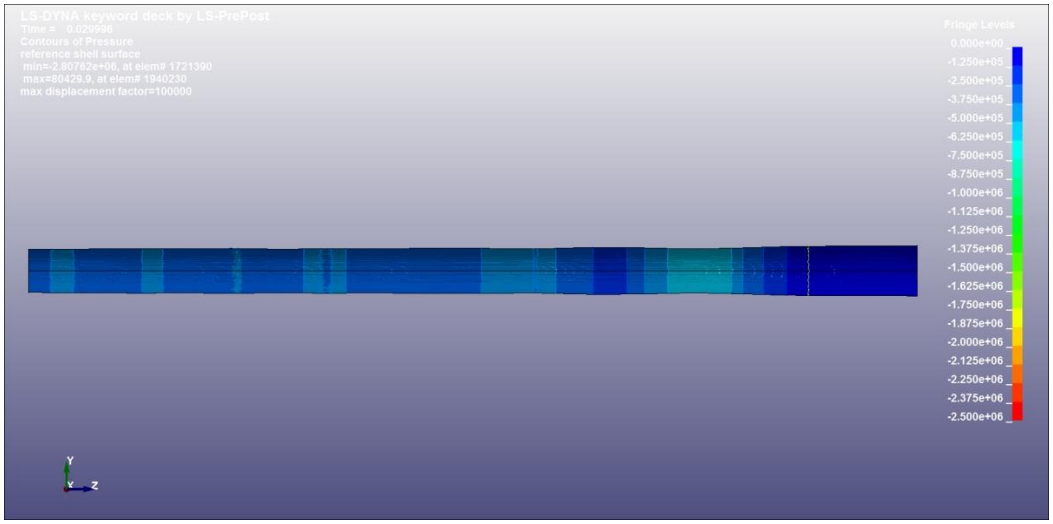

Figure 4.28 - Tube pressure due to precursor wave.

In the next charts it can be seen the comparison between the exact analytical solution of Skalak and Tijsseling and the results obtained with the LS-DYNA software.
Figure 4.29 shows the varying of the pressure values in a specified gauge point situated twenty diameters after the inlet section. Here are presented the results obtained with the previously presented three meshes, from the coarser to the finer. It can be clearly seen that the finer is the mesh the better is the according with the exact solution values of pressure.
The instants before the arriving of the wave front are characterized by high frequency oscillations near the zero value. That's because many software, and also LS-DYNA, encounter difficulties in simulating shock waves propagation, especially in the portion of time and space jest before the wave front. LS-DYNA uses numerical damping systems to minimize this problem and reduce these spurious oscillations, but we decided, in order to correctly analyze how the solver works, to keep the solution free from this type of damping.

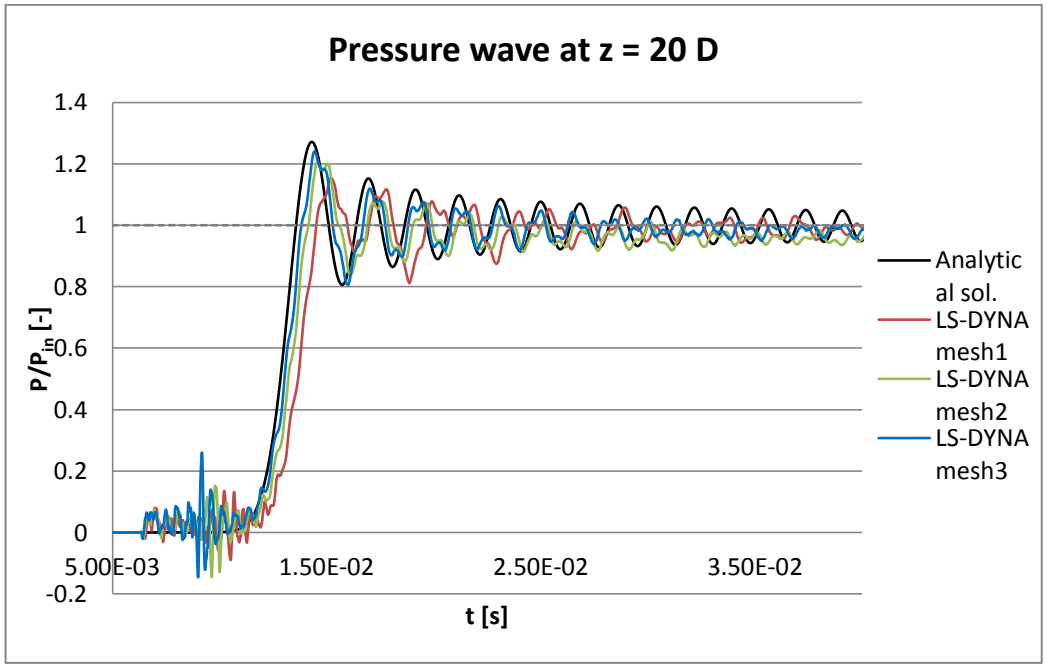

Figure 4.29 - Normalized fluid pressure at the beam axis (z = 20D): comparison between analytic solution and LS-DYNA simulations with different meshes.

In Figure 4.30 are plotted the results given by LD-DYNA in two specified gauge points, twenty and forty diameters from the inlet section, in the passing of time, both compared with the analytical solution adopted. During the propagation of the shock wave in the domain it can be seen from this chart that the wave speed evaluated numerically is a little smaller than the one evaluated with the exact theory. In fact the wave speed value obtained with the classic expression is 972,38 m/s, while the one evaluated through the numerical result is 955,89 m/s, but the difference is in the order of 2%, and in our analysis is an acceptable value.

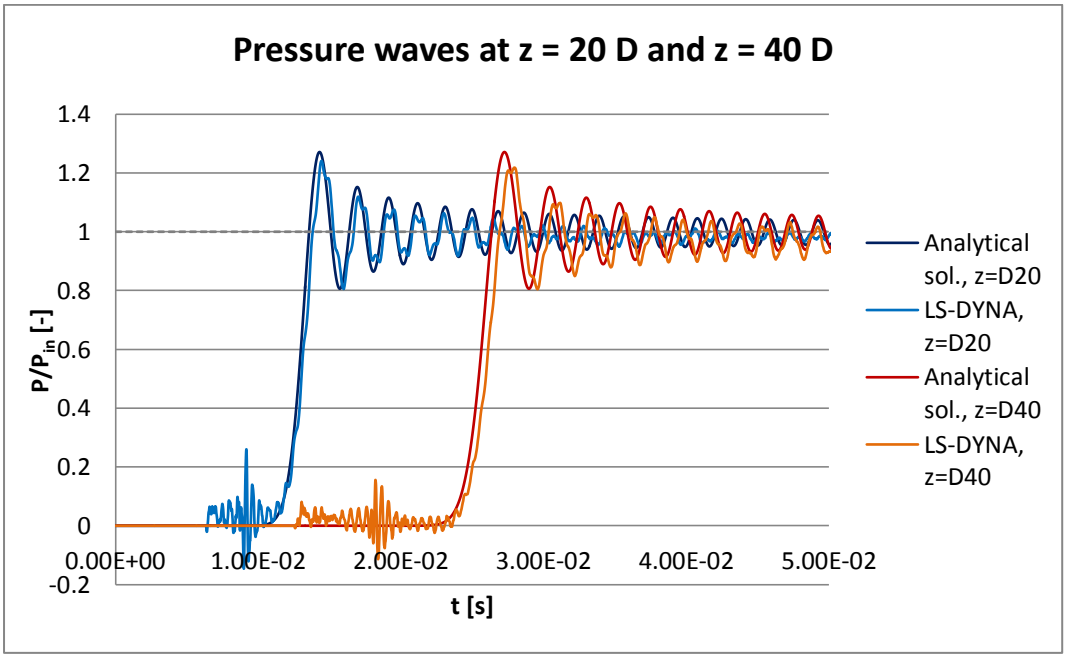

Figure 4.30 - Normalized fluid pressure at the beam axis (z = 20D and z=40D): comparison between analytic solution and LS-DYNA simulation with the finest mesh.

4.6.8 ANSYS FSI Solution

As a final comparison it has been decided to numerically simulate the same FSI problem modeled with LS-DYNA. Posing the same physical domain and mesh, the same boundary conditions and the same duration and time interval properties, it has been observed that the ANSYS barely catch the correct wave form, with negative pressures excursions which are obviously incorrect for this kind of simulated case. But the main problem was the large simulation times expected by the ANSYS solver, which could have strongly compromised the expected times of the study. That's why it has been decided not to include those results into this work.

4.6.9 ANSYS and LSDYNA FSI comparison

Considering the previous observations it has been decided to adopt LSDYNA as solver for the present research study. Since for the solid part both the tested solvers had quite similar results with the exact analytical solution assumed, this conclusion is mainly based on the better precision emerged in the fluid simulations, and on the smaller simulation times obtained with LSDYNA compared to those resulted with the ANSYS FSI solver.

5 Fluid analysis

5.1 Overview of the problem

Since the phenomena objects of this study incorporate many different complex issues, such as the fluid structure interactions, the continuous change in shape and section of the fluid channels, or the incertitude in the evaluation of the parameters composing the problem, it has been chosen to analyze some of the single elements composing the whole complexity of the real domain.
With the aim of correctly understanding the consequences of the application of a compression wave on a section of a porous ground portion, it has been decided to isolate the case of the single fluid pore treated as fluid channel. In fact a portion of porous soil is composed by a solid structure and many channels filled by a mix of liquid and gaseous phases. For a preliminary analysis, as we can see from Figure 5.1, only the liquid phase has been taken into account, acting like observing a sample of the ground and extracting from this one the single fluid phase permeating the pores.

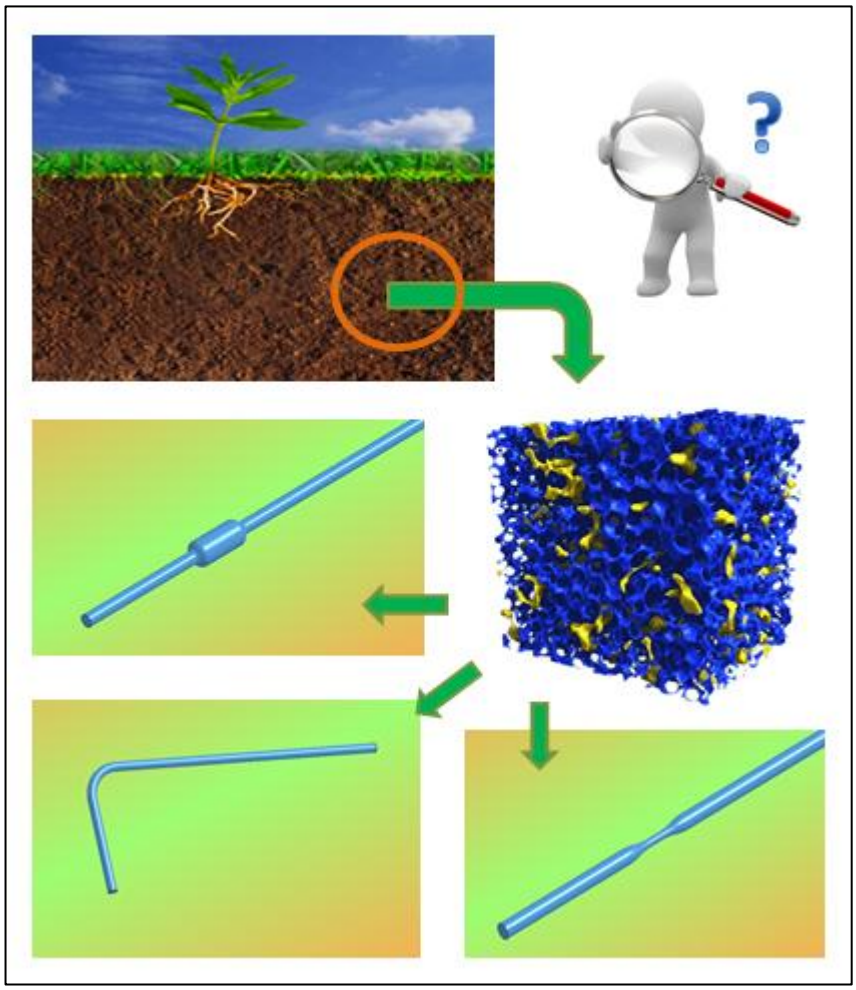

Figure 5.1 - From macro to micro-scale, identifying simple structures from soil whole complexity.

5.1 Overview of the problem

The pores that compose the fluid matrix may evolve into many forms, with different sections and directions, but how a single change of one of these parameters influences the acoustic impedance of a section of porous ground? To answer this question some singularities of the fluid domain are taken into consideration separately from the others.
Observing a single flow channel it can be seen that, for example, it may vary his section area with an enlargement, simulating the entering of the fluid in a bigger pore, or with a constriction reducing the space available to the fluid to flow. On the other hand the area may remain the same, but the channel longitudinal direction may vary for example with a curve or an elbow.
Since the context of this study is a portion of porous rock at high depth and high pressures, filled by oil with fixed properties, to simplify this problem only an atmospheric pressure has been assumed outside the elementary domains as reference pressure, but for further analysis the real pressure imposed by the overlying solid layers can be obtained simply varying this reference pressure parameter.
The considered oil, called in this work “standard oil”, has fixed features resumed in the following table (Table 5.1).

	Symbol	**Value**	**[#]**
Density	ρ	850	kg/m^3
Dynamic Viscosity	μ	0.05	Pa*s
Perturbation Speed	c	1172	m/s
Bulk Modulus	K	1.17	GPa

Table 5.1 - "Standard oil" parameters.

5.2 Fluid geometries

As mentioned before, some basic singularities in the fluid channels can be identified: enlargements of the sections, constrictions of the sections, and curves, represented by elbows, which changes the flow direction. So, those are the fluid geometries considered in this chapter. Furthermore a cylindrical straight domain has been considered to provide also a comparison between a fluid channel without singularities. Those geometries have been recreated and meshed with the meshing software *Gambit* developed by ANSYS Inc, which have provided better meshes than the software LS-Prepost, used only to set up the numerical simulations solved by LS-DYNA.

5.2.1 Straight tube geometry

A long straight cylindrical tube with z-axis as longitudinal direction has been considered (Figure 5.2), with a circular cross section and diameter *D* equal to 10μm, which is the estimated average diameter of a pore in a representative micro-porous medium taken as sample for those simulations. The chosen length *L* is 50D, to permit the solution not to be influenced in a commeasured region by the boundary conditions at the extremity of the tube.

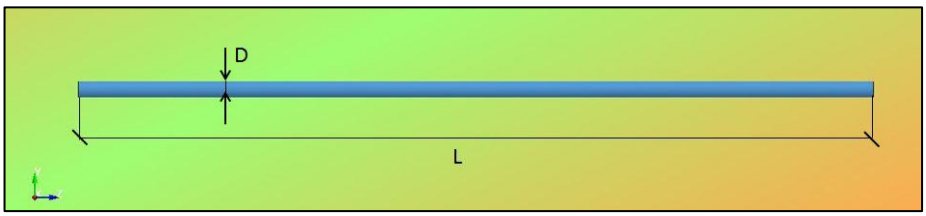

Figure 5.2 - Straight tube geometry.

5.2.2 Elbow geometry

With the aim of evaluating the acoustic impedance variations after a direction change, an elbow geometry has been modeled (Figure 5.3). The considered tube has a circular cross section with diameter D and elbow situated after 10D from the inflow surface, permitting the flow to develop completely. After the elbow, which is 5D long, a straight part of 30D length has been created to analyze the flow after its passing in this singularity.

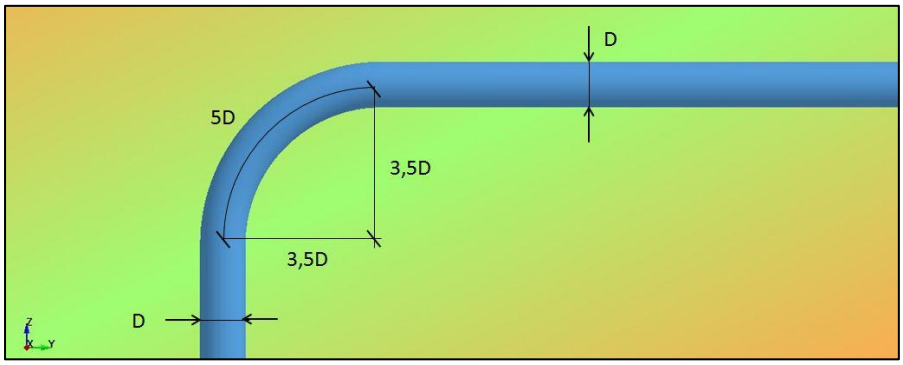

Figure 5.3 - Elbow geometry.

5.2.3 Enlargement geometries

To represent the developing of the flow and the consequent effects on the acoustic impedance after the passing in a larger pore, a cylindrical channel having circular cross section, but with an enlargement after 10D from the inflow surface, has been modeled.
Since many type of enlargements can be identified in pores nature, in this work it's been analyzed two prototypal cases: a sharper one and a smoother one.
As for the elbow geometry, both those enlargements have a length of 5D diameters, for a better results comparison.

5.2.3.1 Enlargement type 1

The sharpness of the first one (Figure 5.4) is meant in the fact that the passing from the channel diameter to the pore diameter occurs more rapidly than in the smoother, where diameter variation is slower. Precisely in this kind of geometry the pore diameter of 2D is reached after a distance of D/2 from the starting of the section change.

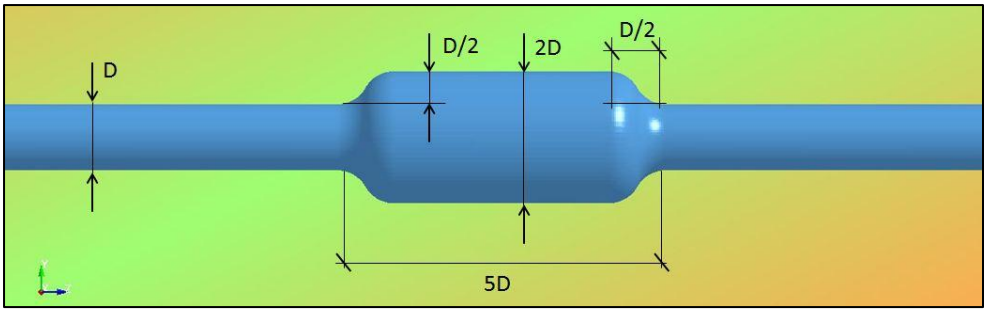

Figure 5.4 - Enlargement type 1 geometry.

5.2.3.2 Enlargement type 2

The smoother model (Figure 5.5) is smooth in the fact that it takes a 2D length to pass from the channel diameter to the pore diameter of 2D, and so the section change is softer.

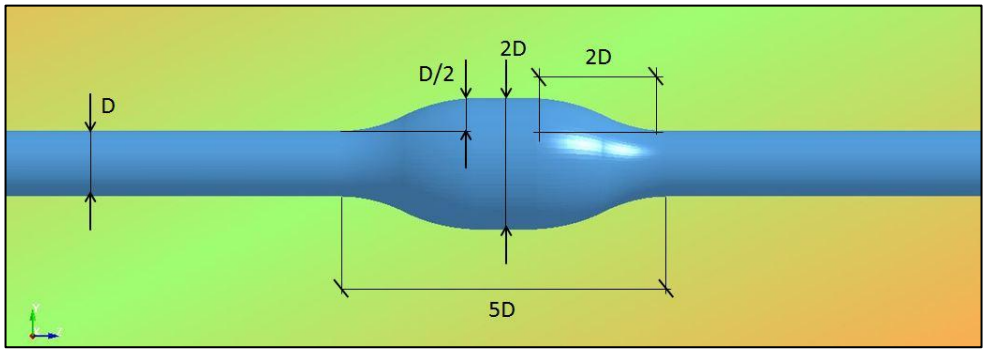

Figure 5.5 - Enlargement type 2 geometry.

5.2.4 Constriction geometry

The fluid flow in porous media may encounter obviously some kinds of section constrictions, that's why a constriction model has been developed (Figure 5.6). The channel diameter is D while the pore diameter is D/2 and the pore length is, as fixed for the previous singularities, 5D diameters. The form of the section change considered is the same used in the second type of enlargement, to provide results for a better comparison between the two opposite cases.

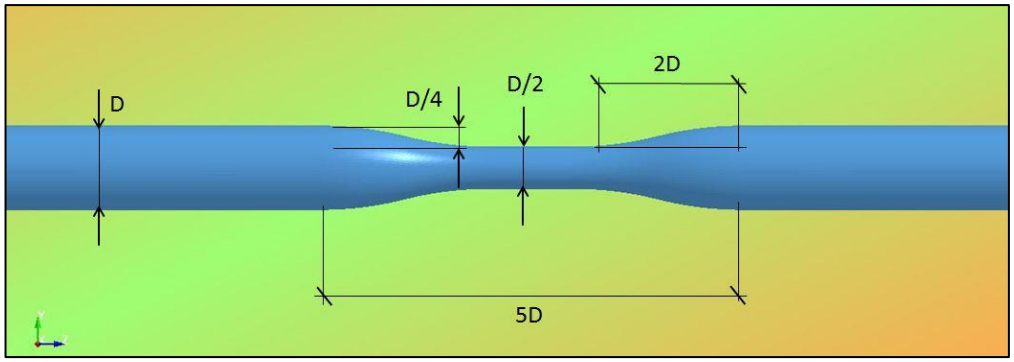

Figure 5.6 - Constriction geometry.

5.3 Boundary conditions

5.3.1 Constraints

To correctly represent the situation of a rigid tube with an interior fluid flux, a rigid wall has been modeled fixing the three translational and the three rotational degrees of freedom of the exterior nodes of every examined geometry.

5.3.2 Inflow and outflow conditions

In the inflow circular surface of each geometry a pressure condition has been set. As we can see from the results with a single compressional wave shown in paragraph 0, some small numerical errors are presents in the final part of the signal wave, that's why to prevent those type of errors it's been decided to introduce a multiple wavelet set as pressure condition in the inlet surface. The pressure signal is decided to be only compressional and characterized by an height of 140 Bar.
Since one of the aims of the present work is to analyze the variability of the acoustic impedance with a change in the input signal frequency, three frequencies have been simulated: 1e+06 Hz (Figure 5.7), 1e+07 Hz (Figure 5.8) and 1+08 Hz (Figure 5.9).

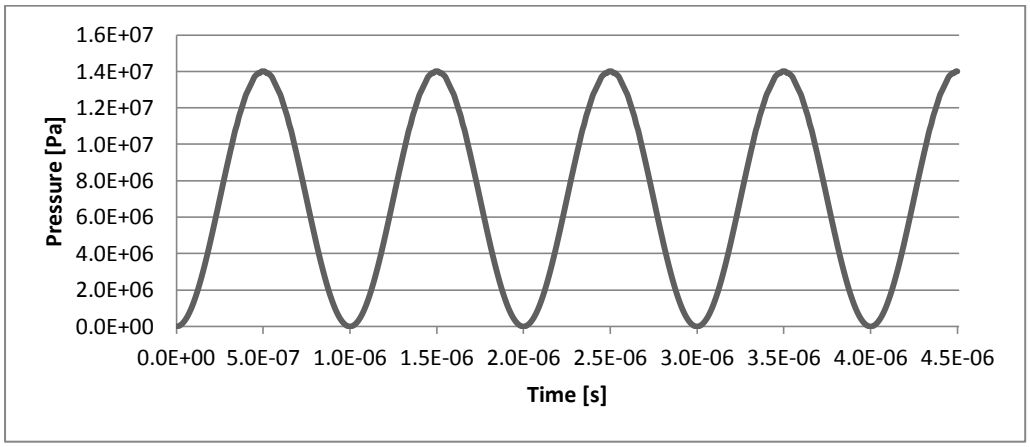

Figure 5.7 - 10^6 Hz input signal.

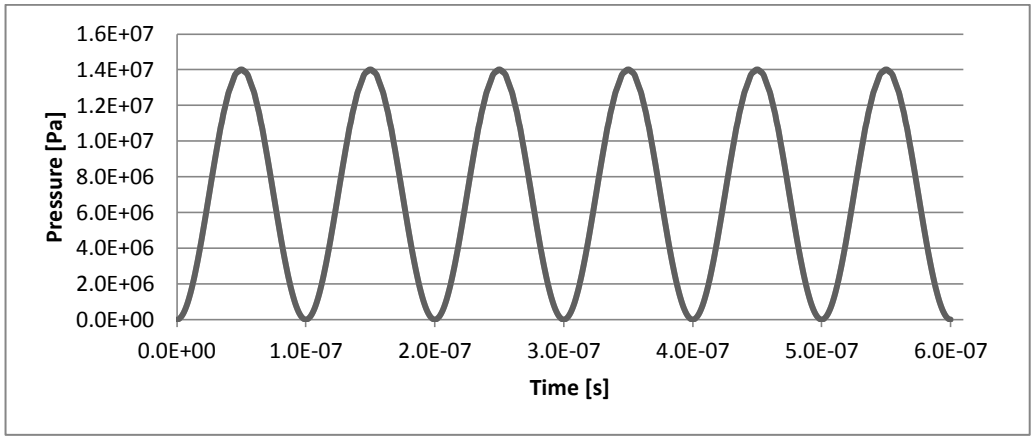

Figure 5.8 - 10^7 Hz input signal.

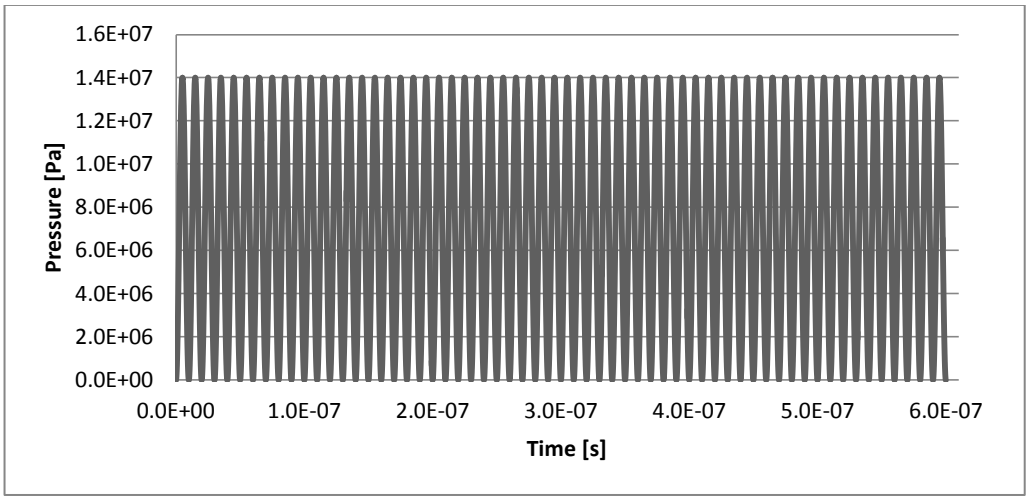

Figure 5.9 - 10^8 Hz input signal.

To simulate what happens in a portion of an infinite tube, or a tube with anechoical terminations, a non-reflective boundary condition has been posed to the outlet surface of the fluid channel, preventing reflection waves to influence the observed solution.

5.3.3 Initial conditions

At the time instant t=0 the system has been modeled completely at rest.

5.4 Mesh implementation

As said before, the discretization of the fluid domain geometries modeled has been implemented with the meshing software *Gambit*, typically used for CFD models.
With the purpose to correctly model the flow into those channels a volume mesh with hexahedral elements has been generated (Figure 5.10).

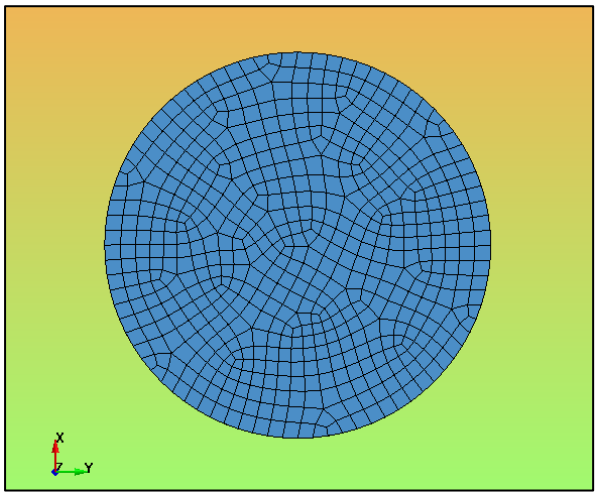

Figure 5.10 - Meshed tube section.

In the following table (Table 5.2) are resumed the main features of the mesh volumes used for this chapter calculations. Besides, every geometry has been meshed so as to obtain a number of nodes and elements on the radius of the circular surface to allow a fine simulation of the fluid velocity profile.

	Straight Tube	**Elbow**	**Large 1**	**Large 2**	**Thin 2**
Elements	743750	688415	782952	787194	807798
Nodes	795636	736488	836571	841100	863098

Table 5.2 - Meshes main characteristics.

5.5 Simulation times

In this paragraph are resumed the main time features of the simulations performed. The table below (Table 5.3) shows the integration time-step, the results saving time-step, the end time adopted for every frequency simulation, and the mean simulation length.

	1.00E+06	**1.00E+07**	**1.00E+08**
dt of integration	1.00E-11	1.00E-11	1.00E-12
dt of saving	1.00E-09	1.00E-09	1.00E-10
Sim. time	4.50E+06	6.00E-07	6.00E-07
Average sim. duration	10h	2h	4h

Table 5.3 - Simulation times.

5.6 Mesh validation

From the past studies on fluid simulations, the adopted volumes discretization is enough dense to ensure a correct solution of the examined problems. To prove this fact, a very thick discretization has been created increasing by the 50% the number of elements of a chosen domain, the elbow, with the aim of analyzing the differences between the used mesh and a high elements number mesh.

5.7 Results

After performed those numerical simulations, results of pressure and particle velocity signals have been detected in order to evaluate the acoustic impedance for many sections of interest.
The analysis has been developed observing the time variation of these values in those sections of interest, fixed for example in particular positions: before, within and after the singularity (Figure 5.11, Figure 5.12 and Figure 5.13) for every simulated geometry.

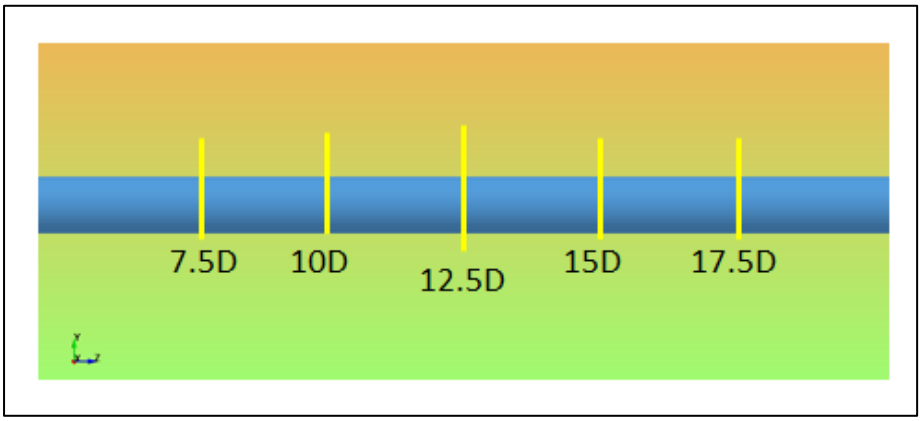

Figure 5.11 - Sections of observation in straight tube domain.

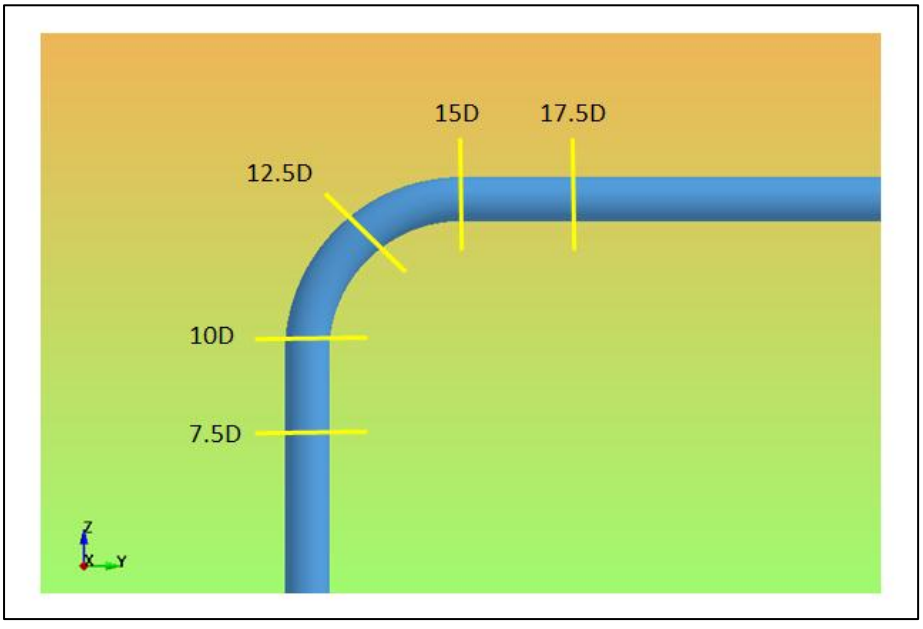

Figure 5.12 - Sections of observation in elbow geometry domain.

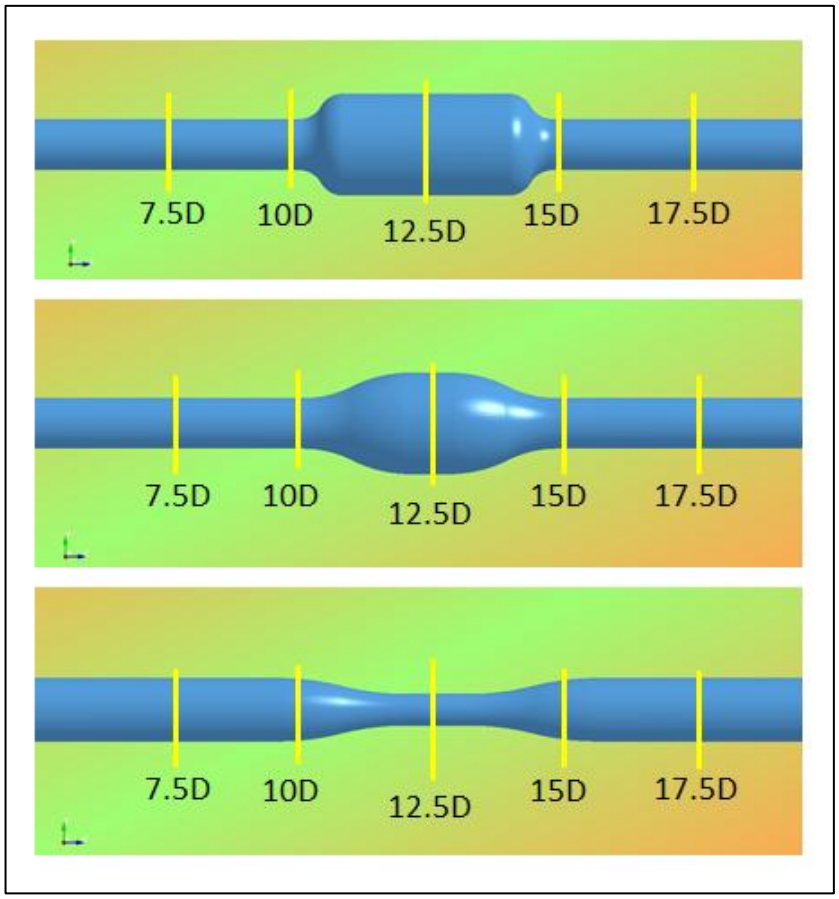

Figure 5.13 - Sections of observation in enlargements and constriction geometries domains.

5.7.1 Straight tube geometry

First of all pressure and velocity signals have been extracted for the straight tube geometry, to provide a comparison case for the solutions with the other tested geometries.
In the following figures (Figure 5.14, Figure 5.15, Figure 5.16, Figure 5.17, Figure 5.18, and Figure 5.19) are shown those results for every simulated frequency as a preliminary view of how the system reacts to a wave train chosen as input condition.

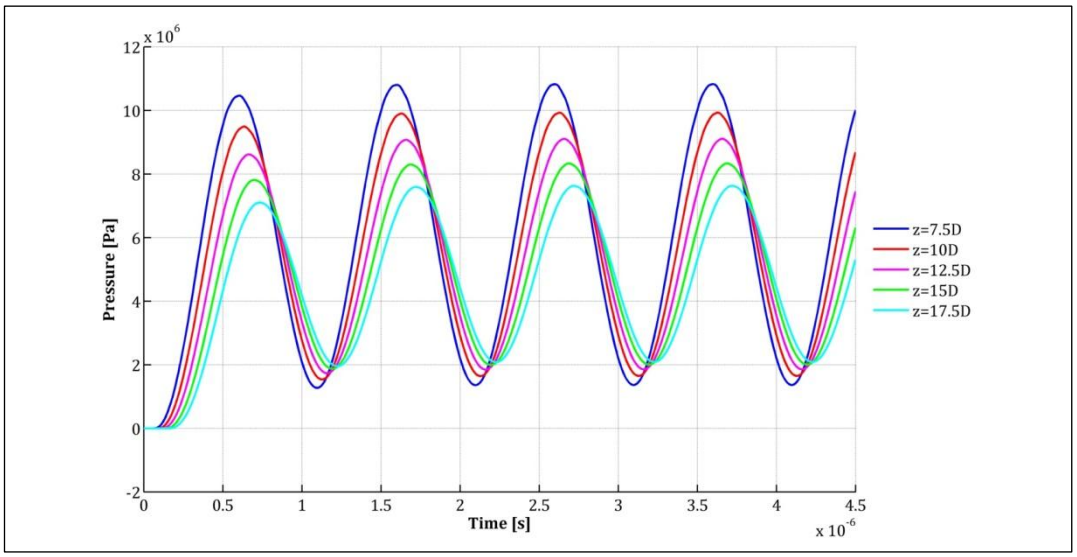

Figure 5.14 - Pressure signal for 10^6 Hz input frequency for straight tube geometry.

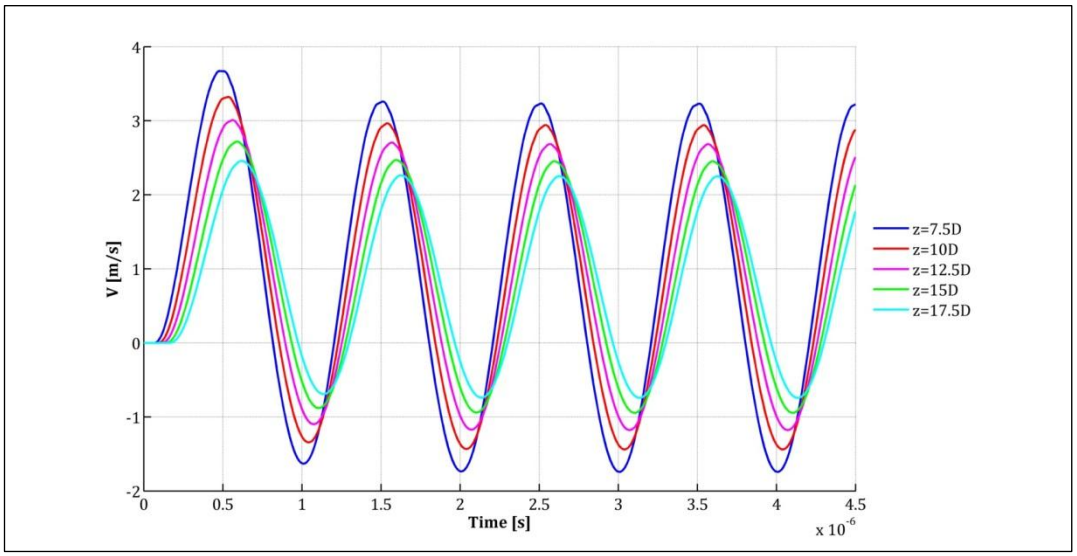

Figure 5.15 - Velocity signal for 10^6 Hz input frequency for straight tube geometry.

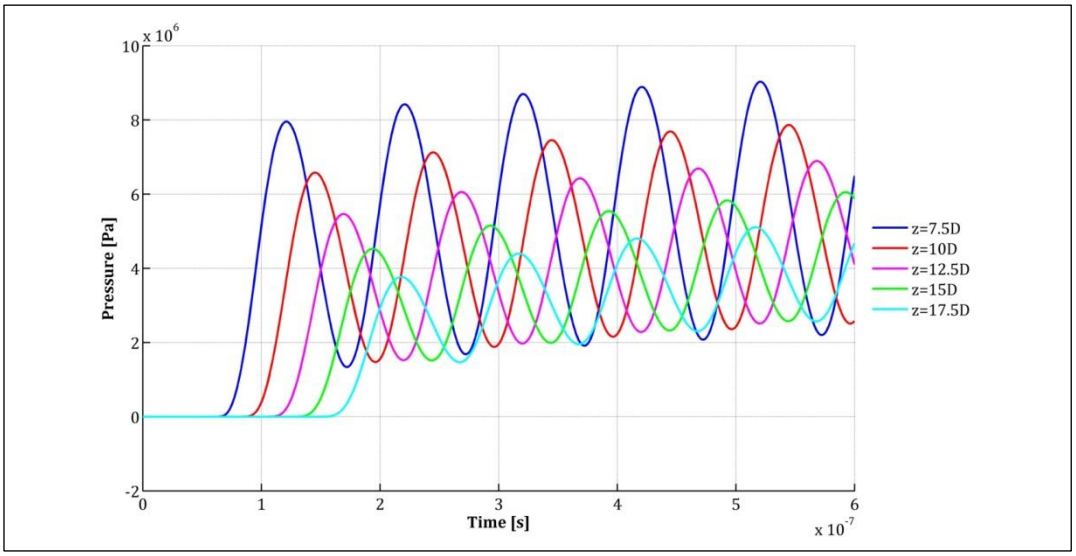

Figure 5.16 - Pressure signal for 10^7 Hz input frequency for straight tube geometry.

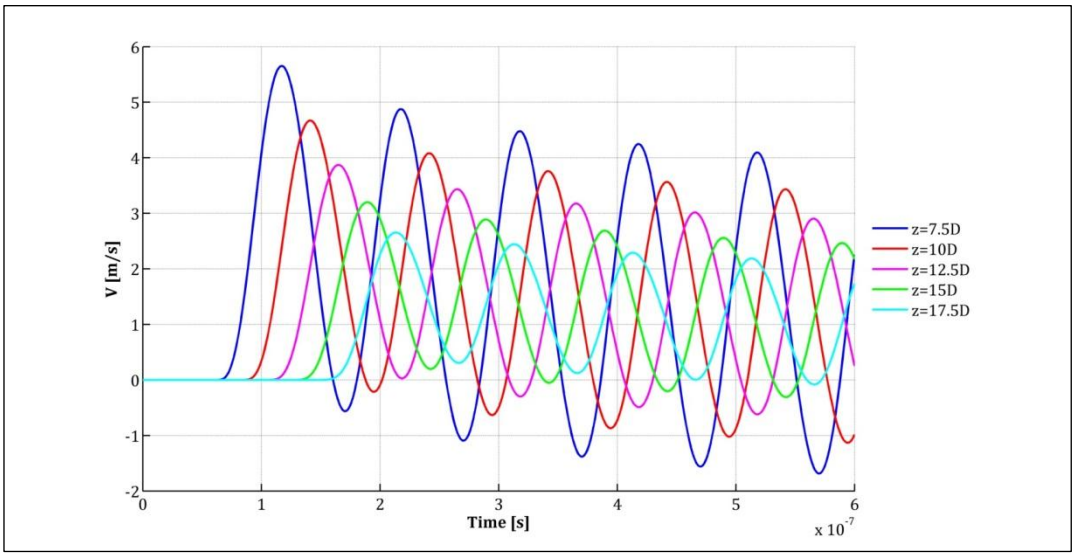

Figure 5.17 - Velocity signal for 10^7 Hz input frequency for straight tube geometry.

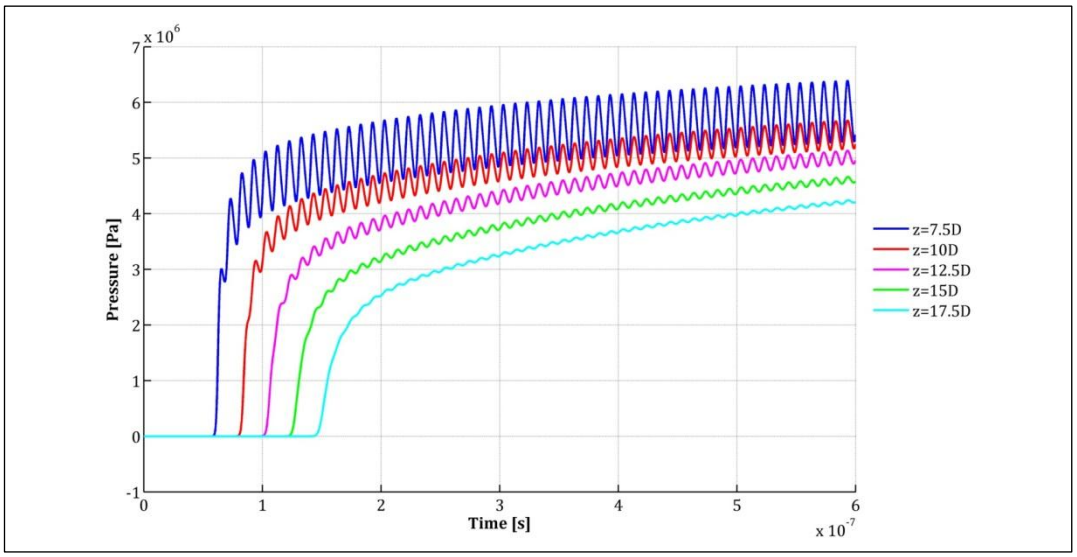

Figure 5.18 - Pressure signal for 10^8 Hz input frequency for straight tube geometry.

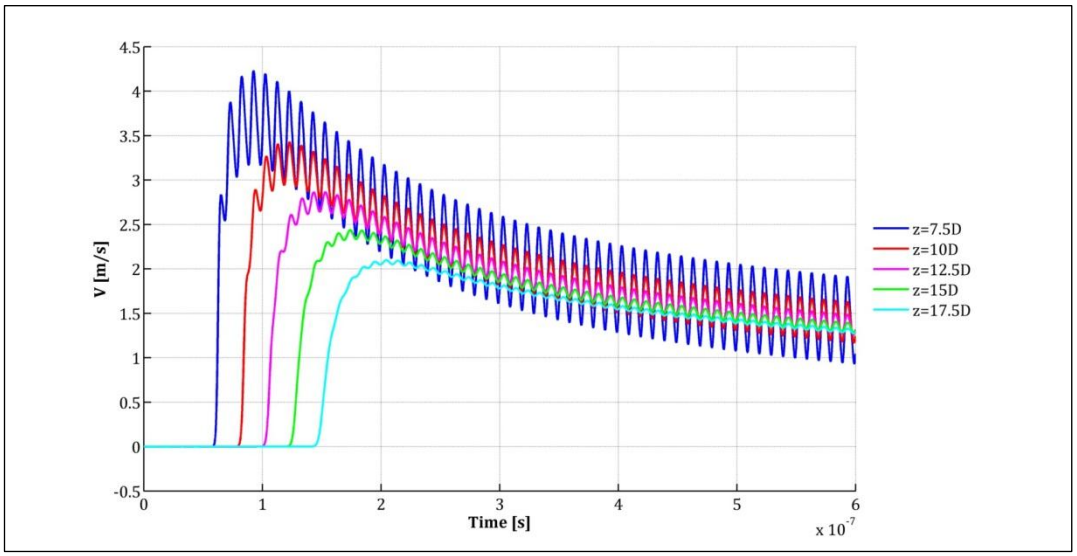

Figure 5.19 - Pressure signal for 10^8 Hz input frequency for straight tube geometry.

Pressure and velocity results can be also observed in the spatial domain, examining their variation along the tube at a fixed time instant (Figure 5.20 and Figure 5.21). Pressure seems to correctly be constant on surfaces perpendicular to the flow and its magnitude, represented by the colors resumed in the palette on the right, correctly oscillates decreasing the peak value by the increasing of the z-coordinate.

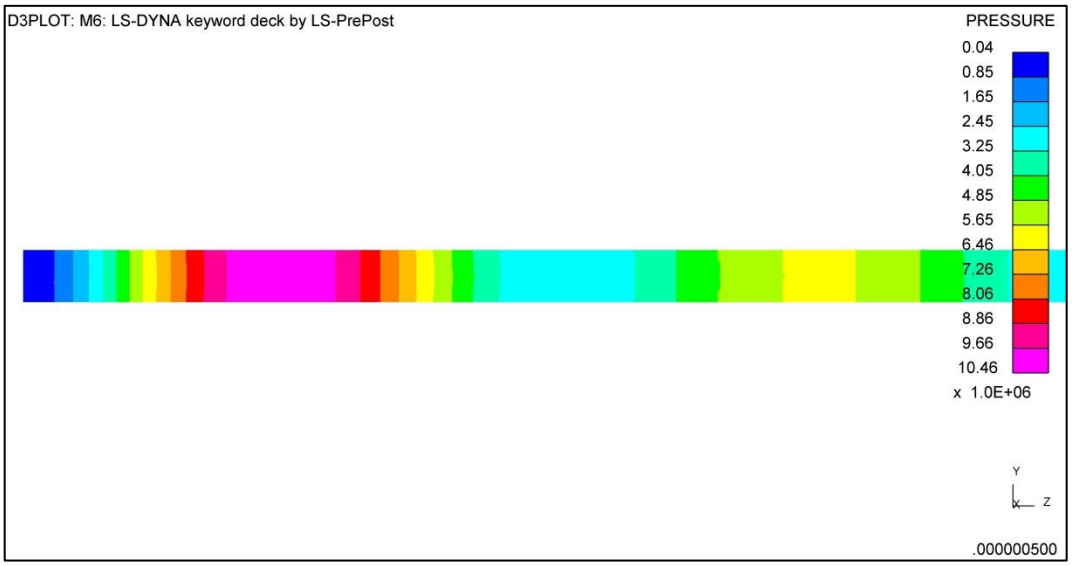

Figure 5.20 - Pressure evolution in the straight tube domain at $t=5\cdot10^{-7}$ s.

The same representation can be adopted for the velocity results where we can see the no slip condition on the walls is respected. Furthermore, as we can see from the velocity plots before, there are some regions where the velocity passes from positive to negative, change due to the sign of the pressure spatial variation which is negative in those parts of the domain.

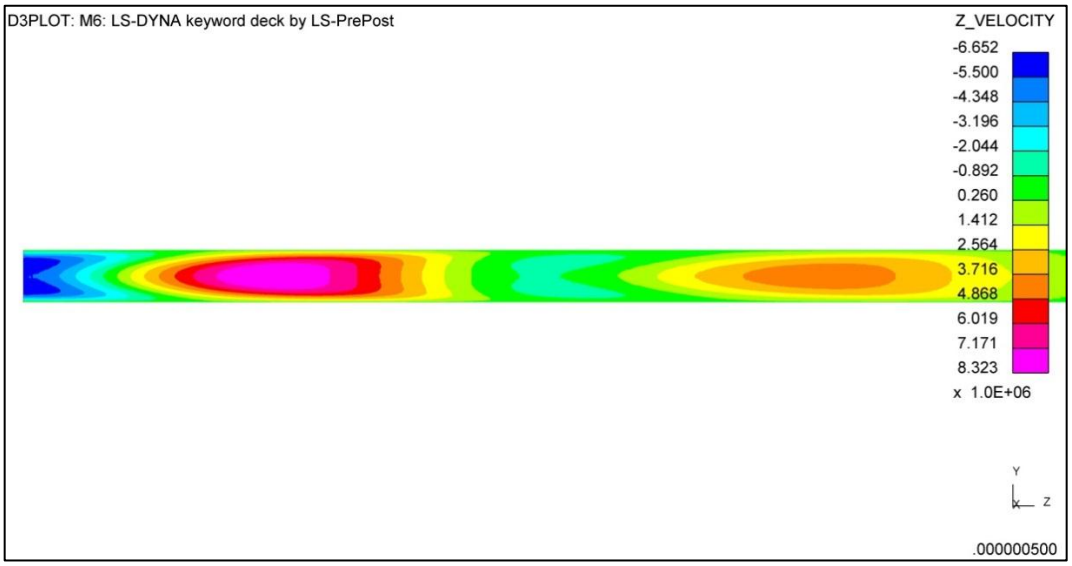

Figure 5.21 – Velocity evolution in the straight tube domain at $t=5\cdot10^{-7}$ s.

Looking at the velocity results and the fluid properties, the Reynolds numbers of these studied phenomena can be easily evaluated. These values remain in the unity range, proving that the fluid motion is developed in laminar regime, as expected for those pore-flow problems [27]. The velocity profile, in the peak of the oscillation, assumes the form presented in the figure below (Figure 5.22).

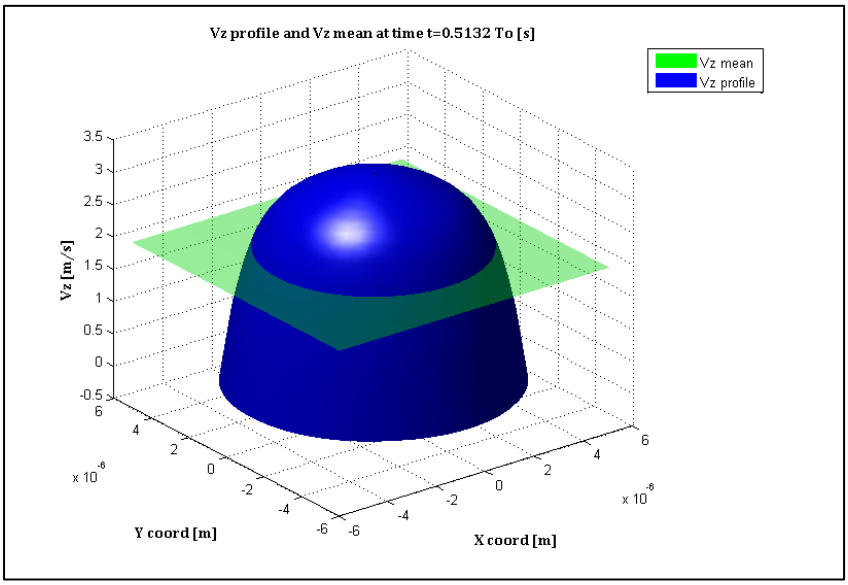

Figure 5.22 - Z-component of fluid velocity profile represented in blue with mean z-velocity indicated with the green plane. Profile obtained at a fixed time t/T_0=0.5132 with T_0 simulation time.

Pressure and velocity signals show that only after an initial transient evolution the mean oscillating term starts to set on an almost stationary value, and that's the part of the signal chosen for the acoustic impedance calculation. As seen before, impedance is defined as the ratio of complex pressure and complex velocity, that's why a Fourier transformation is required to express those signals into a sum of harmonic terms passing from time to frequency domain.
Performing this mathematical calculation, pressure and velocity signals have been expressed with their modulus and phase in the frequency domain as follows respectively in Figure 5.23, where the transformed signals for a frequency input of 1e07 are represented (the mean value of the series has been subtracted before the transform operation).

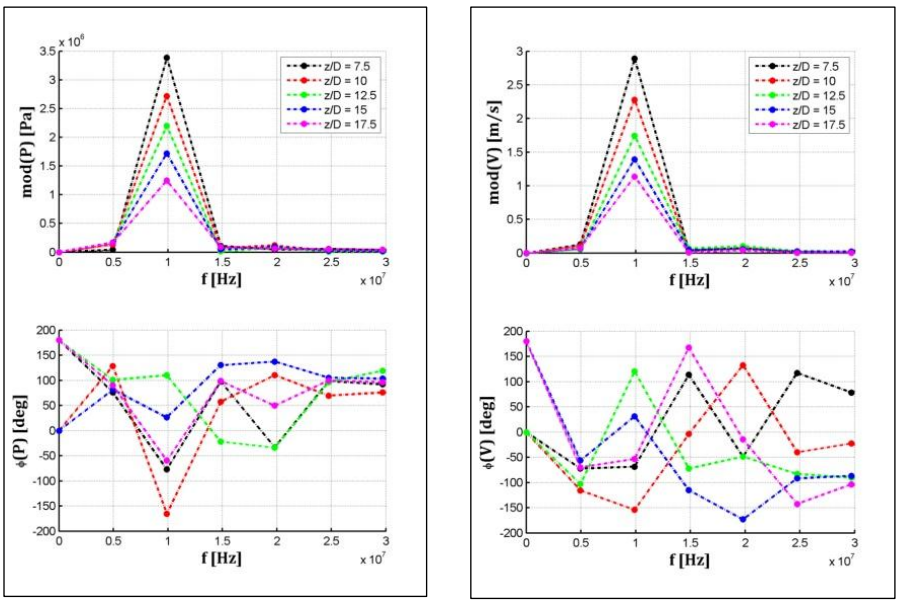

Figure 5.23 – Modulus and phase of pressure and velocity FFT.

Then, with those complex signals, the calculation of the acoustic impedance has been performed with the relations illustrated in chapter 3. Results of impedance can be resumed in the frequency domain plotting its modulus and phase (Figure 5.24), and also its real and imaginary parts (Figure 5.25), which can lead to very interesting considerations as well as to a better understanding of the phenomena in progress.

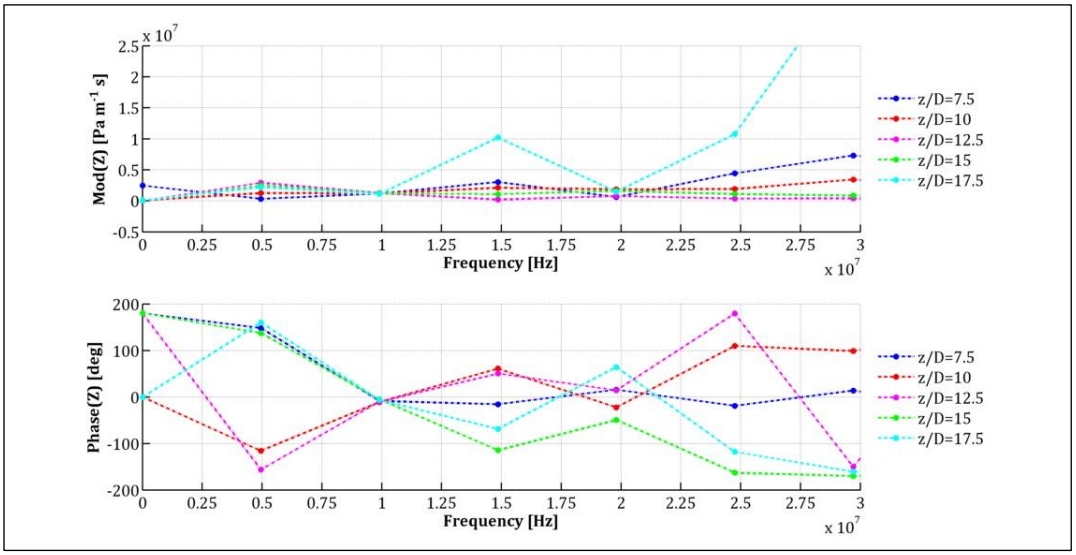

Figure 5.24 - Impedance modulus and phase in frequency domain for straight tube geometry and 10^7 Hz input signal.

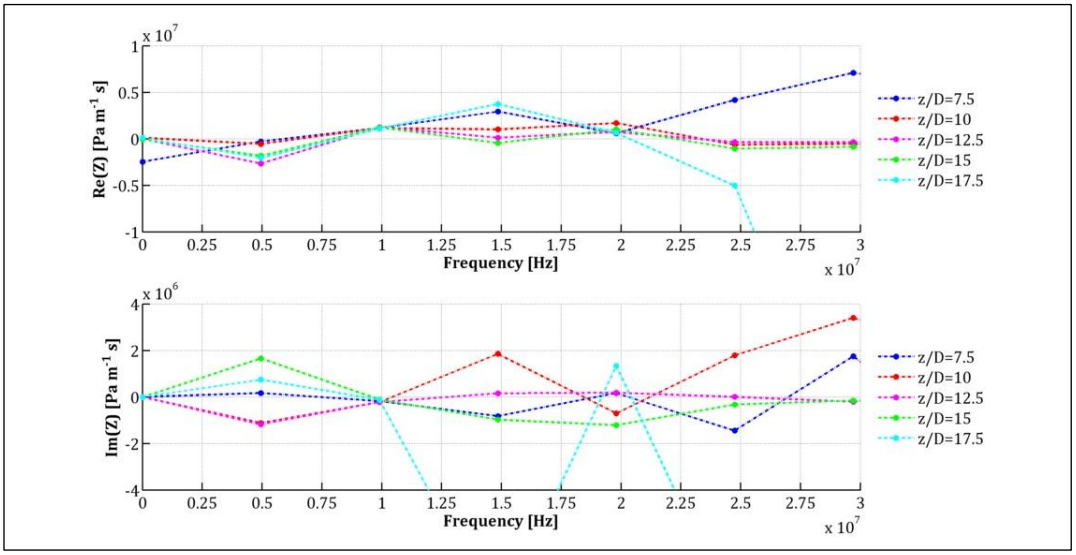

Figure 5.25 - Impedance real and imaginary in frequency domain for straight tube geometry and 10^7 Hz input signal.

Those figures show that, as expected from the results of the straight cylinder geometry, the impedance modulus, phase, real and imaginary part, in the nearby of the input frequency, remains almost constant.
Finally impedance results have been also represented in the spatial domain, displaying the values of the acoustic impedance for the input frequency only, in order to analyze the way each geometry influences this complex coefficient and provide relations between impedance and geometry variations (Figure 5.26, Figure 5.27).

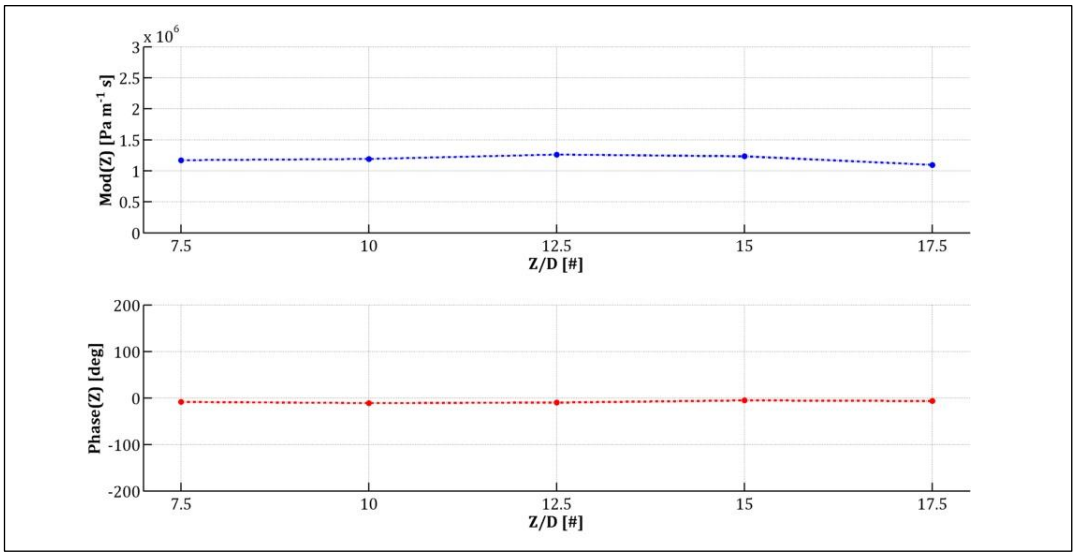

Figure 5.26 - Impedance modulus and phase in spatial non-dimensional domain for straight tube geometry and 10^7 Hz input signal.

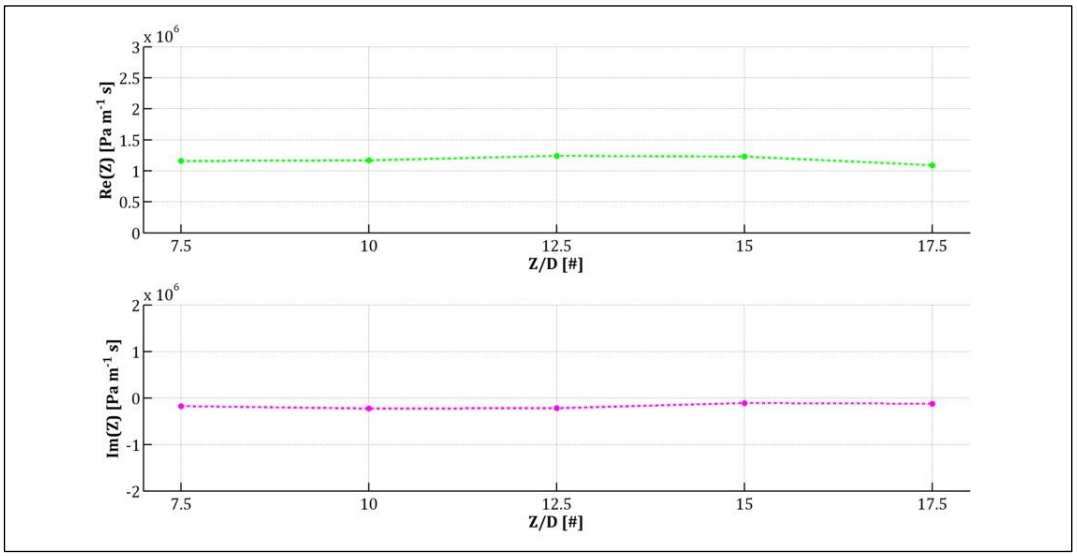

Figure 5.27 - Impedance real and imaginary part in spatial non-dimensional domain for straight tube geometry and 10^7 Hz input signal.

From a quick look of those graphs, it can be clearly seen what stated before for the impedance on frequency figures, but further observations can be performed. For

example, it was expected to find for the real part an almost constant value and close to the reference one obtained with ρc, which is slightly lower than 10^6 Pa·m^{-1}·s, and not to observe variation on the phase, which indicates a low or null effect of the acoustic dispersion on this phenomenon. Those expectations were properly respected in those results, and so they can be used as a good start for the analysis of other more complex domains. In the next two figures (Figure 5.28, and Figure 5.29) are resumed the results for the straight cylinder geometry for the three simulated input frequencies. As cited before, the three curves develop with an almost constant trend around the value of ρc for both modulus and phase and both real and imaginary part.

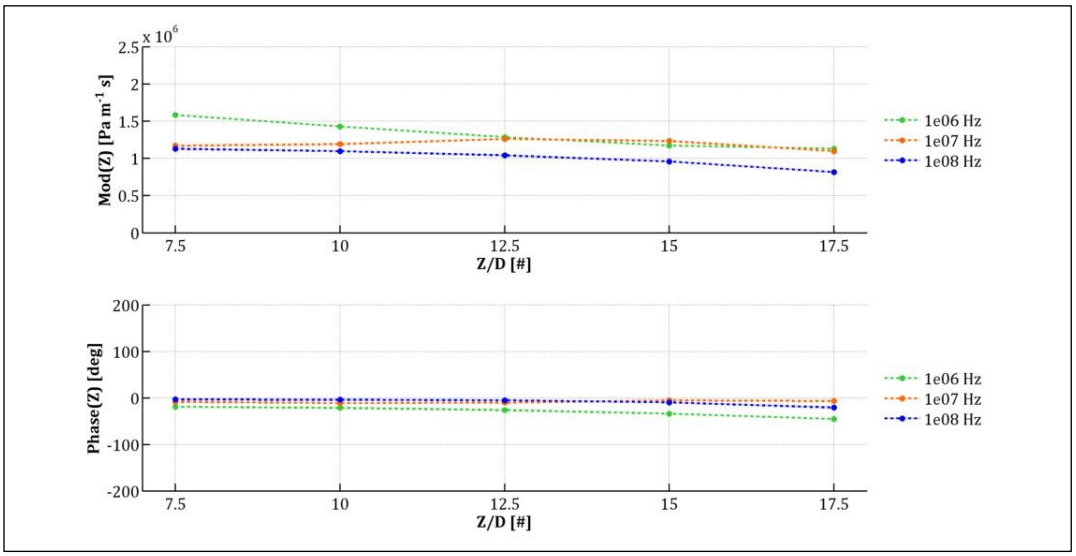

Figure 5.28 - Impedance modulus and phase in spatial non-dimensional domain for straight tube geometry and every simulated input frequency.

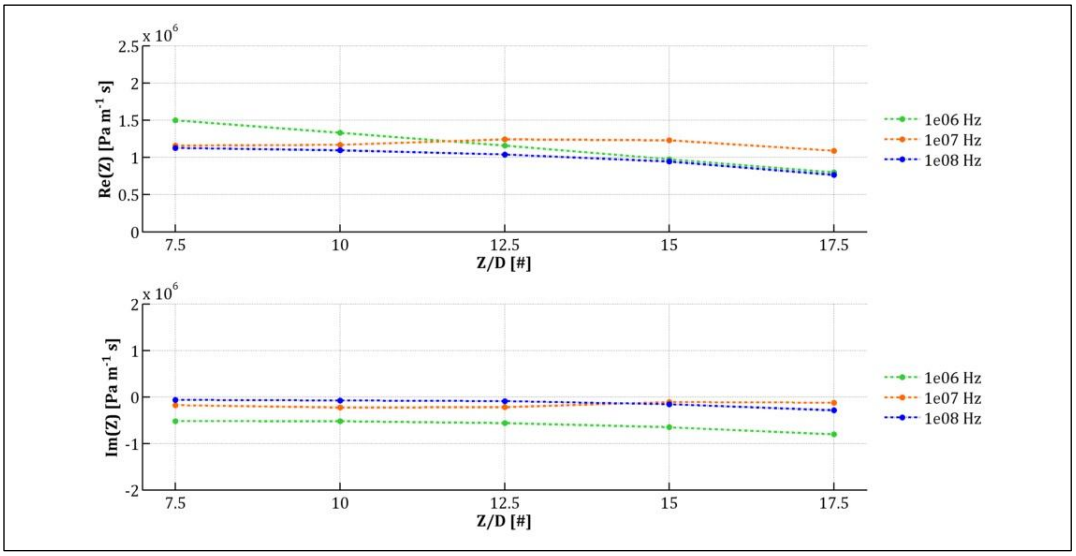

Figure 5.29 - Impedance real and imaginary part in spatial non-dimensional domain for straight tube geometry and every simulated input frequency.

5.7.2 Elbow geometry

The same procedure has been adopted for the other geometries. In this paragraph the results for the elbow geometry are shown.

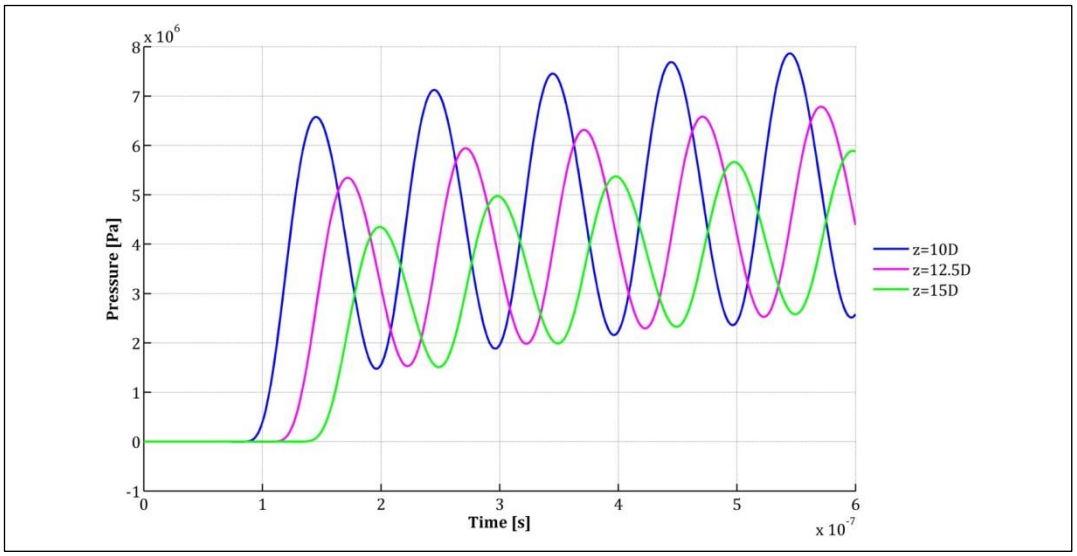

Figure 5.30 - Pressure signal for 10^7 Hz input frequency for elbow geometry.

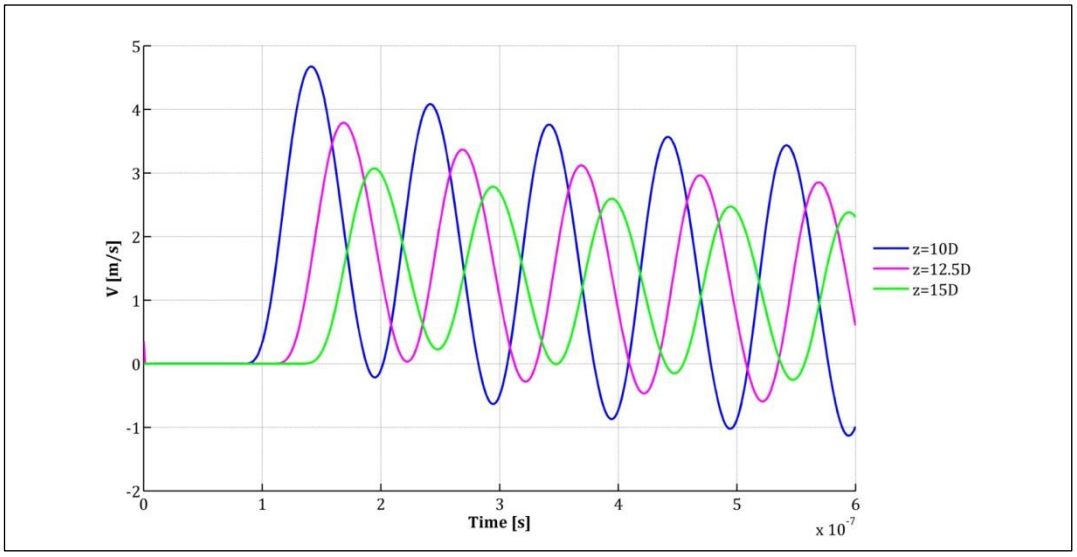

Figure 5.31 - Velocity signal for 10^7 Hz input frequency for elbow geometry.

Pressure and velocity signals, for each input frequency studied, are similar in shape to the ones obtained with the straight tube geometry (Figure 5.30 and Figure 5.31) and their effect on the impedance evolution along the channel are also analogue in terms of evolution through the domain and values, with the exception of the results obtained for the frequency 10^8 Hz (Figure 5.32 and Figure 5.33).

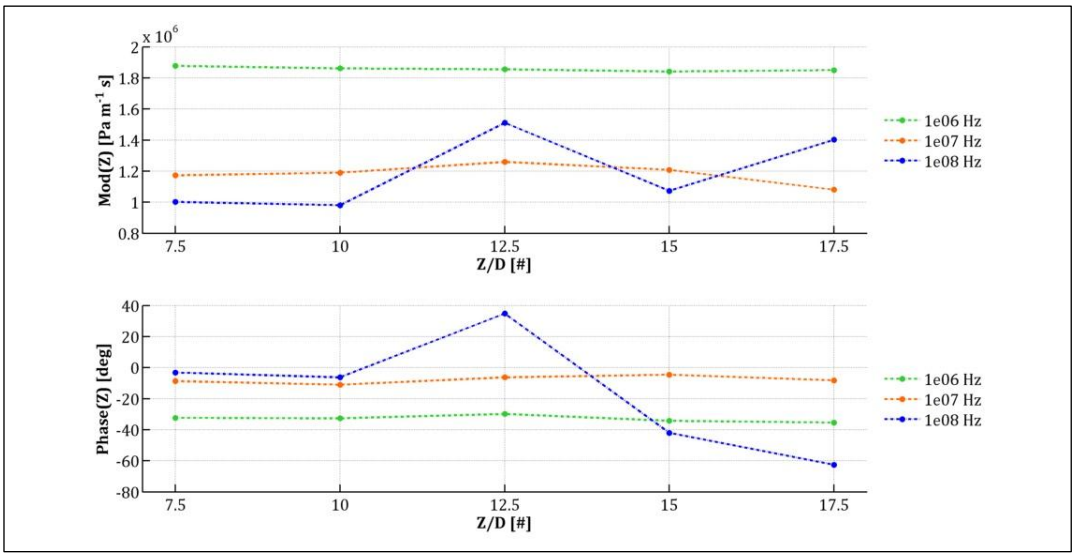

Figure 5.32 - Impedance modulus and phase in spatial non-dimensional domain for elbow geometry and every simulated input frequency.

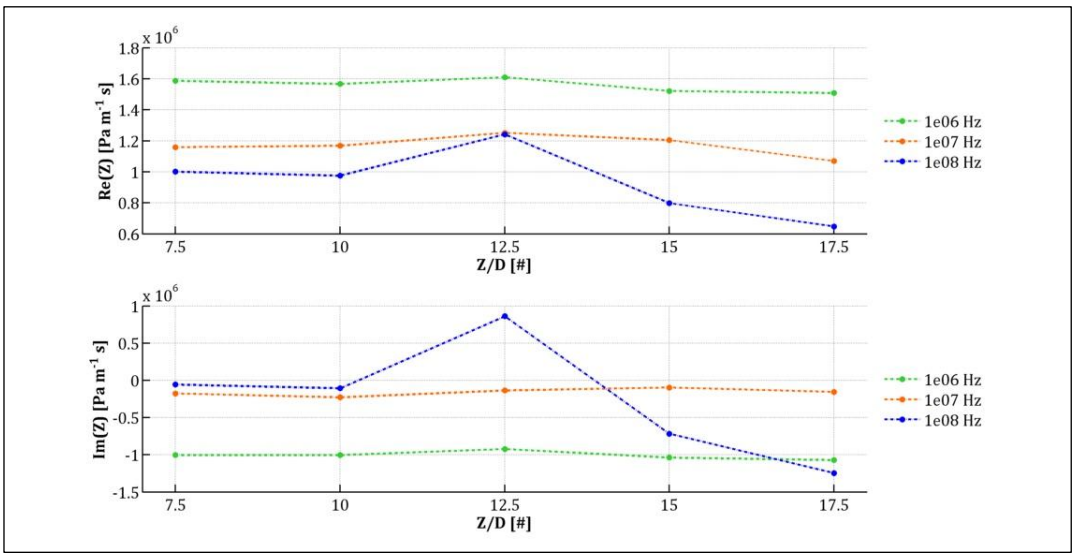

Figure 5.33 - Impedance real and imaginary part in spatial non-dimensional domain for elbow geometry and every simulated input frequency.

This phenomenon occurs because of the wavelength of the 10^8 Hz, which is in the order of 10^{-5} m, becoming comparable with the geometry representative length, the channel diameter, which equals to 10^{-5} m.
That's why, spreading the point of view from one dimensional to two dimensional, other (higher-order) modes of propagation are formed by interference between plane waves propagating in non-axial directions, as it can be seen in (Figure 5.34). The interference field is of course the result of multiple reflections of sound from the parallel walls.

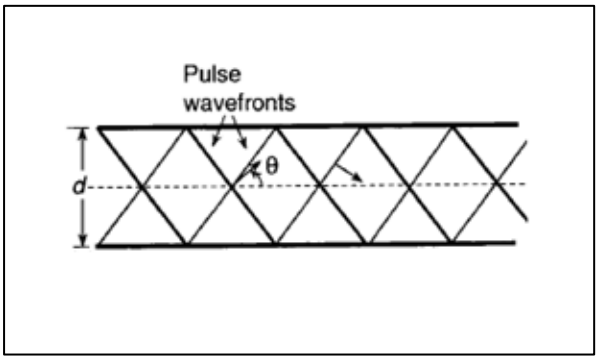

Figure 5.34 - Reflections on rigid walls of a waveguide (Frank J. Fahy, Foundations of Engineering Acoustics*, 2001).*

In summary, in duct of given width, a particular angle of plane pulse propagation is uniquely associated with a harmonic series of frequencies for a given speed of sound in the fluid. The corollary of this statement is that any temporally harmonic sound field within a waveguide may be decomposed into a set of harmonic plane waves travelling in a number of discrete directions, and this number is increasing with frequency. A qualitative physical explanation of this behavior is provided by (Figure 5.35). The spatial phase gradient of the pressure field produced by interference between the incident plane wave and that reflected from the bend wall increases with frequency. The interference field therefore becomes increasingly less well matched to a plane wave field in the downstream leg, which has uniform phase over the cross-section. The mismatch reaches a maximum when the waveguide width equals a half wavelength, that is a situation similar to the studied one.

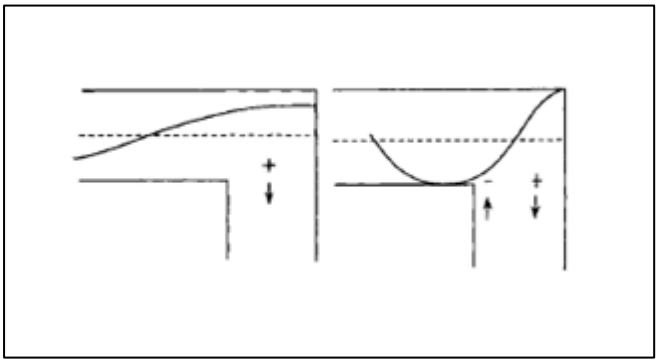

Figure 5.35 - Effects of wavelength on the signal propagation after the elbow (Frank J. Fahy, Foundations of Engineering Acoustics*, 2001).*

In conclusion, the elbow geometry acts like a uniform straight tube geometry as long as the wavelength of the input signal remains significantly larger than the duct diameter. If this wasn't so, the imaginary part grows and becomes inertive, due to the accelerations created in this case.

5.7.3 Enlargement geometries

In this paragraph the results for the enlargement geometries are shown.

5.7.3.1 Enlargement type 1

First of all pressure and velocity signals has been analyzed. In the following figures are resumed signals for the frequency 10^7 Hz.

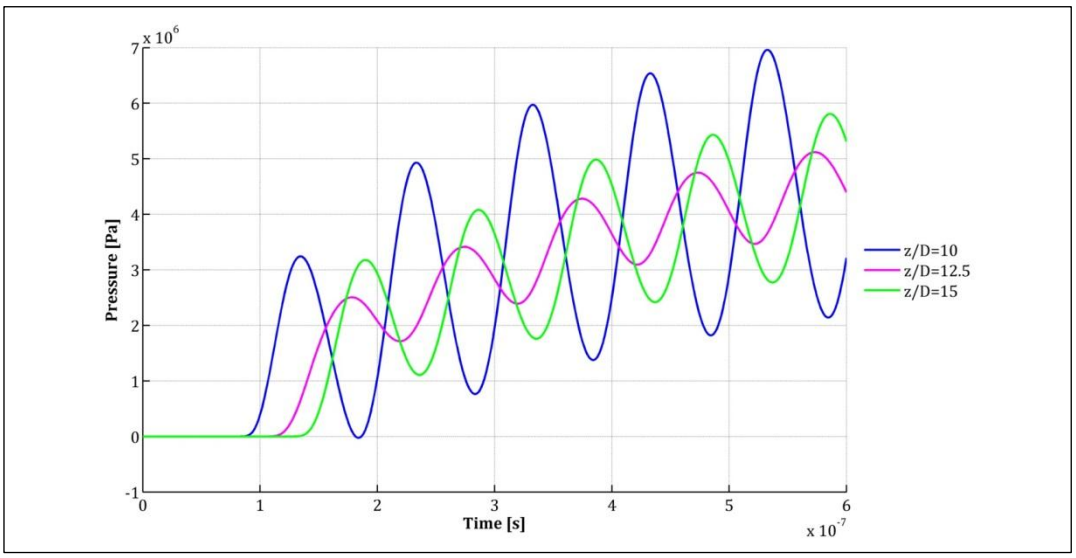

Figure 5.36 - Pressure signal for 10^7 Hz input frequency for enlargement type 1 geometry.

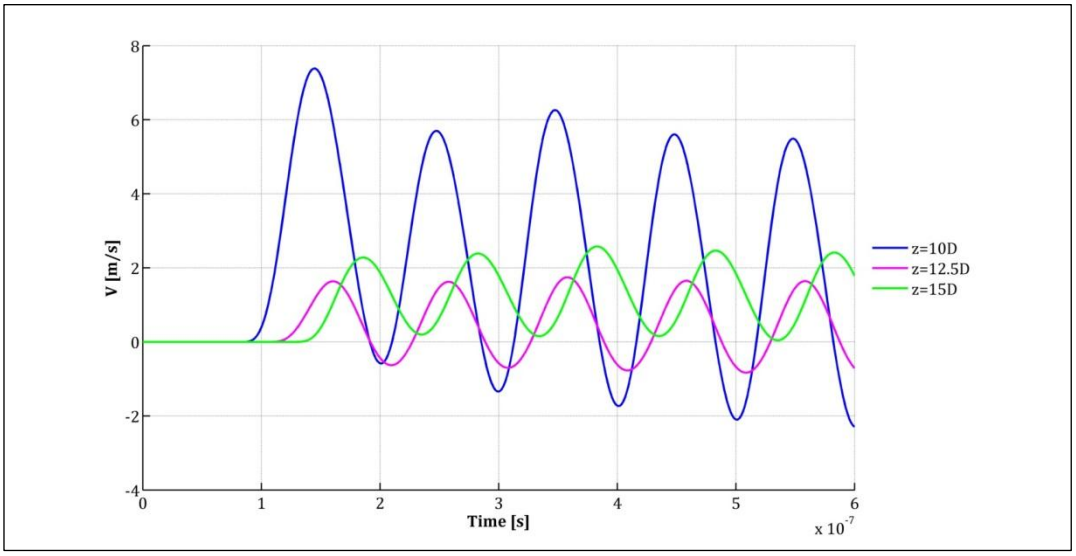

Figure 5.37 - Velocity signal for 10^7 Hz input frequency for enlargement type 1 geometry.

From Figure 5.37 it can be clearly seen that the mass conservation is correctly respected because of the decreasing, in comparison with the expected value, of the velocity in the middle of the singularity.
Transforming those signals and evaluating the acoustic impedance at various sections, the charts below can be obtained (Figure 5.38 and Figure 5.39).

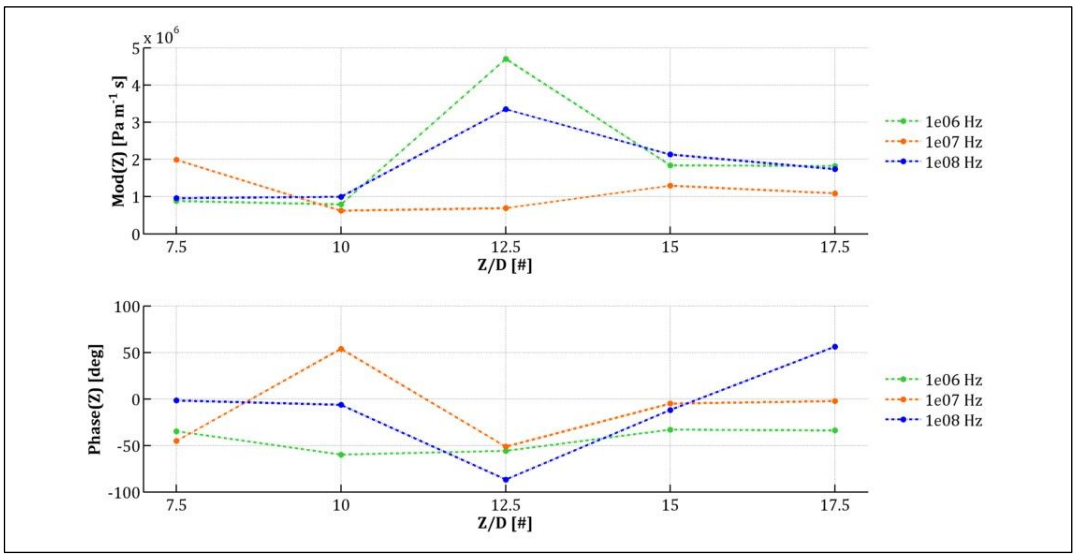

Figure 5.38 - Impedance modulus and phase in spatial non-dimensional domain for enlargement type 1 geometry and every simulated input frequency.

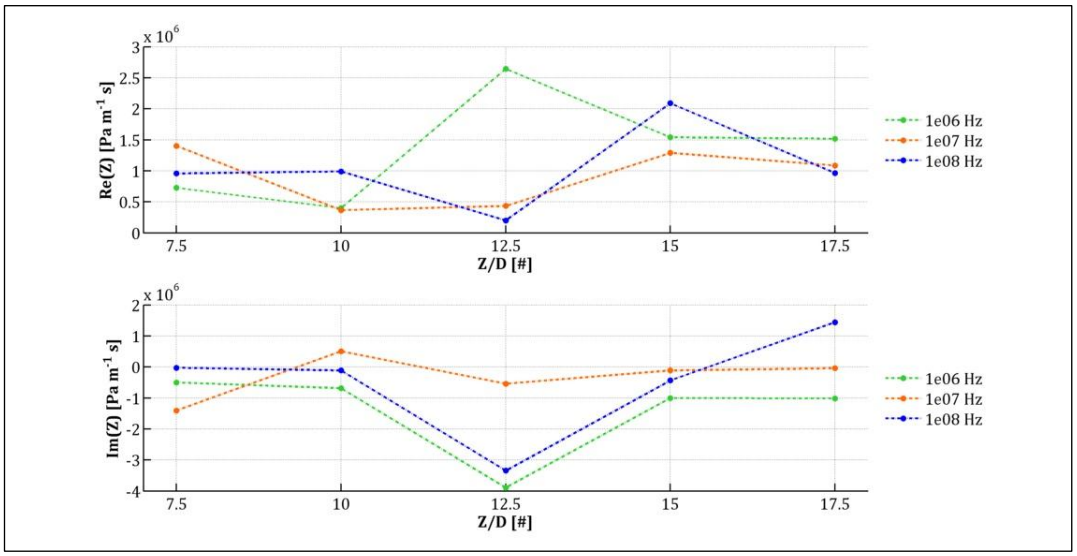

Figure 5.39 - Impedance real and imaginary part in spatial non-dimensional domain for enlargement type 1 geometry and every simulated input frequency.

To correctly evaluate those results, it is useful to analyze what physically happens to a wavelet encountering a singularity as an abrupt change of section. If this area changes abruptly at some point, the associated change of impedance will cause incident waves to be reflected. The acoustic flow field in immediate vicinity of the

area discontinuity cannot be one-dimensional and plane. Non-plane sound fields are generated but, at low frequencies, they are confined to the immediate vicinity of the discontinuity, and only plane waves can propagate and transport energy. The effect of the discontinuity is to introduce an additional inertial impedance associated with the local kinetic energy of the non-planar particle motion. And that's what it can be seen at the non-dimensional distance of 10 z/D.
To explain the low peaks in the negative field of the impedance imaginary part values, that represent an increasing of the stiffness reactance of the system, a classical example may become useful. This is the archetypal Helmholtz resonator, consisting of a neck and cavity, shown in Figure 5.40. At the fundamental resonance frequency, the dimensions of both components are much less than an acoustic wavelength and can thus be treated as lumped elements coupled at a geometric discontinuity. The coupling condition is that the oscillatory volume flow in the neck is equal to that imposed on the fluid in the cavity. A volume of fluid in an acoustically small enclosure that acts like an elastic spring. The acoustic impedance of the cavity of volume V_0 is given by $Z = -j\gamma P_0/\omega V_0$. The acoustic impedance of the fluid in the neck is inertial in nature and given by $Z=j\omega\rho_0 l/S$ where l and S are the length and cross-sectional area of the neck, respectively. Because the fluid in the neck behaves like an incompressible mass, the impedances of the neck and cavity add to give the internal reactance X_{int} given to pressure imposed on the external opening of the neck.

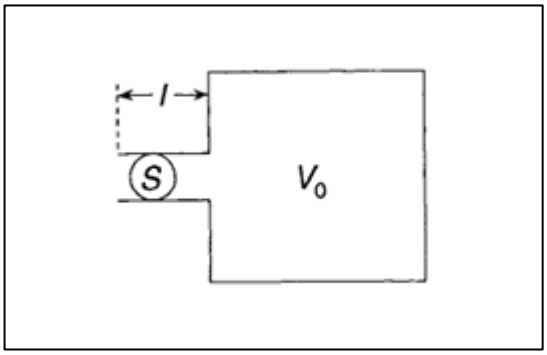

Figure 5.40 - Archetypal Helmholtz resonator (Frank J. Fahy, Foundations of Engineering Acoustics*, 2001).*

If kl << 1, the fluid in the neck is so stiff that it moves virtually as an incompressible volume, its acceleration being controlled by its inertia. Hence, the smaller of the two components of neck impedance controls the motional response.
For these reasons it is observable in Figure 5.39 that the imaginary part is more negative in the middle of the enlargement than in other sections. The real part seems to increase for frequencies not comparable with the diameter of the duct because in section 12.5 z/D the cross section is bigger and friction has less influence on the motion. For the frequency of 10^8 Hz real part is smaller because of the effects due to the small wavelength of the signal that causes local accelerations and dissipations.

5.7.3.2 Enlargement type 2

For this type of geometry pressure and velocity signals don't differ much in shape from those obtained with the enlargement type 1 (Figure 5.41), except from the boundary layers created by the different cross section transitions, and consequently impedance results remains qualitatively similar (Figure 5.42 and Figure 5.43) and the observations that can be brought out are mainly the same.. For a quantitative evaluation, better observations will be done in paragraph 5.7.5 where all geometry results are compared.

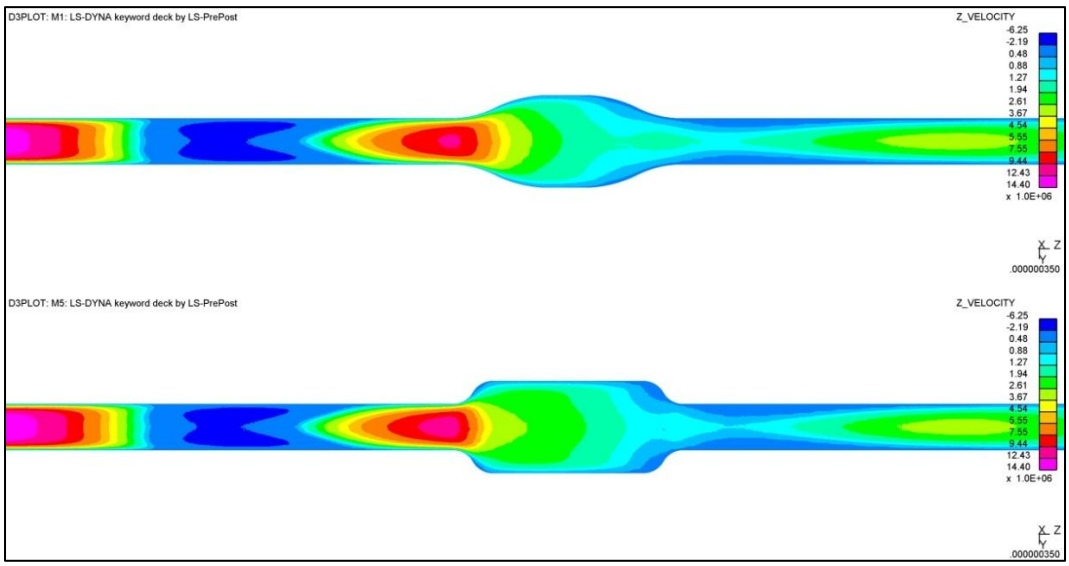

Figure 5.41 - Enlargement type 2 and type 1 velocity distributions at time t=3.5e-07 s. Velocities in micron/s.

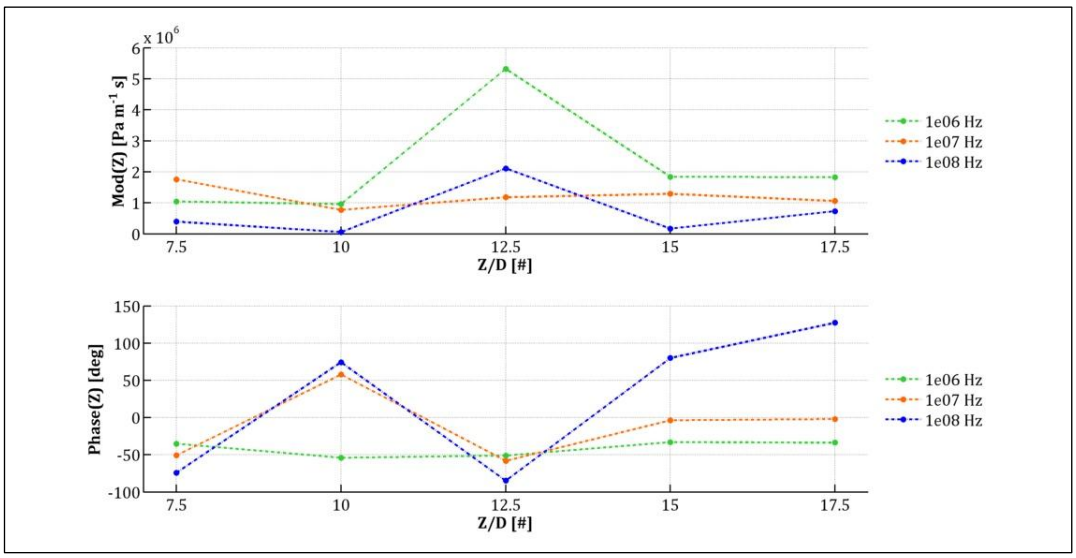

Figure 5.42 - Impedance modulus and phase in spatial non-dimensional domain for enlargement type 2 geometry and every simulated input frequency.

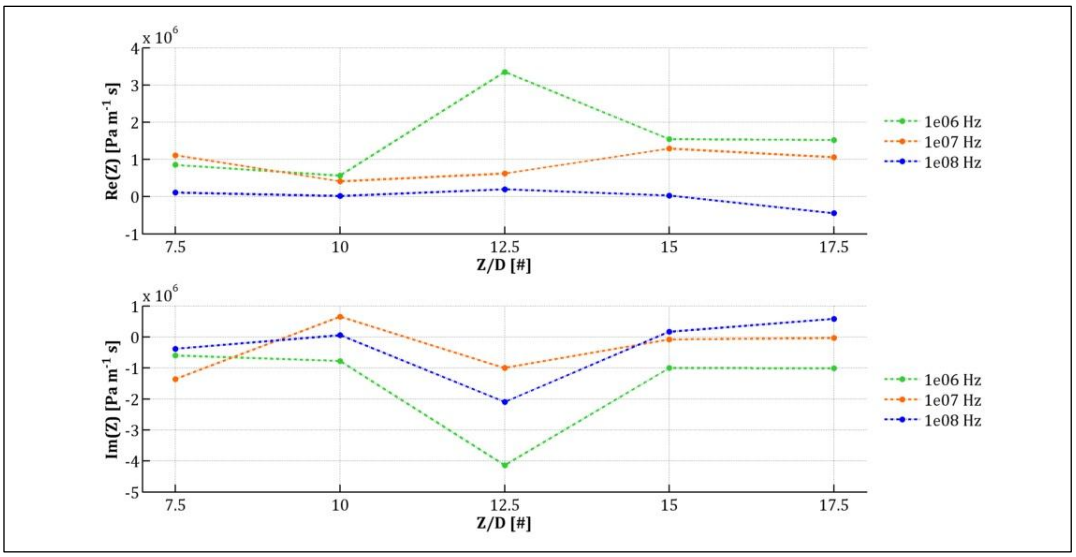

Figure 5.43 - Impedance real and imaginary part in spatial non-dimensional domain for enlargement type 2 geometry and every simulated input frequency.

5.7.4 Constriction geometry

Results for pressure and velocity signal are presented in Figure 5.44 and Figure 5.45.

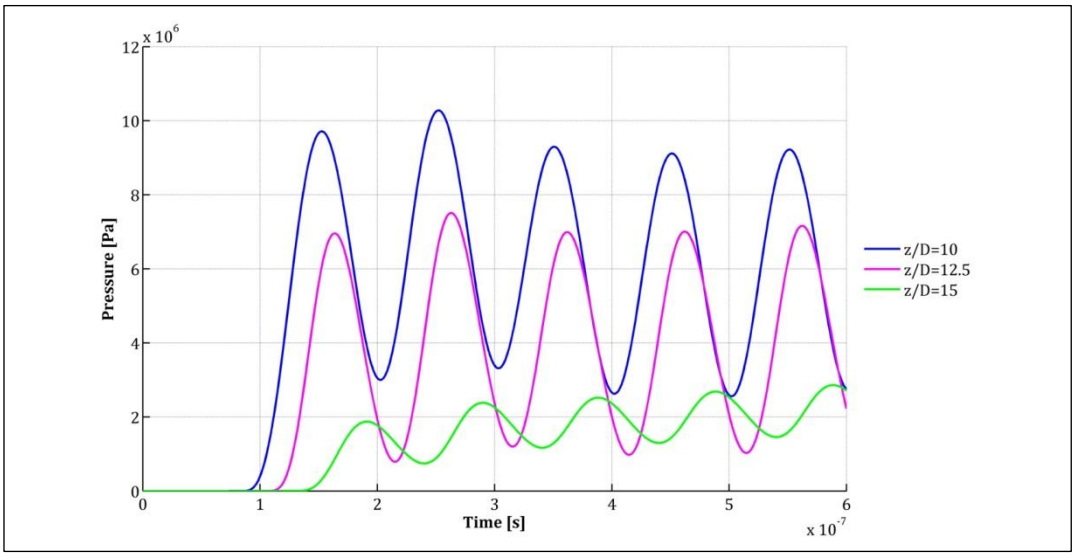

Figure 5.44 - Pressure signal for 10^7 Hz input frequency for constriction geometry.

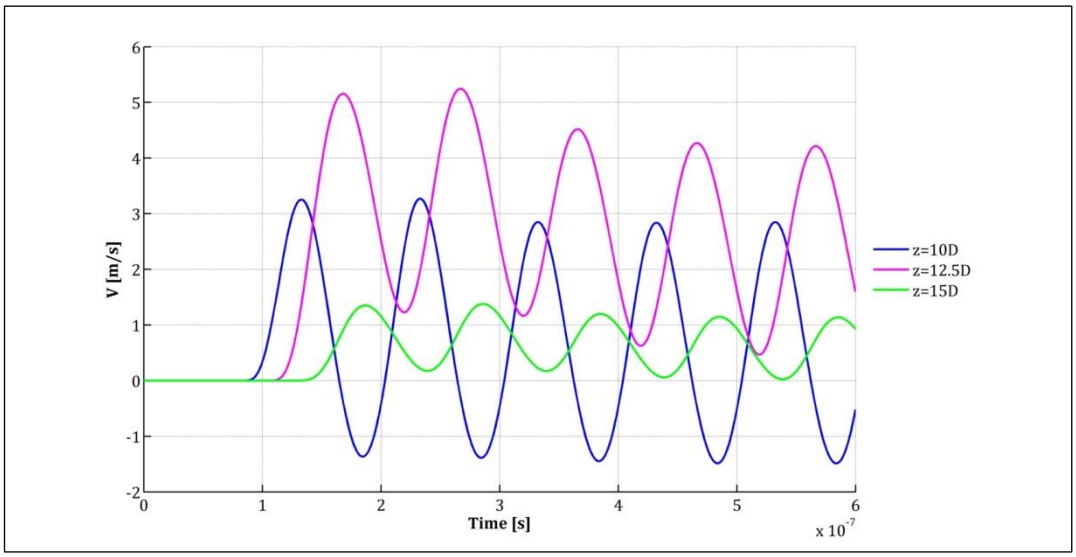

Figure 5.45 - Velocity signal for 10^7 Hz input frequency for constriction geometry.

From Figure 5.45 it can be easily seen the effect of the constriction, which increases fluid velocity in section 12.5 z/D, as the conservation of mass predicts. This geometry can also be seen as the specular case, from the point of view of the section variations, of the enlargements, and this aspect is reflected on velocity field (Figure 5.46) and impedance results (Figure 5.47 and Figure 5.48).

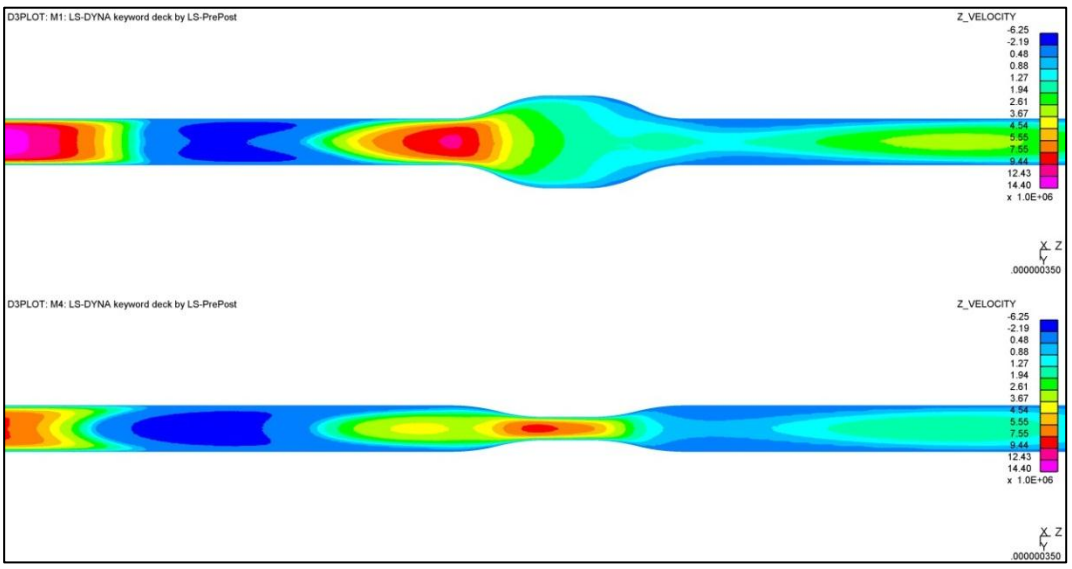

Figure 5.46 - Enlargement type 2 and constriction velocity distributions at time t=3.5e-07 s. Velocities in micron/s.

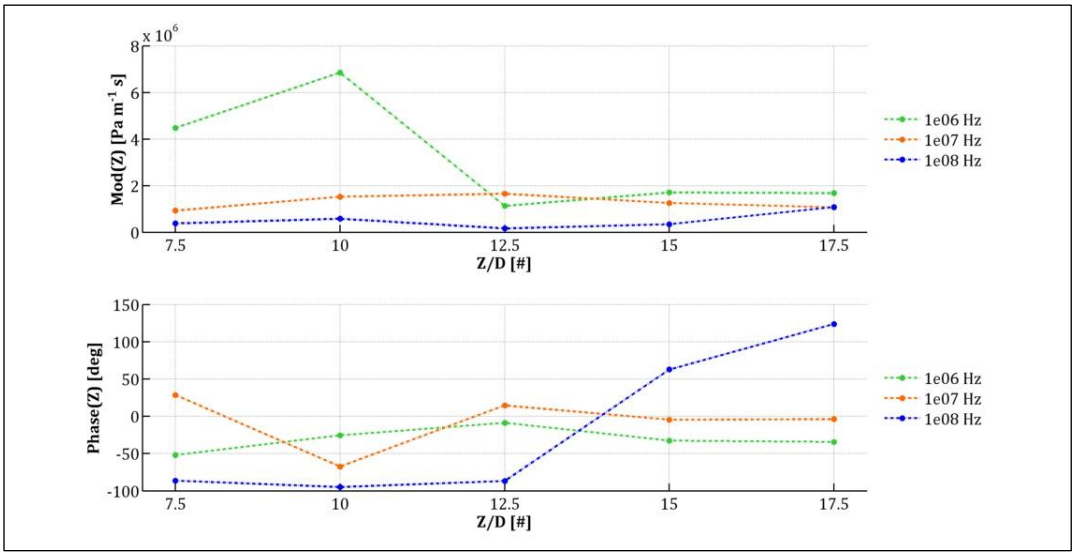

Figure 5.47 - Impedance modulus and phase in spatial non-dimensional domain for constriction geometry and every simulated input frequency.

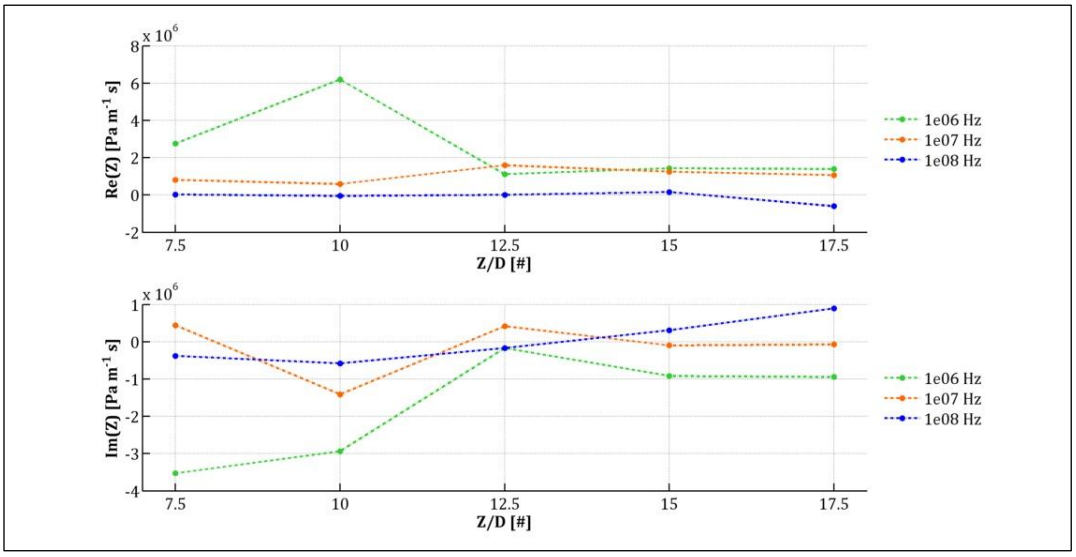

Figure 5.48 - Impedance real and imaginary part in spatial non-dimensional domain for constriction geometry and every simulated input frequency.

In facts, remembering the Helmholtz resonator example, in the constriction zone the imaginary part of the impedance grows tending to positive values, as a prove that the inertive reactance is increasing, while in the larger section zones imaginary part is strongly stiffness regulated (z/D=10).
Looking at the real part, frequency 10^8 Hz is very dissipative and this is translated in the small real part values assumed. That's because strong resistive phenomena occurs during the interference and interaction of the signal and the structure.

5.7.5 Results comparison

For a better understanding of the geometry change influence on the acoustic impedance, results have been plotted for every simulated geometry with a fixed value of input frequency.

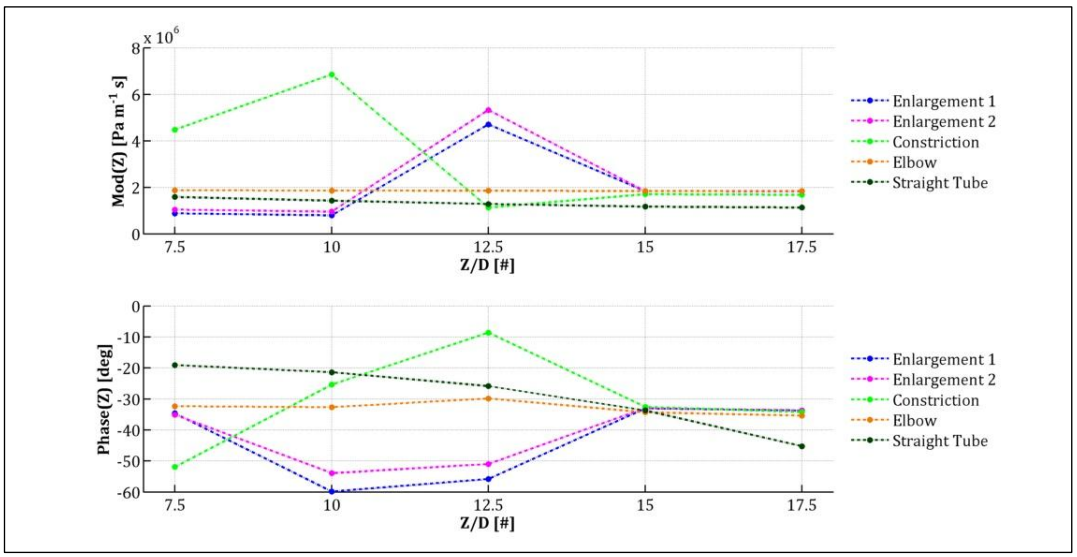

Figure 5.49 - Impedance modulus and phase the in spatial non-dimensional domain for every simulated fluid geometry for an input frequency of 10^6 Hz.

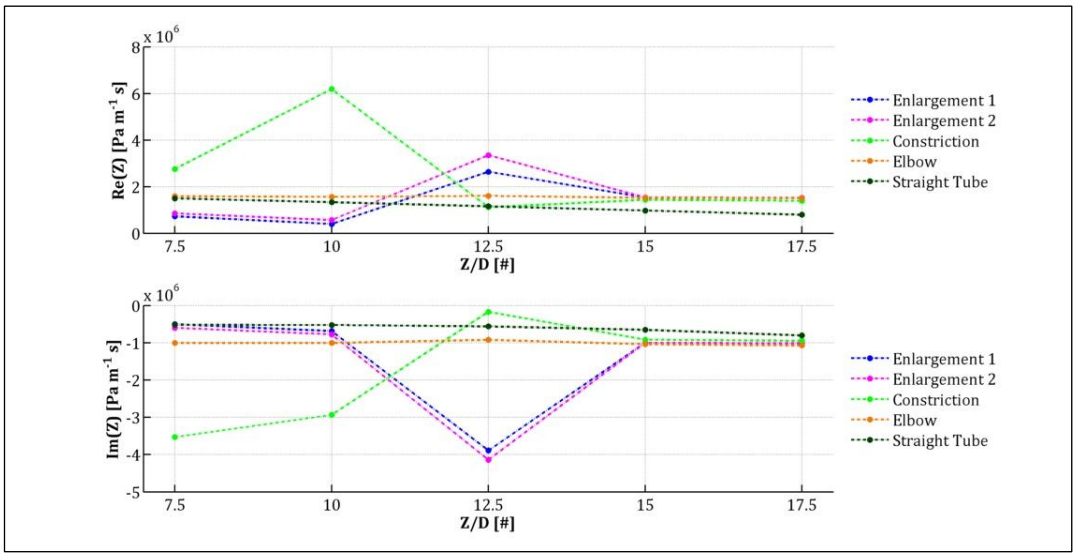

Figure 5.50 - Impedance real and imaginary part in the spatial non-dimensional domain for every simulated fluid geometry for an input frequency of 10^6 Hz.

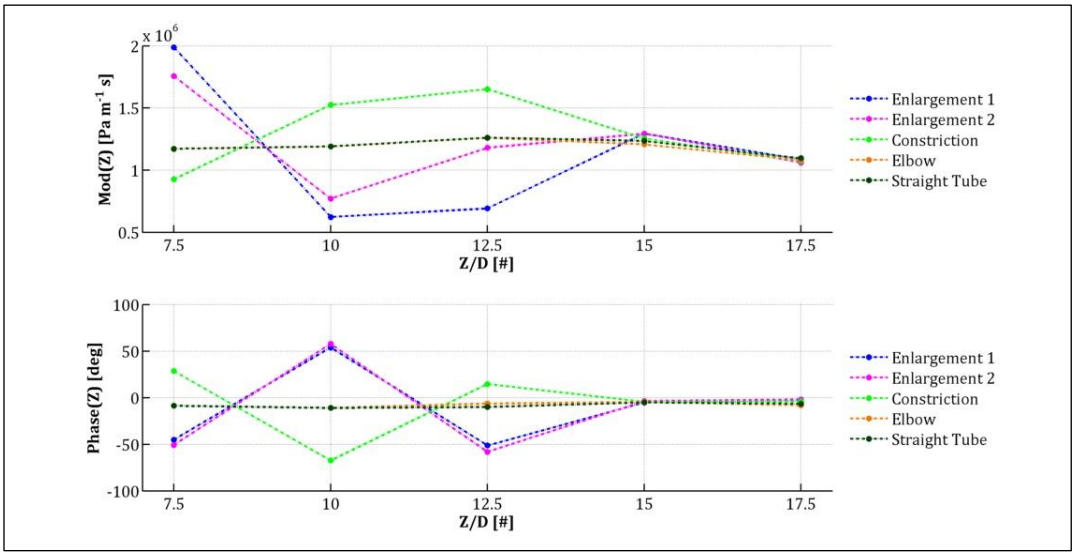

Figure 5.51 - Impedance modulus and phase in the spatial non-dimensional domain for every simulated fluid geometry for an input frequency of 10^7 Hz.

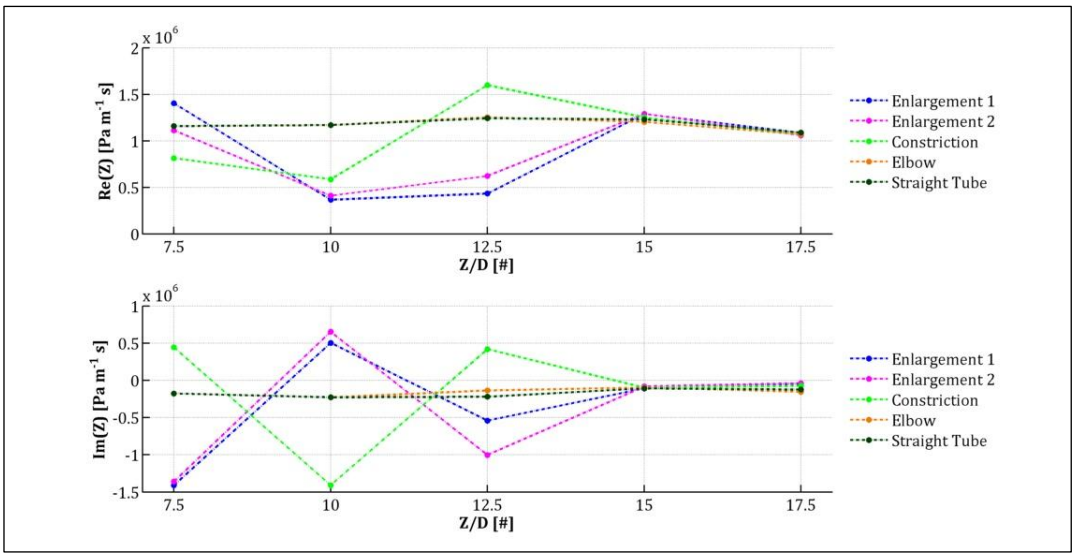

Figure 5.52 - Impedance real and imaginary part in the spatial non-dimensional domain for every simulated fluid geometry for an input frequency of 10^7 Hz.

With regard to the two frequencies with a wavelength non comparable with the diameter of the channel, that is to say 10^6 and 10^7 Hz, the results seems to obey to the physics of the considered phenomena just looking at real and imaginary parts and considering the analysis carried out in the previous paragraph. Enlargements and the constriction have specular behaviors, while the elbow and the straight tube act almost the same way.

A particular consideration has to be done looking at what happens in the space non-dimensional domain after the various singularities. At both the considered frequencies the impedance values at 15 and 17.5 z/D tend to the ones achieved by the straight tube, that can considered as non-perturbed. That's because the transmitted wave regulates its pressure and velocity with respect to the impedance

of the sections that encounters during its proceeding, which is almost constant considering the uniformity of the geometry and the fluid parameters after the singularities. On the other hand, the same thing can't be said for the sections that precede the singularity, even though the domain here is still uniform without abrupt changes of direction or cross section. As a matter of fact the incident wave that hits the singularity creates, in addition to the transmitted wave, a reflected wave that travels in the opposite direction, and that can be positive or negative depending on the boundary encountered by the incident wave (see the velocity distribution changes before the singularity in Figure 5.46 caused by the different reflected waves). Moreover, this reflected wave hits the input signal section and again reflects itself. Those mechanisms represent what would really happen in the proximity of the input section, that's why the analysis in this zone should only be qualitative.

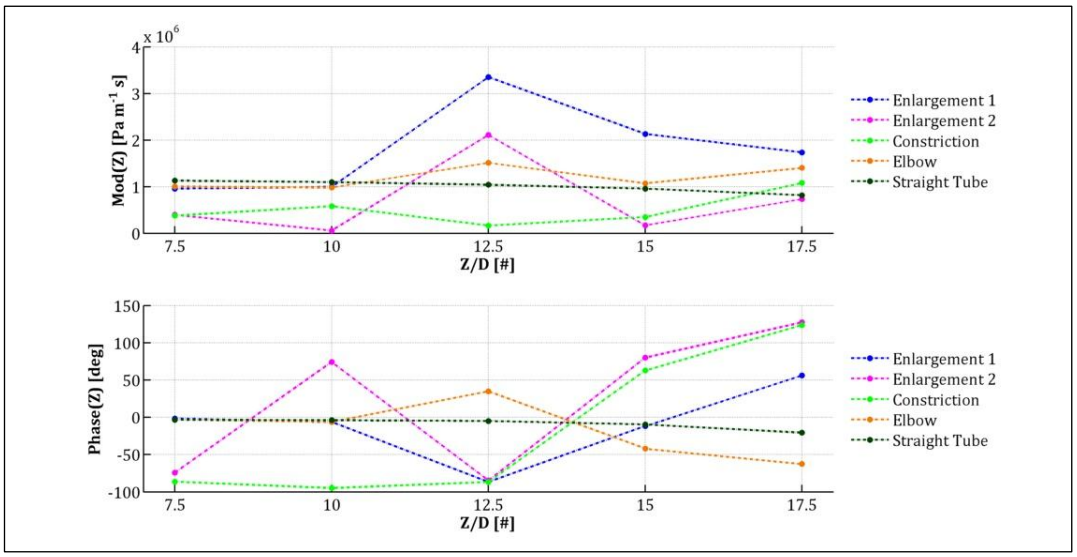

Figure 5.53 - Impedance modulus and phase in the spatial non-dimensional domain for every simulated fluid geometry for an input frequency of 10^8 Hz.

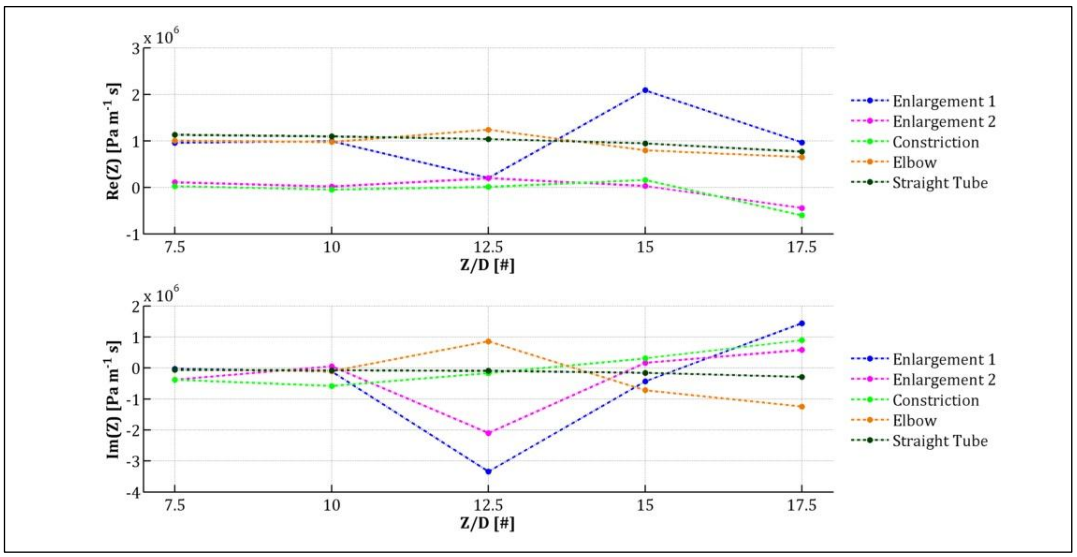

Figure 5.54 - Impedance real and imaginary part in the spatial non-dimensional domain for every simulated fluid geometry for an input frequency of 10^8 Hz.

Analyzing the input frequency with a wavelength comparable with the duct diameter, i.e. 10^8 Hz, one of the first thing we noticed is the disturbance of the elbow results that detach from the straight tube trend, unlike what happens for the lower frequencies, as said in the previous paragraphs. Another important difference is the loss of agreement between the results of the two types of enlargements. This happens because in the enlargement type two, and also in the constriction geometry, another dimensional aspect turns to be comparable with the input signal wavelength: the transition length of the section variations, which is two times the diameter while in the enlargement type 1 is half the diameter. In fact, in cases where the transition is less abrupt, such as a short conical adaptor for example, if the transition length is not much less than a wavelength, an acoustic horn model is required, which includes reflections created not approximately in a single section, but in a greater length, but this problem is not further treated in this study.

6 Fluid-Structure Interaction analysis

6.1 Overview of the problem

Fluid geometries explored so far were considered as isolated from the rock portion of the soil sample, leading to an analysis of the single fluid phase surrounded by a solid material non-reactive to the fluid stresses on fluid-solid interfaces. This equals to say that the rock taken in consideration was a rigid material, with an infinite Young modulus. Let's now add complexity to those models considering the solid part of the system as reacting with the fluid, with fixed features resumed in Table 6.1, inching closer to model the real physics of the problem.

	Symbol	**Value**	**[#]**
Density	ρ	2300	kg/m^3
Elastic modulus	E	10.5	GPa
Poisson coefficient	ν	0.3	-
Sound velocity	c	2137	m/s

Table 6.1 - Rock portion main features.

With the aim to correctly simulating this condition, a Fluid-Structure Interaction analysis has to be performed, using the solver LS-DYNA previously chosen in Chapter 4.
The pressure wave imposed by the membrane on the inlet face of the model acts on both fluid and solid portions, so it would be useful, for a clearer understanding of the physics at stake, to divide the effect of the wave travelling in the single fluid phase on the solid part from the stress wave travelling in the single solid part. This condition is achievable keeping at rest the solid phase in the initial conditions, and so only the interaction forces on the fluid-solid interface would act on the rock portion through, for example, Poisson effect.

6.2 FSI geometries

To correctly evaluate the effect of the elasticity of the solid phase on the oil field, the same geometries of the previous chapter have been modeled, adding an external solid layer to the fluid domains considered, having the features of the rock stated above. Since the solid is elastic and reacting to the fluid pressure, its thickness becomes an important variable of the problem. It's been decided to maintain the pore average distance of the order of magnitude of the diameter of the pores, to represent the situation that can be found, for instance, in a sandstone sample.

6.2.1 Straight tube

As for the fluid geometries analysis, the straight tube conditions have been considered first, establishing a basic situation used as comparison for other complex geometries.

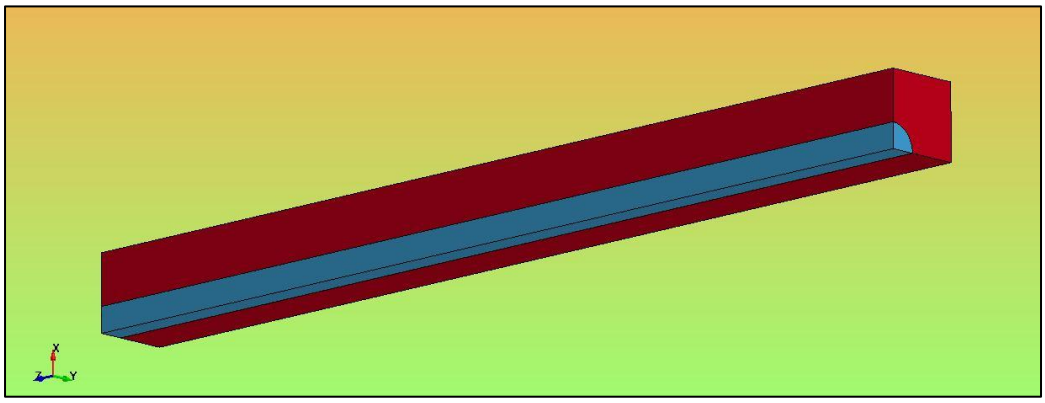

Figure 6.1 - Straight tube FSI domain. Fluid part is represented in light blue and solid part in red.

A representative block of porous soil has been considered, with a square cross section (with constant dimensions for every simulation performed) and a channel, representing the fluid, digged from the solid block, which results excavated in the interior. The fluid-solid interface can be seen as the negative of the fluid external surface.
With the aim of reducing the simulation times, for each geometry modeled it's been decided to consider a quarter of the entire domain section, as it can be seen in Figure 6.1, imposing symmetric boundary conditions on the correct surfaces to simulate the full section conditions.
The fluid channel has been modeled with the same diameter D adopted for the fluid geometries, that is to say D =10 μm. Accordingly to what stated before, rock minimum thickness has been chosen to be also 10 μm (Figure 6.2). Those quantities are the same for the other FSI geometries for the sections far from the singularities, where the diameter and the solid thickness will obviously vary case by case. Fluid and solid domains lengths are the same for every simulated geometry, and they are equal to 20 times the diameter to appreciate what happens in the proximity of the singularity.

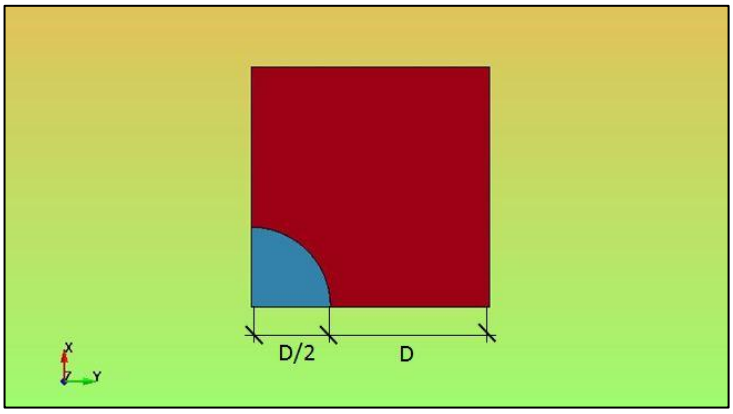

Figure 6.2 - Straight tube geometry section.

6.2.2 Enlargement geometry

An FSI geometry has been modeled also to simulate an enlargement, traced on the second type of enlargement considered in the fluid geometries chapter. The fluid section starts to vary after 10 diameters in the longitudinal direction from the inlet surface, as in the homologue fluid domain (Figure 6.3).

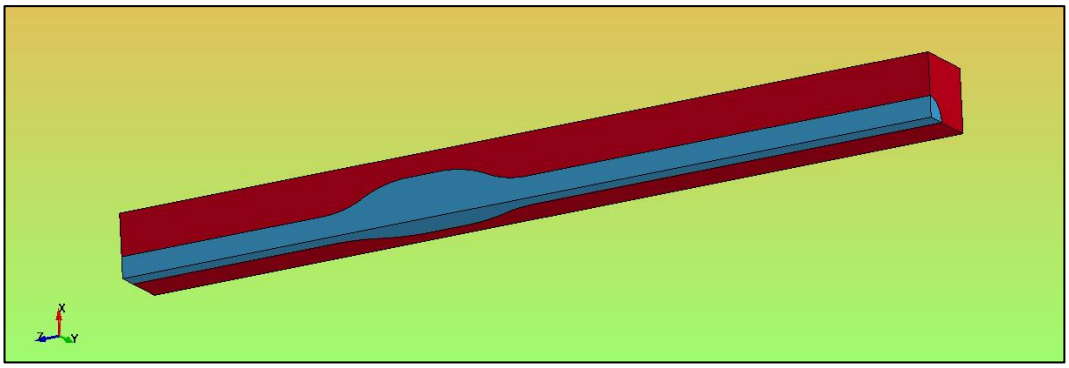

Figure 6.3 - Enlargement FSI domain. Fluid part is represented in light blue and solid part in red.

Enlarged section is twice the channel diameter and the transition length, from the channel section to the enlarged section, is again 2D with a solid thickness in the singularity of half the diameter (Figure 6.4). The rock minimum thickness is half the diameter.

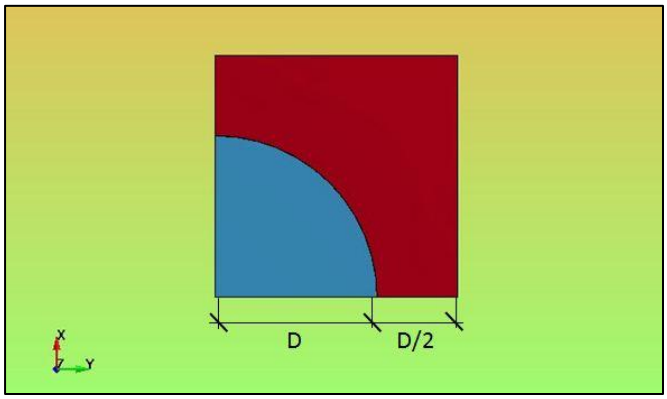

Figure 6.4 – Enlargement FSI geometry section.

6.2.3 Constriction geometry

Based on the constriction fluid geometry described in paragraph 5.2.4, a FSI domain has been modeled to represent a reduction of the cross section of a fluid channel surrounded by solid material (Figure 6.5).

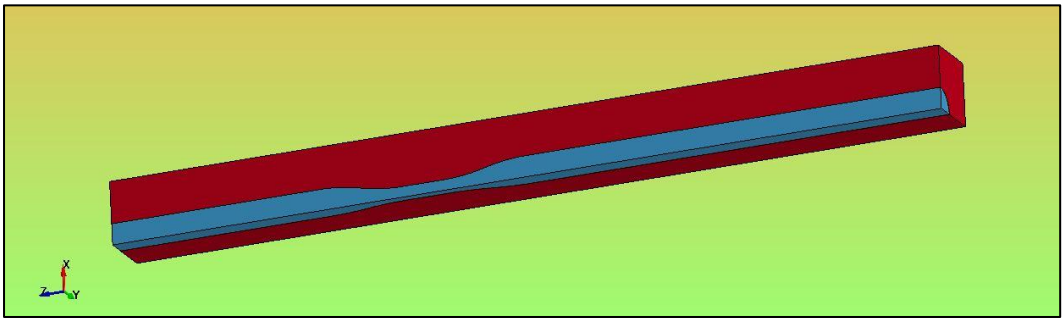

Figure 6.5 - Constriction FSI domain. Fluid part is represented in light blue and solid part in red.

The restricted section, achieved after a transition length of 2D, has a diameter of half the diameter of the fluid channel, and of course a radius of D/4. The solid section is the remaining part, that is to say with a minimum thickness of 5/4D (Figure 6.6).

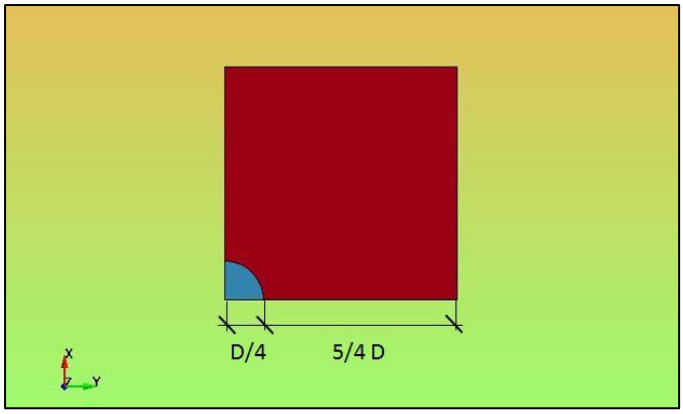

Figure 6.6 – Constriction FSI geometry section.

6.3 Boundary conditions

6.3.1 Constraints

Since a quarter of the entire domain has been simulated, symmetry boundary conditions have been imposed on the sectioned surfaces A and B in the fluid domain, C and D in the solid domain (Figure 6.7), that can been as motional and stress constraints on those surfaces.
Furthermore, this representative block is meant to be part of bigger domain composed with many of these blocks one beside the other in an infinite replication. To simulate this situation, two other symmetry conditions have been imposed on the surfaces E and F.
The inlet solid surface G has been fixed in the longitudinal direction constraining the translation along the z-axis. This condition neglects the charges imposed on this solid surface.

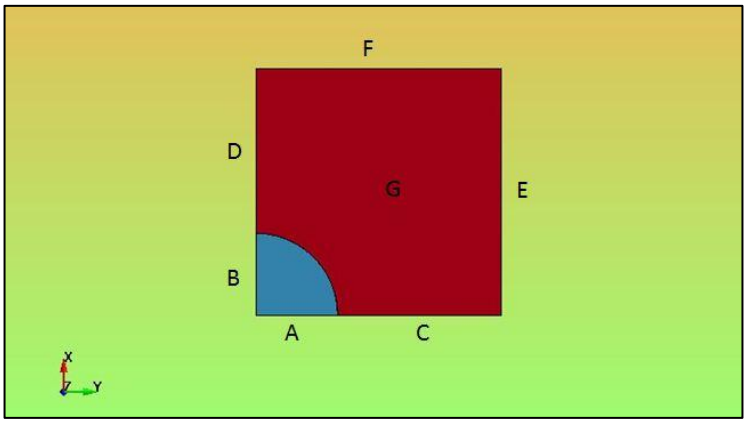

Figure 6.7 - Surfaces with imposed boundary conditions.

6.3.2 Inflow and outflow conditions

The inlet surface of the fluid has been charged with the same wavelet trains used for the fluid simulations plotted in Figure 5.7 and Figure 5.8. On solid surface at z=0 no stress has been superimposed. On outlet surfaces of both fluid and solid domains non-reflective boundary conditions have been imposed, to create an anechoic termination which models the conditions that would happens in an infinite domain in z direction.

6.3.3 Initial conditions

At the time instant t=0 both fluid and solid systems have been modeled completely at rest.

6.4 Mesh implementation

The domains discretization has been performed with the software *Gambit*, which has provided a good hexahedral mesh both for fluid and solid parts of the system. Figure 6.8 shows the discretization adopted for a section of the model.

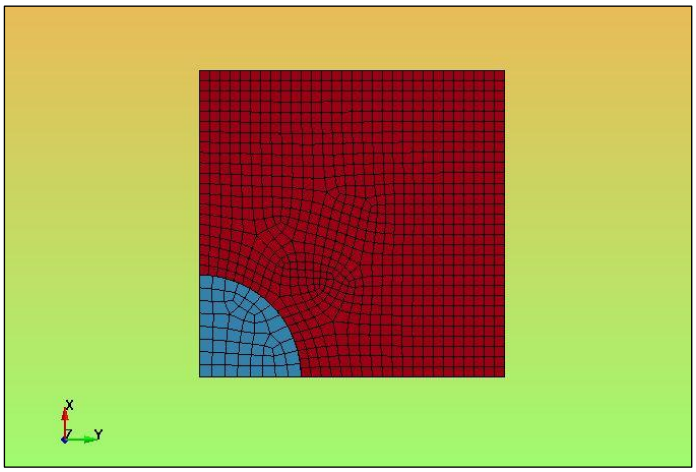

Figure 6.8 - Discretization for fluid and solid domains.

In the following table (Table 6.2) are resumed the main features of the mesh volumes used for this chapter calculations. Every geometry has been meshed so as to obtain a number of nodes and elements to achieve the right solution both for fluid and solid domains, and to make every fluid element of the fluid-solid boundary interface with at least two solid elements, this to perform a good FSI calculation.

	Straight Tube	**Enlargement**	**Constriction**
Solid Elements	386295	390540	387144
Solid Nodes	414504	419049	415413
Fluid Elements	17528	17584	18840
Fluid Nodes	22294	22365	23625

Table 6.2 – FSI meshes main characteristics.

6.5 Simulation times

In this paragraph are resumed the main time features of the simulations performed. The table below (Table 6.3) shows the integration time-step, the results saving time-step, the end time adopted for every frequency simulation, and the mean simulation length.

	1.00E+06	**1.00E+07**	**1.00E+08**
dt of integration	1.00E-11	1.00E-11	1.00E-11
dt of saving	1.00E-09	1.00E-09	1.00E-10
Sim. time	4.50E+06	6.00E-07	6.00E-07
Average sim. duration	15h	2h	2h

Table 6.3 – FSI simulation times.

6.6 Results

Pressure and velocity results have been extracted for some sections of interest placed every 2.5 times the diameter of the fluid channel starting from the z=0 inlet section. This procedure has been adopted to provide a better point view of the influence of the geometry on the acoustic impedance values, posing sections before, within and after each singularity, as shown in Figure 6.9. Pressure and velocity are extracted for the fluid part, in order to analyze, in conclusion, the differences between fluid domain surrounded by a rigid body or an elastic body with the properties of the considered rock. The analysis of the stress in the solid matrix will be carried out in the next chapter.

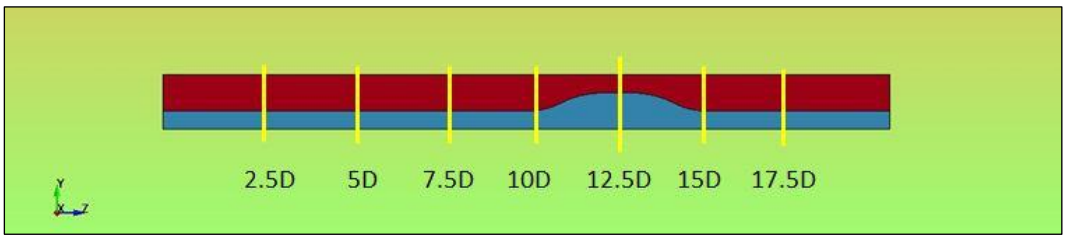

Figure 6.9 - Monitored sections for every FSI domain simulation.

After obtained those results, the same procedure executed for the fluid geometry analysis has been performed, transforming those pressure and velocity signals with FFTs and calculating the impedance value for each section monitored.

6.6.1 Straight tube geometry

Pressure and velocity signals are shown in Figure 6.10 and Figure 6.11 to understand how a wave train travels in the fluid part of a so structured FSI domain.
An important phenomenon, characteristic of those FSI problems, can be immediately recognized: the presence of a wave with smaller amplitude preceding the fluid pressure wave. In paragraph 4.2.1, thanks to the analysis of water hammer waves performed by Tijsseling, it has been introduced the presence of the so called "precursor wave", generated by the fluid stressing the solid part, travelling in the solid matrix, and obviously reacting on the fluid. This is visible before the incoming of the fluid pressure inlet perturbation because of the difference of phase velocity between fluid and solid media.

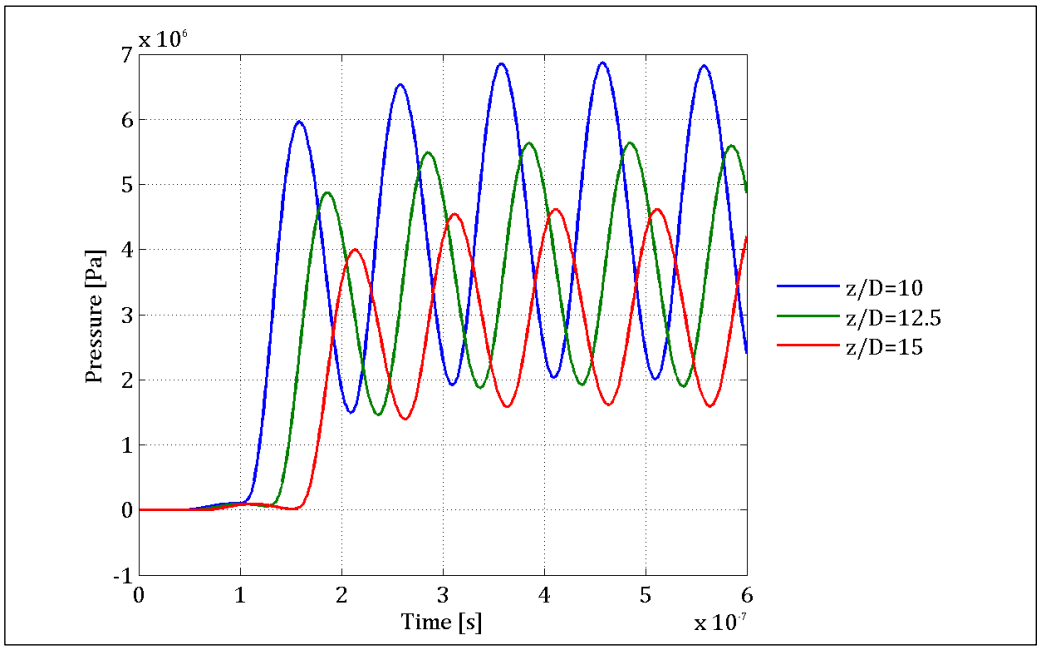

Figure 6.10 – Fluid pressure signals for the straight tube FSI geometry for an input pressure of 10^7 Hz.

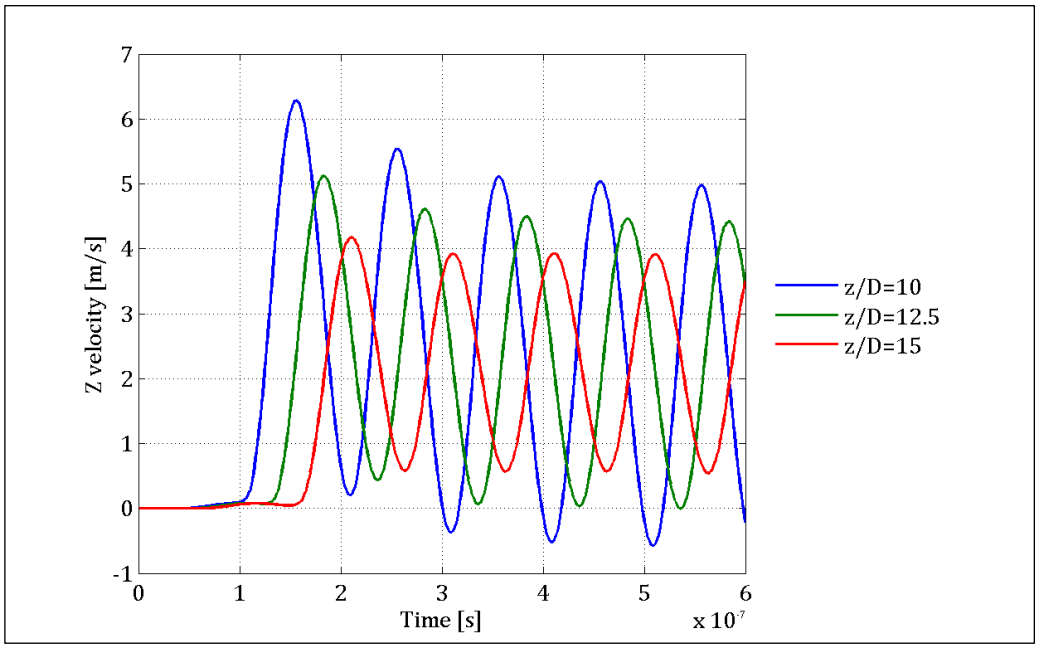

Figure 6.11 – Fluid velocity signals for the straight tube FSI geometry for an input pressure of 10^7 Hz.

In Figure 6.12 is shown the consequence of this difference in phase velocity, and the precursor wave is clearly visible. In this case its amplitude is still smaller with respect to the fluid pressure wave, but in the next chapter, while analyzing the effects of different constraints configurations, its magnitude will increase and play an important role on the pressure distributions both in the fluid and the solid phase.

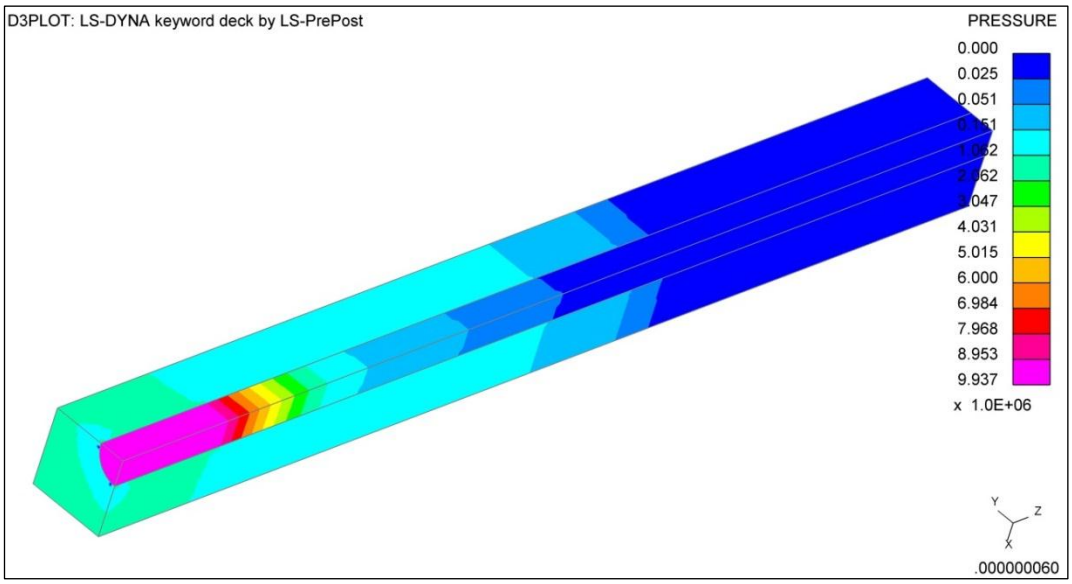

Figure 6.12 - Pressure distributions in both fluid and solid parts at time t=6e-08 for input pressure of 10^7 Hz. The precursor wave is clearly visible.

For a complete analysis the pressure signal results for the other input frequencies have been plotted (Figure 6.13, Figure 6.14). In the 10^6 Hz signal the precursor wave is no more observable, while in the 10^8 Hz signal, because of the high frequency and its comparability with the channel diameter, different fluctuation can be seen, and this is the same for the velocity signals. The effect of this frequency is similar to those detected in Figure 4.30 for the FSI analysis of the test case in chapter 4, but with constant pressure applied in the inlet surface.

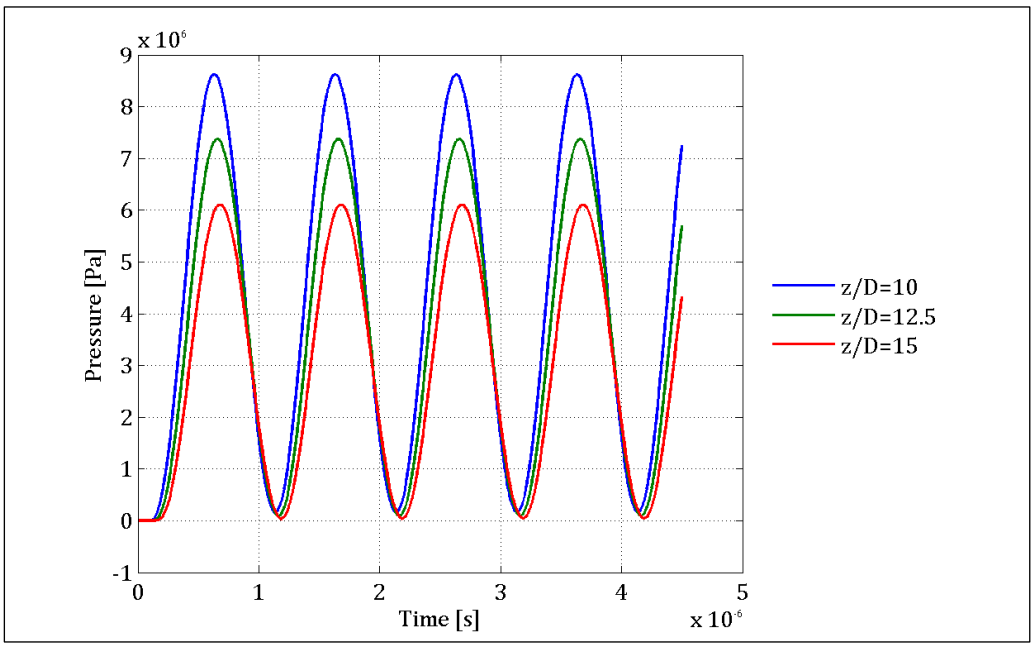

Figure 6.13 – Fluid pressure signals for the straight tube FSI geometry for an input pressure of 10^7 Hz.

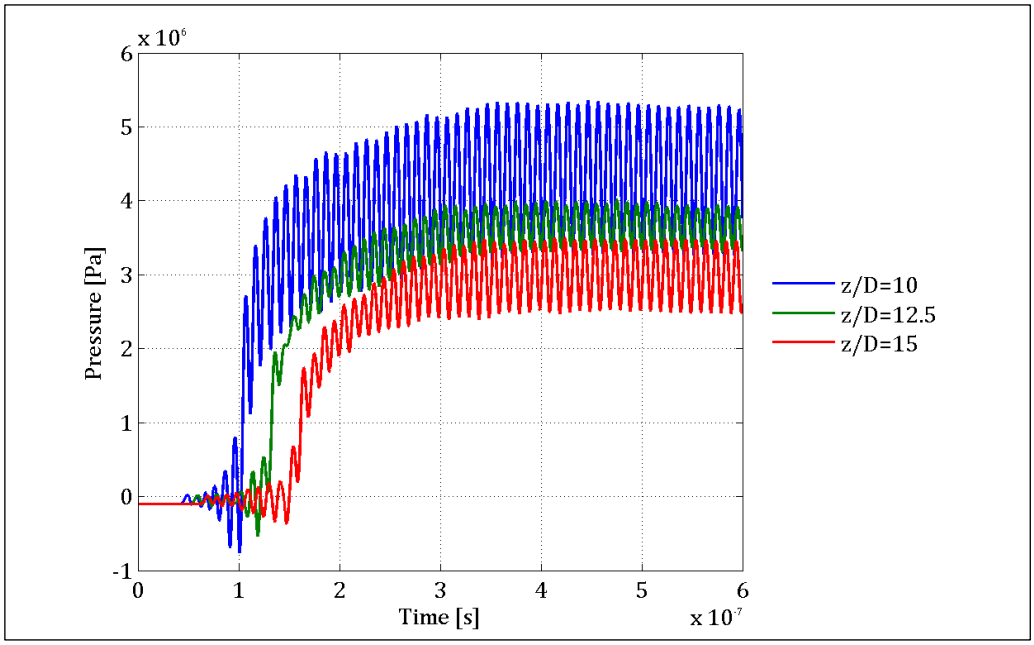

Figure 6.14 – Fluid pressure signals for the straight tube FSI geometry for an input pressure of 10^7 Hz.

On the other hand, the solid part is also reacting deforming its interface with the fluid channel, in Figure 6.15, are shown the solid part z-stress component with the interface displacements, those magnified 1000 times because their value is very small with respect to the domain dimensions. The first two waves of the train entered the domain and the third is entering in the inlet sections, where the stresses are stronger also because of the presence of the constraint reactions.

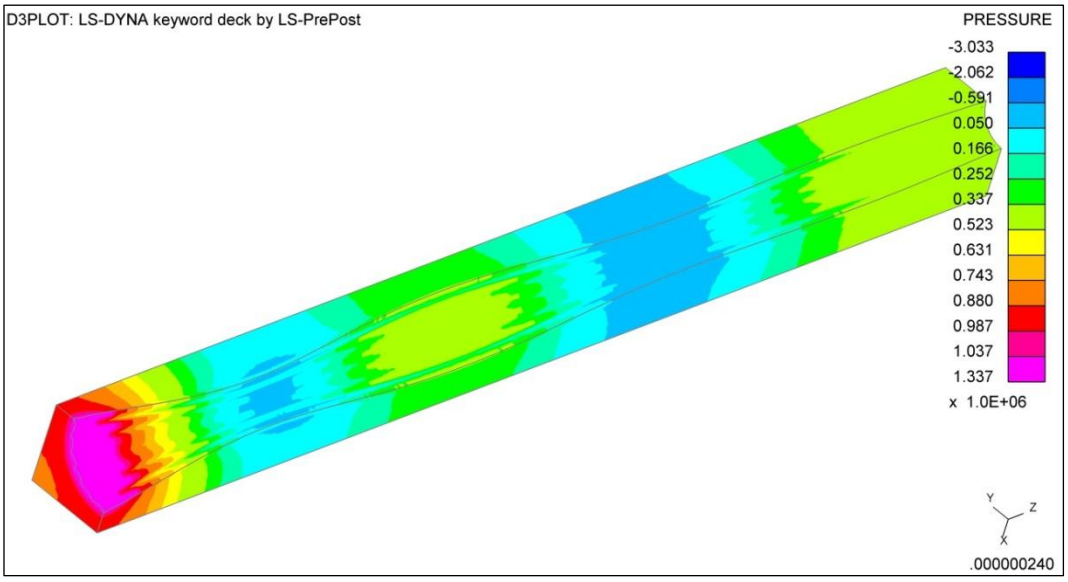

Figure 6.15 - Pressure distributions in the solid part at time t=2.4e-07 for input pressure of 10^7 Hz. The displacements are magnified 1000 times.

Impedance results reflect the same considerations done for the fluid geometries, that is to say when the wavelength of the signal become comparable with the dimensions, for example the diameter of the channel, it could be possible to see variations on the acoustic impedance values detected. Figure 6.16 and Figure 6.17 depict this consideration, with the greater differences in the real part chart, while the phase and the imaginary parts don't denote the same excursions. This because of the regularity of the domain.

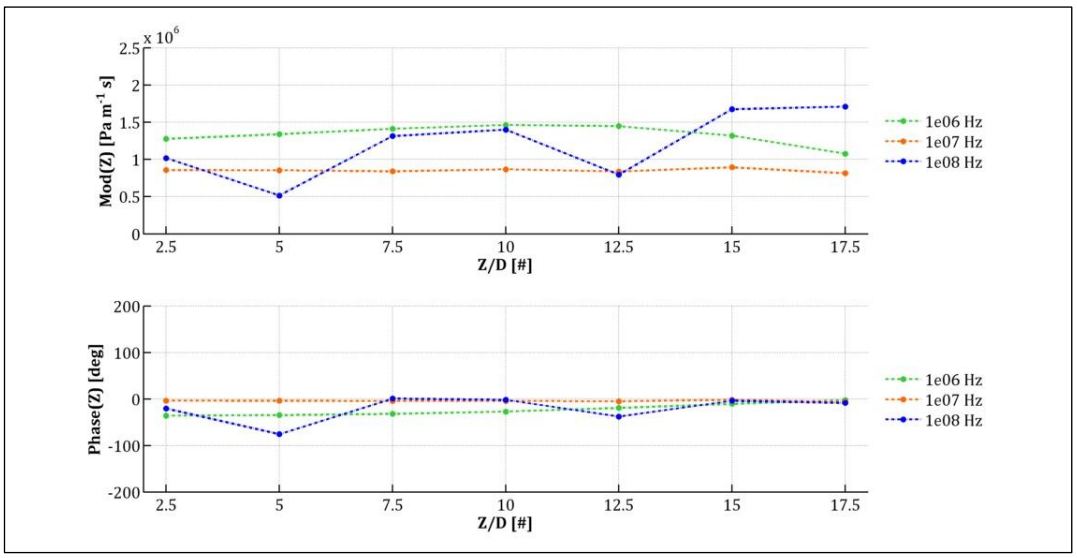

Figure 6.16 - Impedance Z modulus and phase for the straight tube FSI domain for every simulated frequency.

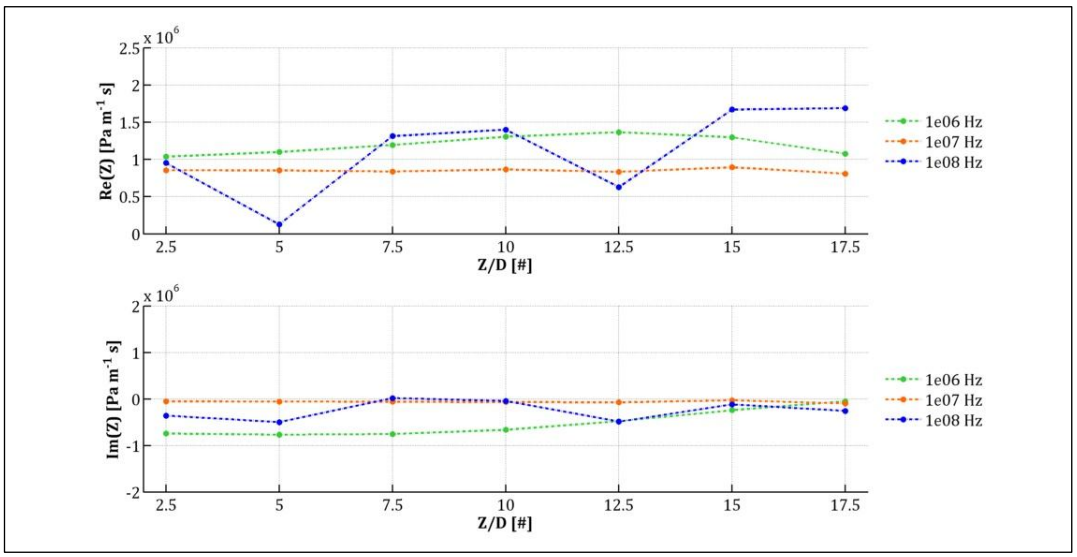

Figure 6.17 - Impedance Z real and imaginary parts for the straight tube FSI domain for every simulated frequency.

6.6.2 *Enlargement geometry*

Figure 6.18 and Figure 6.19 show the pressure and velocity results for the enlargement FSI geometry. Compared with the analogue pressure signal for the fluid geometry analysis in previous chapter (Figure 5.36) the trend is similar, except from what occurs in section z/D equal to 15. In fact, in the FSI analysis, pressure results smaller than the previous case, this might be because of the presence of the elastic boundary represented by the solid who takes part of the incoming pressure through transmitted waves. In the fluid case this was not possible because of the rigid body condition assumed around the fluid geometry.

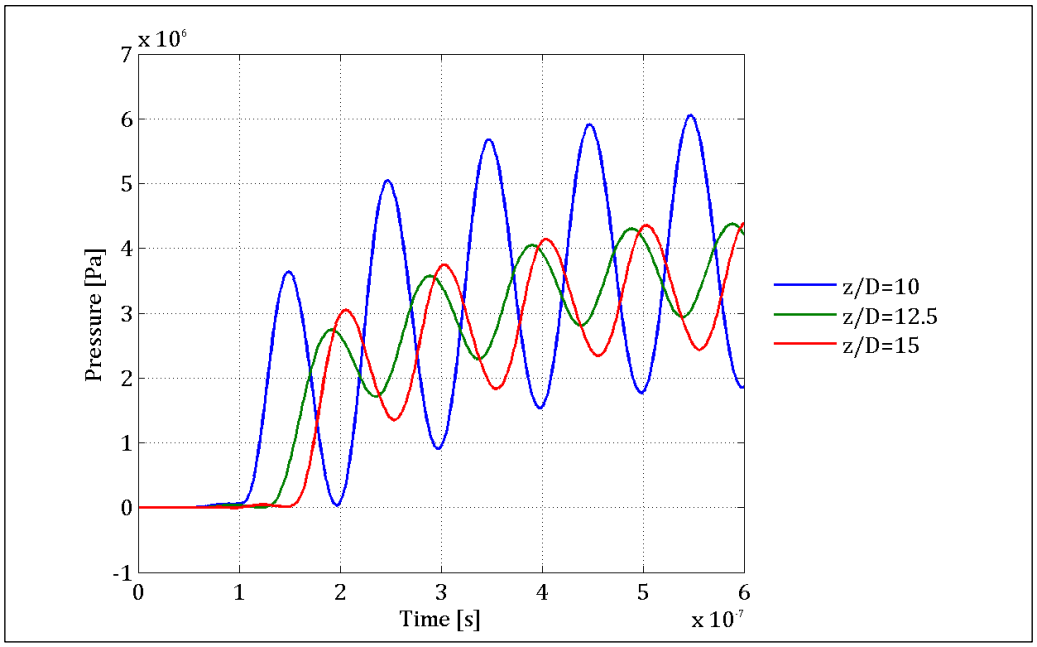

Figure 6.18 – Fluid pressure signals for the enlargement FSI geometry for an input pressure of 10^7 Hz.

In the velocity signal (Figure 6.19) is easily visible the effect of the conservation of mass: where the section area gets larger, the fluid velocity tends to decrease.

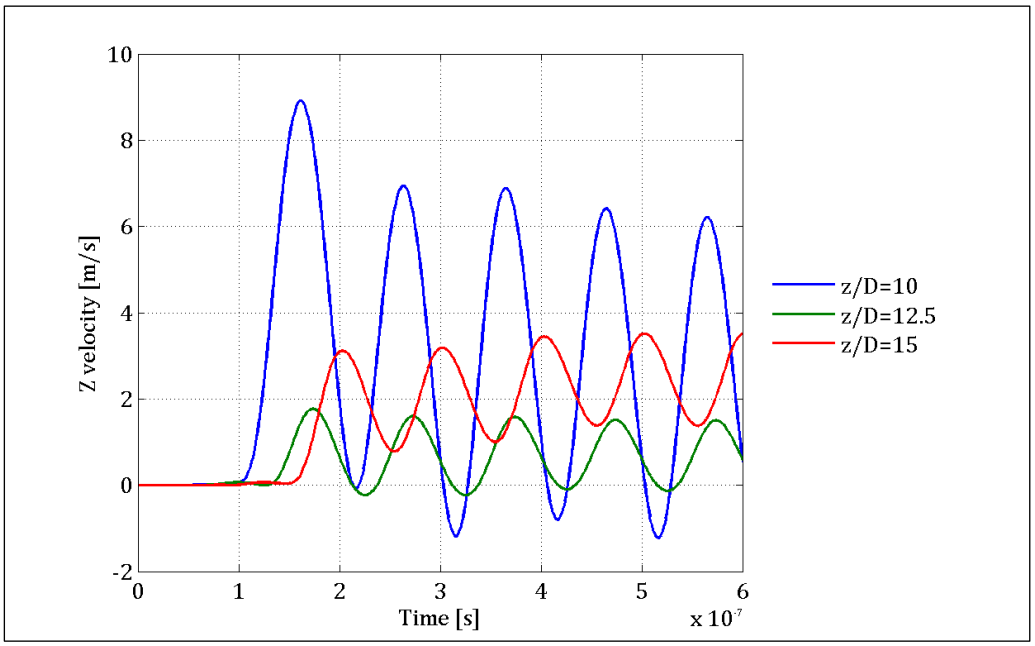

Figure 6.19 – Fluid velocity signals for the enlargement FSI geometry for an input pressure of 10^7 Hz.

Observing the impedance results, plotted for every monitored section and resumed in Figure 6.20 and Figure 6.21, an increasing of the stiffness reactance is easy to notice in section 12.5 z/D, in the middle of the singularity as already seen in the fluid analysis of the previous chapter. In this section frictions are smaller and so the real part tends to increase too, as expected.

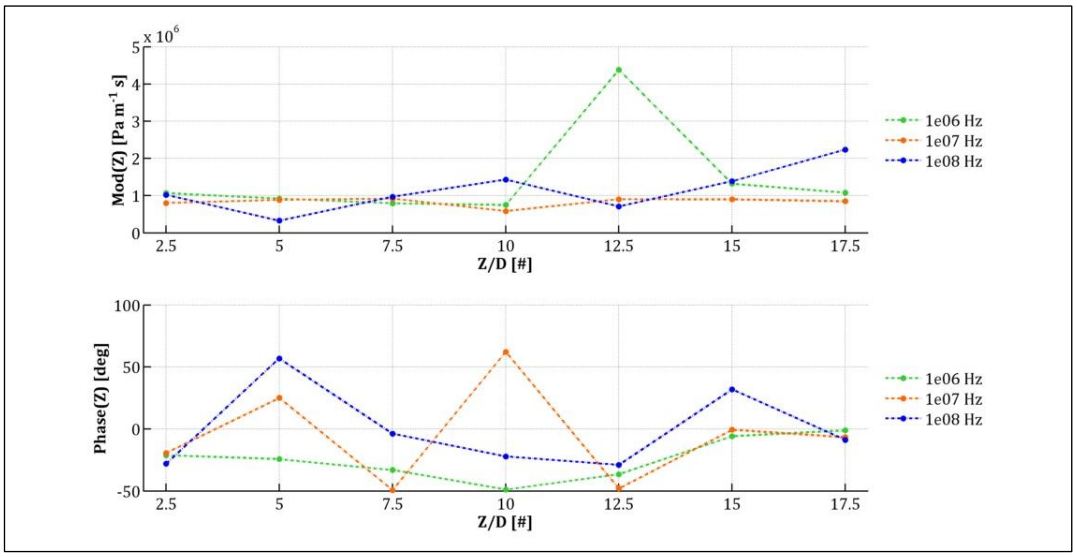

Figure 6.20 - Impedance Z modulus and phase for the enlargement FSI geometry for every simulated frequency.

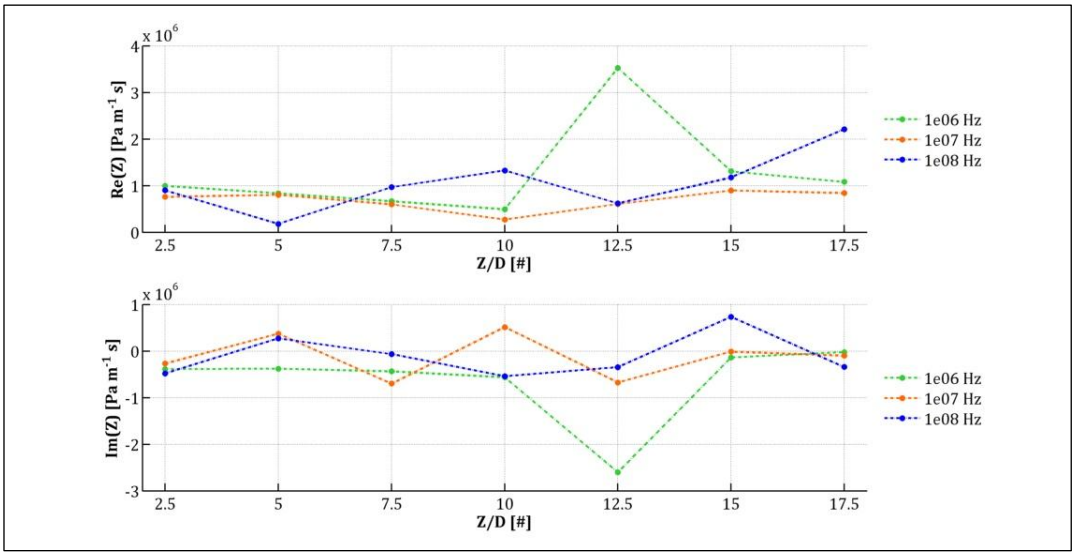

Figure 6.21 - Impedance Z real and imaginary parts for the enlargement FSI geometry for every simulated frequency.

6.6.3 *Constriction geometry*

Pressure and velocity signals (Figure 6.22, Figure 6.23) depict a significant reduction of the amplitudes after the singularity. Again, from the velocity signal, the results obtained in the middle of the singularity respect the conservation of mass, where the increment od velocity is due to the constriction od the cross section of the channel.

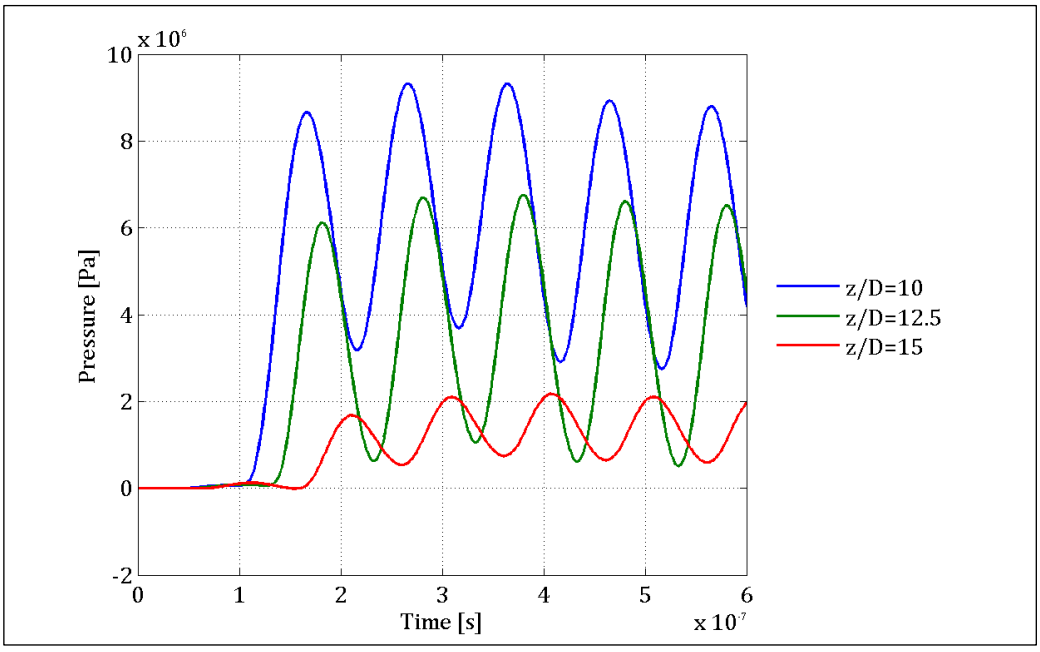

Figure 6.22 – Fluid pressure signals for the constriction FSI geometry for an input pressure of 10^7 Hz.

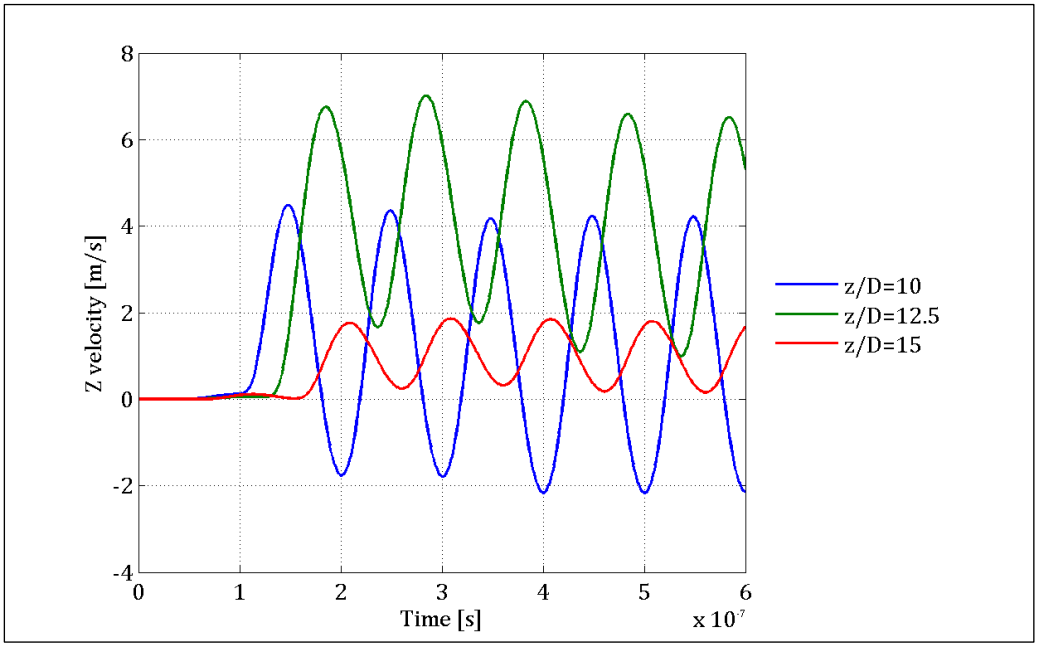

Figure 6.23 – Fluid velocity signals for the constriction FSI geometry for an input pressure of 10^7 Hz.

As seen in the fluid geometries analysis, the constriction example mirrors what happens in the respective enlargement domain studied in the previous paragraph (Figure 6.24, Figure 6.25).
Remembering the example of the Helmholtz resonator of paragraph 5.7.3.1, it can be seen the increment of the inertive part of the reactance denoted by the results of the imaginary part in section 12.5 z/D in the middle of the singularity. Conversely reactance is more stiffness dominated in section 10 z/D where the section is larger.

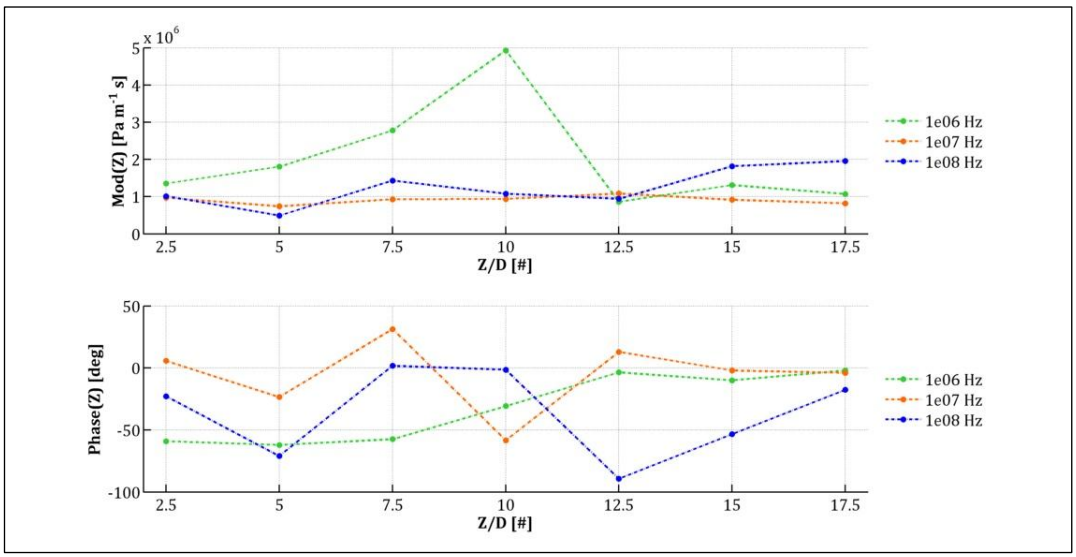

Figure 6.24 - Impedance Z modulus and phase for the constriction geometry for every simulated frequency.

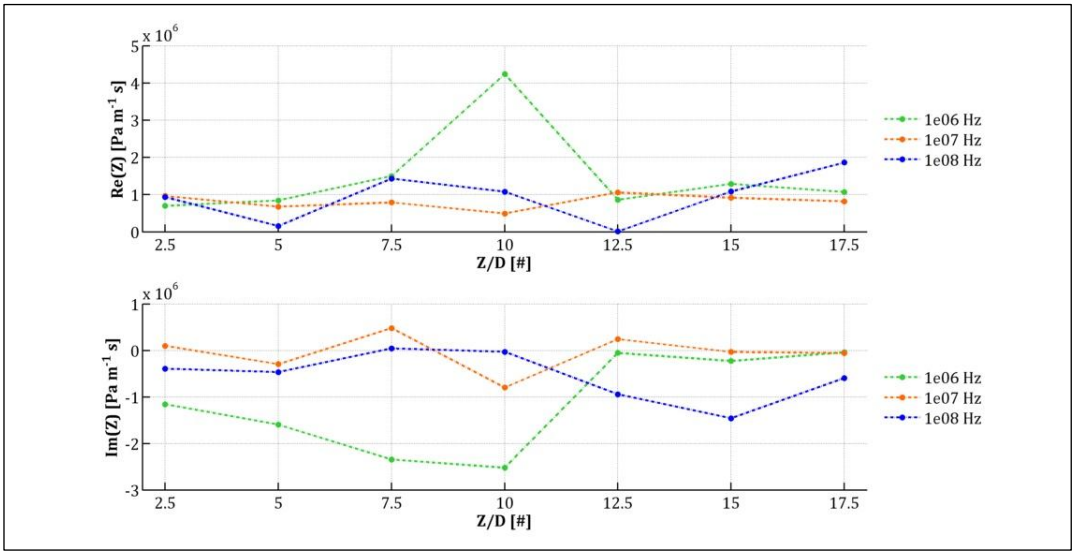

Figure 6.25 - Impedance Z real and imaginary part for the constriction geometry for every simulated frequency.

6.6.4 Results comparison

In this paragraph are resumed the results obtained for every simulated geometry grouped by input pressure frequency.
As seen in the fluid geometry analysis, here is still the diameter length the value who discriminates which wavelength is influenced by the considered domains in particular ways. In frequencies as 10^6 and 10^7 Hz (Figure 6.26, Figure 6.27, Figure 6.28, Figure 6.29), impedance results seem to follow the considerations carried out in the fluid geometry analysis, but a finer comparison between fluid and FSI simulations will be done in the next paragraph.
Correctly, the straight tube geometry does not present significant variations in phase, real and imaginary parts. Conversely the great variations are visible in the other two geometries, and their results mostly follows opposite trends, because of their singularities.

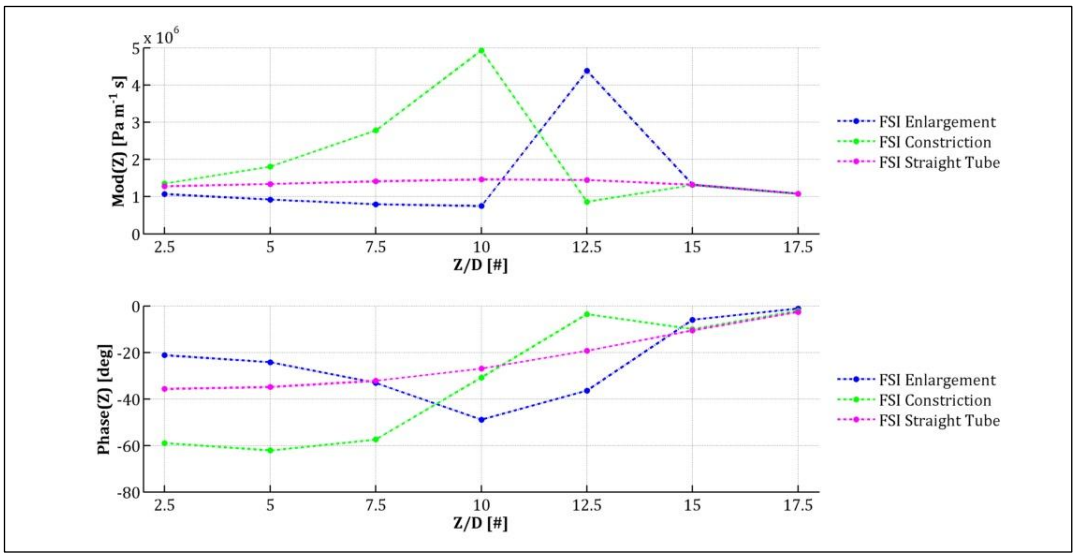

Figure 6.26 - Impedance modulus and phase in the spatial non-dimensional domain for every simulated FSI geometry for an input frequency of 10^6 Hz.

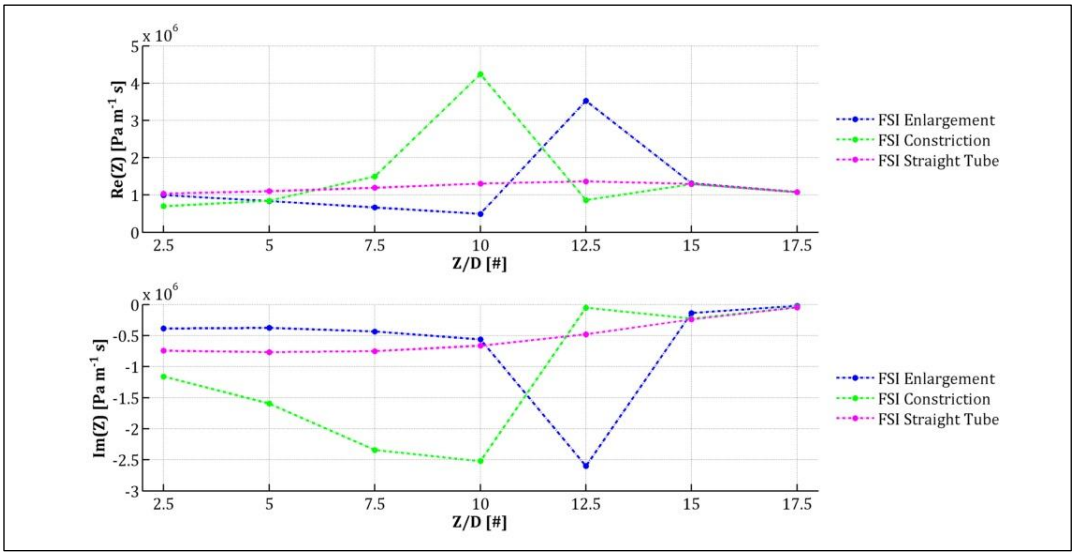

Figure 6.27 - Impedance real and imaginary parts in the spatial non-dimensional domain for every simulated FSI geometry for an input frequency of 10^6 Hz.

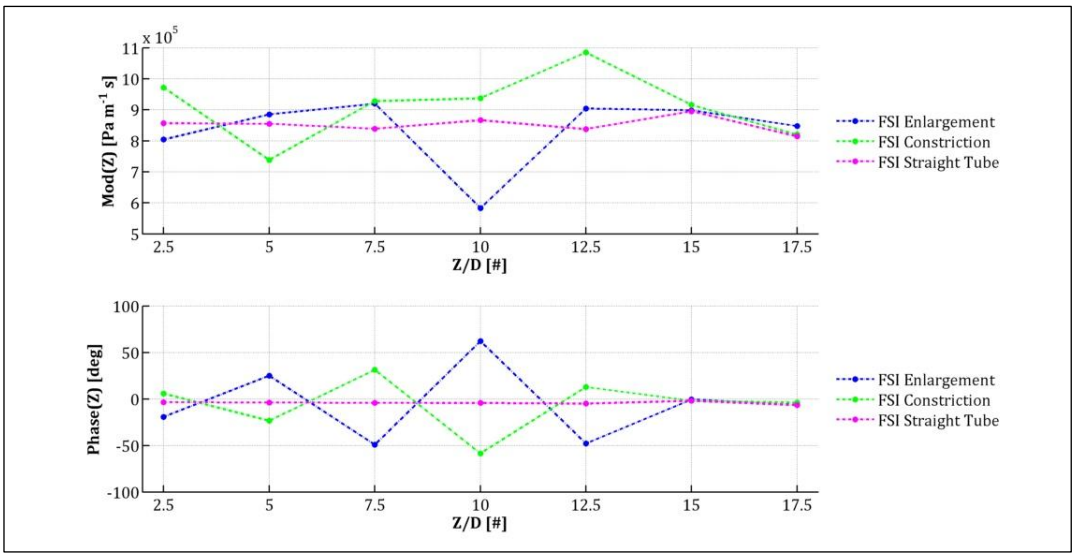

Figure 6.28 - Impedance modulus and phase in the spatial non-dimensional domain for every simulated FSI geometry for an input frequency of 10^7 Hz.

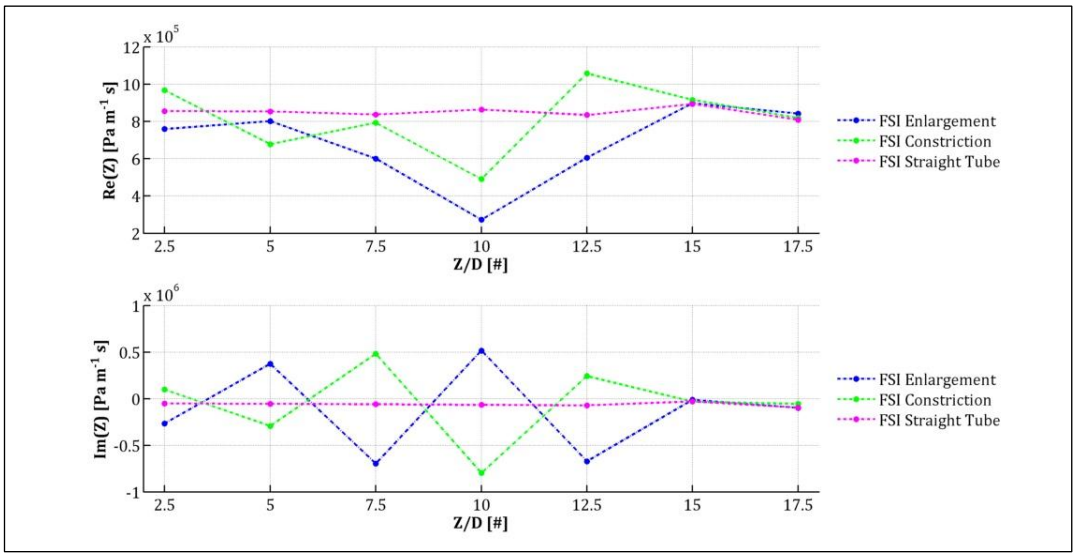

Figure 6.29 - Impedance real and imaginary parts in the spatial non-dimensional domain for every simulated FSI geometry for an input frequency of 10^7 Hz.

The explication of this phenomenon lies in the pressure and velocity fields along the domain for those two FSI geometries (Figure 6.30, Figure 6.31). For example, the pressure field immediately before the constriction presents higher values than the enlargement, but the velocity field acts in the opposite way. that's why for example real part is higher in 7.5 and 10 z/D in the constriction geometry than in the enlargement (more pressure with less velocity means better signal energy conservation and then higher real part).
From Figure 6.30 and Figure 6.31 it is easy to appreciate the meaning of the development of engineering technologies as borehole acoustic imaging systems. This figures are an example of how a signal is reflected from the singularity encountered, and resent backward to a point where, with special sensors, the geology nearby the system can be reconstructed through the time of incoming and the amplitude of this reflected wave.

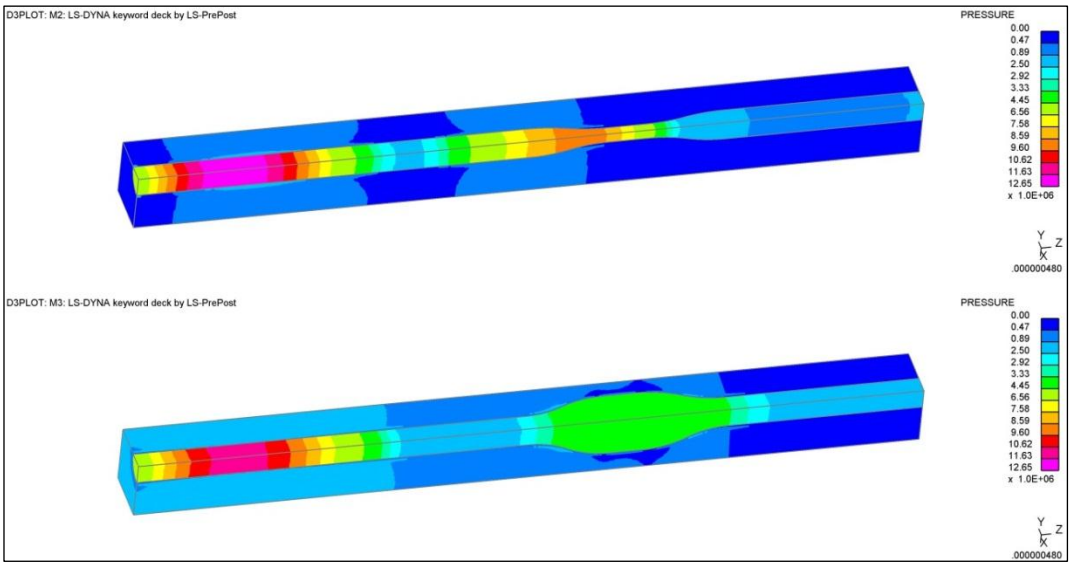

Figure 6.30 - Pressure spatial distributions in enlargement and constriction FSI domains at time t=4.8e-07s for an input frequency of 10^7 Hz.

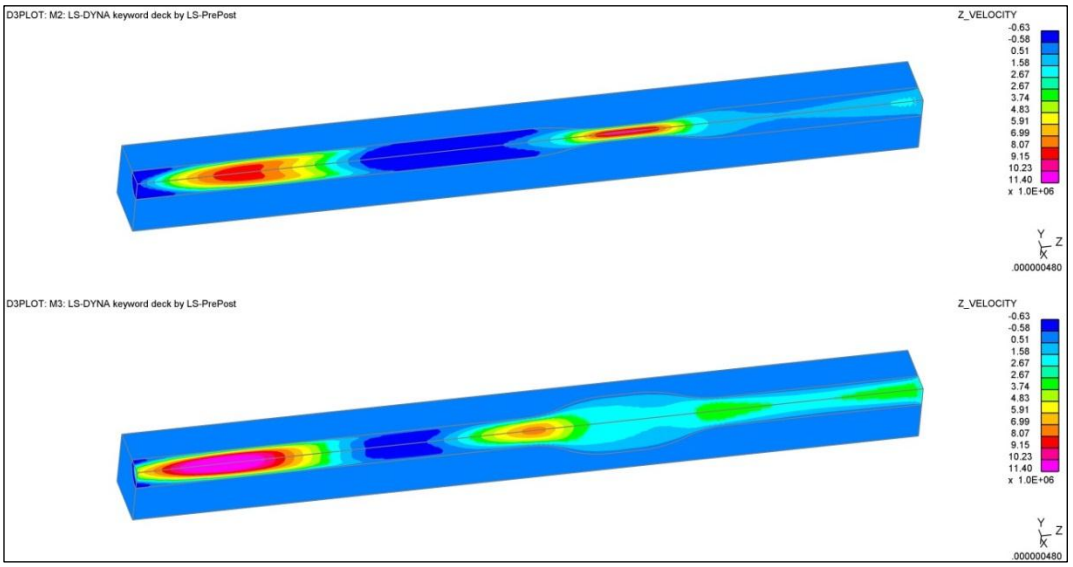

Figure 6.31 - Velocity spatial distributions in enlargement and constriction FSI domains at time t=4.8e-07s for an input frequency of 10^7 Hz.

Results for an input frequency of 10^8 Hz are more difficult to interpret, but some considerations can still be performed. For example trends of the modulus and real part of the impedance are similar for every considered geometry, this is probably because the short wavelength is too short to notice the singularities imposed.
Differences in phase and imaginary part by the way can be observed in sections before the singularities. Reflections from the enlargement causes reflected waves with opposite phase with respect to the other geometries.

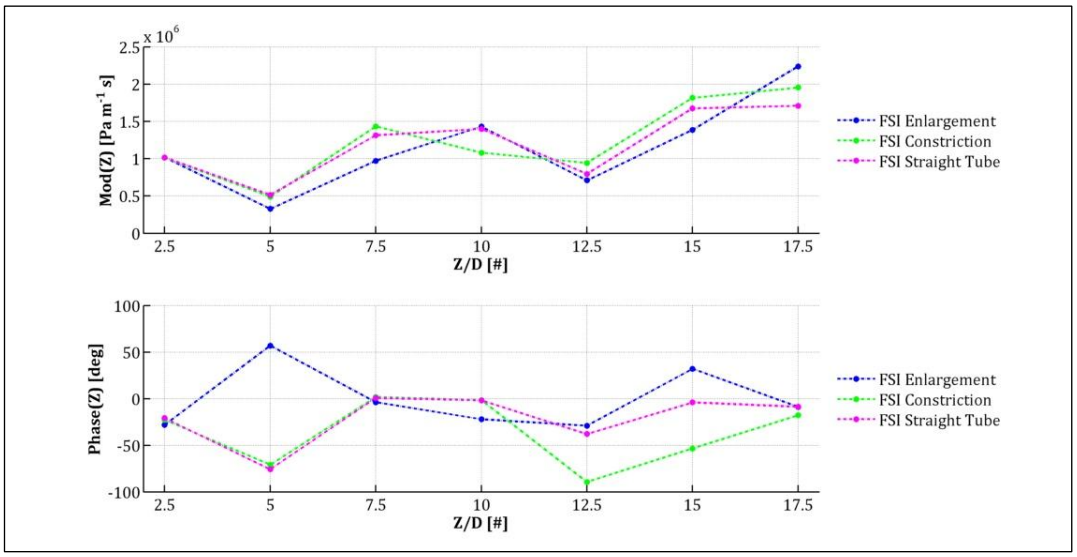

Figure 6.32 - Impedance modulus and phase in the spatial non-dimensional domain for every simulated FSI geometry for an input frequency of 10^8 Hz.

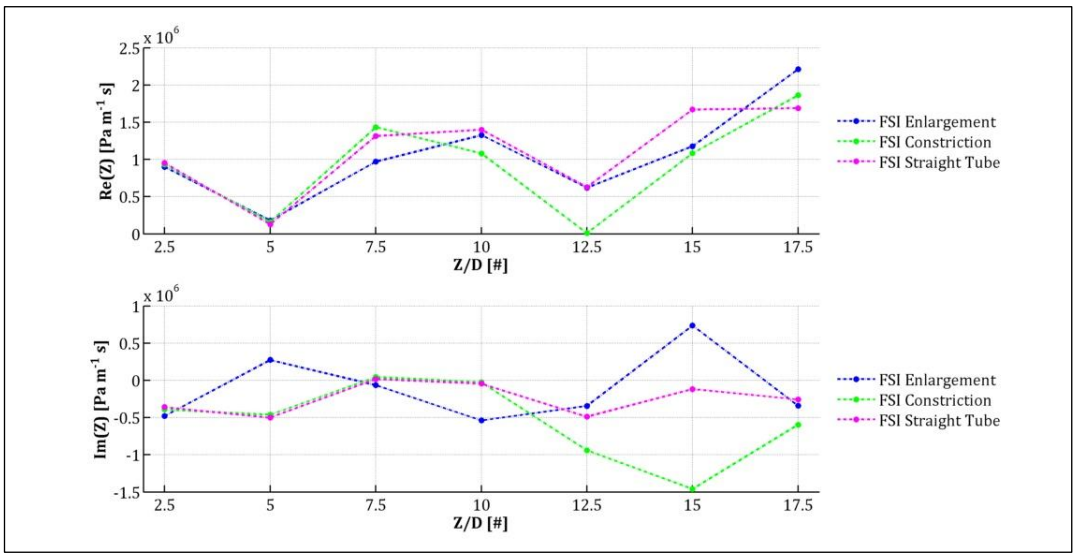

Figure 6.33 - Impedance real and imaginary parts in the spatial non-dimensional domain for every simulated FSI geometry for an input frequency of 10^8 Hz.

6.6.5 *Fluid analysis and FSI analysis results comparison*

As a conclusion of the fluid-structure interaction analysis, another important comparison has been performed: for each geometry simulated (straight tube, enlargement and constriction) results of the fluid analysis, with a rigid constraint around the fluid domain, and results of the FSI analysis, with an elastic body surrounding the fluid channel, are gathered in a chart for a better understanding of the effect of the interaction between fluid phase and solid matrix.
The first thing noticed from every geometry results is that the main trends seem to follow what was expected, a decrease of the values of impedance for the FSI simulations which have a compliant solid boundary. In fact, in a fluid surrounded by a rigid body, the pressure wave reflects on the boundaries maintaining into the domain the energy introduced, and pressure losses are only due to viscosity effects. In a domain with an elastic interaction between solid an fluid those waves incident to the external fluid boundaries are only partially reflected in the fluid domain, and the difference in transmitted to the solid domain which spreads it as stress waves travelling, in our case, at twice the phase velocity of the fluid. The elastic nature of the solid simulated do not imply that the solid is dissipative, but in this analysis is only a mean to subtract energy from the fluid and transport it in other parts of the domain. The way in which waves travels in the solid matrix, and the factors they are influenced by, are explained in the next chapter.

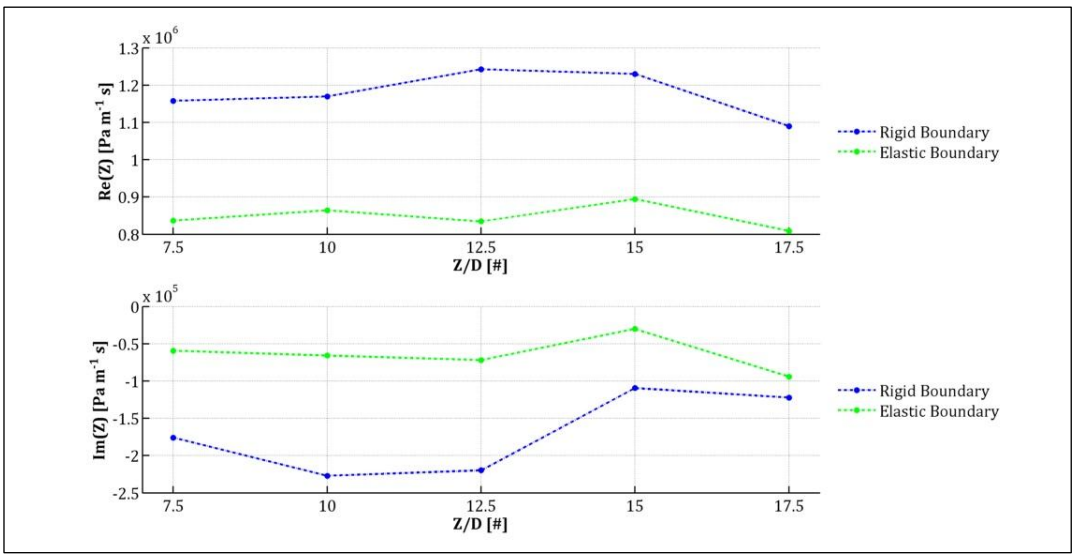

Figure 6.34 - Real and imaginary parts of the impedance Z for the straight tube fluid (rigid boundary) and FSI (elastic boundary) domains, for an input pressure wave frequency of 10^7 Hz.

Reduction in real part, the factor which resumed the amount of energy transported, as shown in the relation (3.8), is an average of 15%. This value spreads far from the sections nearby the singularities, and reduces in correspondence with them, as it can be seen in figures Figure 6.35 and Figure 6.36 reporting the results for the enlargement and the constriction geometries. Results presents similar behaviors also with input frequency 10^6 Hz, while those trends are not respected for the 10^8 Hz input frequency.

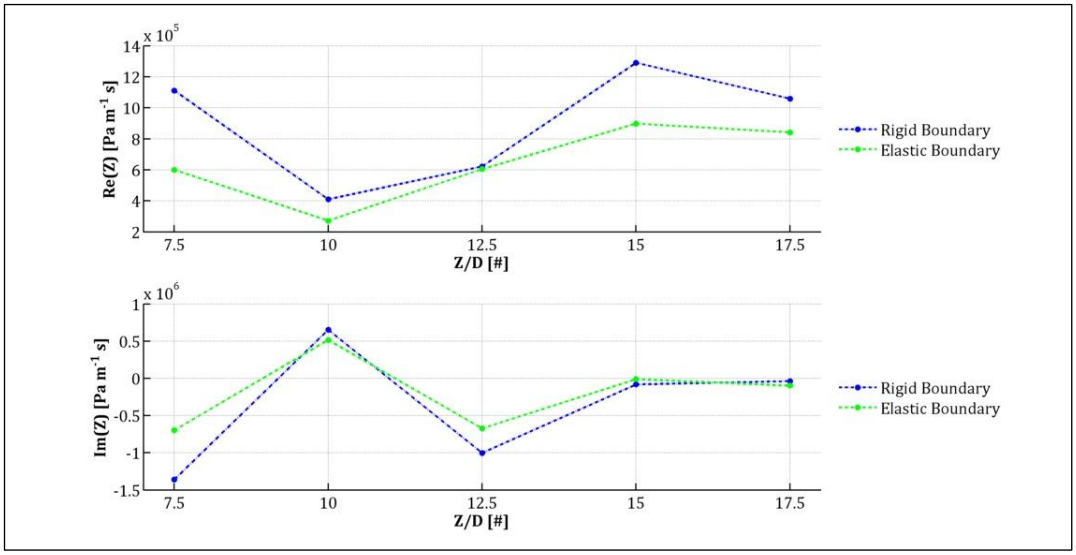

Figure 6.35 - Real and imaginary parts of the impedance Z for the enlargement fluid (rigid boundary) and FSI (elastic boundary) domains, for an input pressure wave frequency of 10^7 Hz.

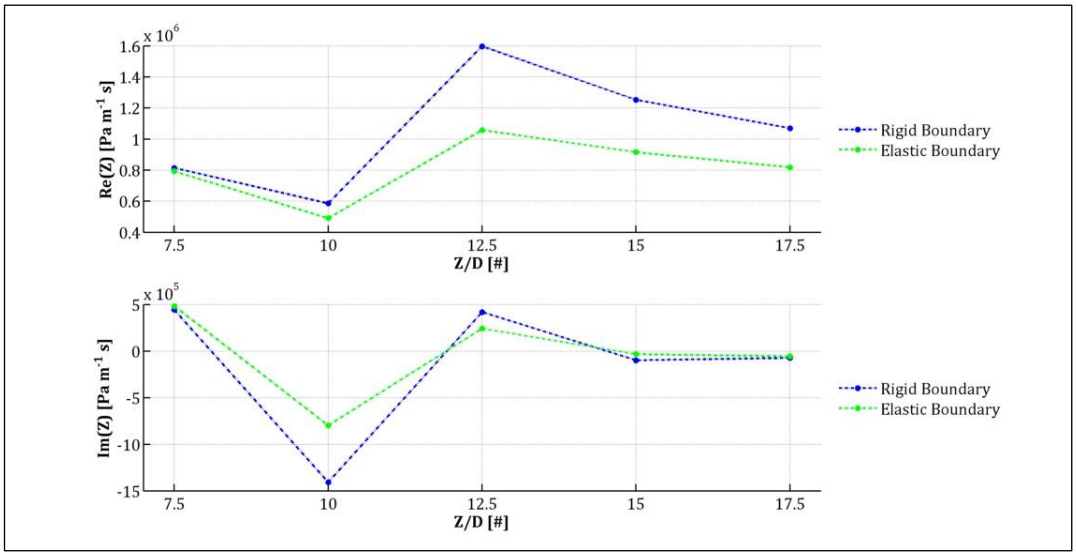

Figure 6.36 - Real and imaginary parts of the impedance Z for the constriction fluid (rigid boundary) and FSI (elastic boundary) domains, for an input pressure wave frequency of 10^7 Hz.

7 A further evaluation: boundary conditions for the solid structure

7.1 Overview of the problem

From the point of view of adding complexities to the simple starting standalone fluid problem, to perform a correct fluid-structure interaction both solid and fluid phase have to be stressed with the same pressure inlet wave. In order to simulate only a very small representative part of the real extended porous soil, the rock domain has to be constrained in a way that the results have to be comparable to those obtainable with the real physics in nature.
With the aim to achieve the better constraint conditions some combinations of boundary conditions have been performed.
The choice of the constraints had to take into account multiple factors that could be influenced by the different boundary conditions superimposed. Since symmetry conditions have been adopted for all the xz and yz plane boundary surfaces, the solid domain could move only in the z direction of the longitudinal axis of the system. Constraining this translational degree of freedom would cause, however, reaction forces not correlated with the real nature phenomenon or generate stresses due to reflections on the constraints of the perturbations travelling in the considered domains.
That's why an analysis has to be done on this important aspect.

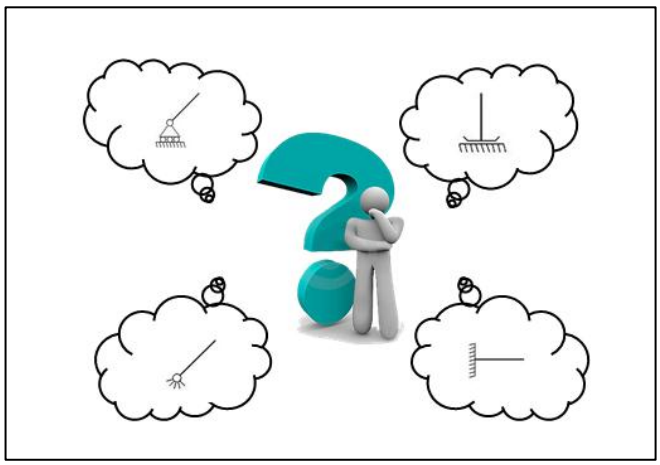

Figure 7.1 - What is the better constraint condition?

7.2 FSI geometry

With the aim of analyzing the single effect of the z-translational constraint on the input solid interface, a simple domain has been created modeling a square sectioned solid perforated by a circular cross section cylindrical channel fully filled with fluid. In order to decrease the simulation times, a quarter of this domain has been simulated, with applying symmetry conditions on the appropriate surfaces. This model has the same fluid channel diameter D of the previous domains used for FSI simulations, equal to 10 μm, and their same length, that is to say 20 times the diameter D. The minimum solid thickness has been reduced to 3 μm, remaining in the same magnitude order of the diameter.

7.3 Analyzed constraints for solid surfaces

For every surface lying on plane parallel to the xz or yz plane, symmetry conditions have been imposed.
Furthermore, considering the shape of the cross section of the chosen domain, three main constraint conditions for the z-axis longitudinal translation might be possible to apply to the solid input surface to evaluate individually their effects on the solution: fixing all the surface nodes (Figure 7.2), fixing the nodes of the two external edges of this surface (Figure 7.3) and fixing only the external corner this surface (Figure 7.4).

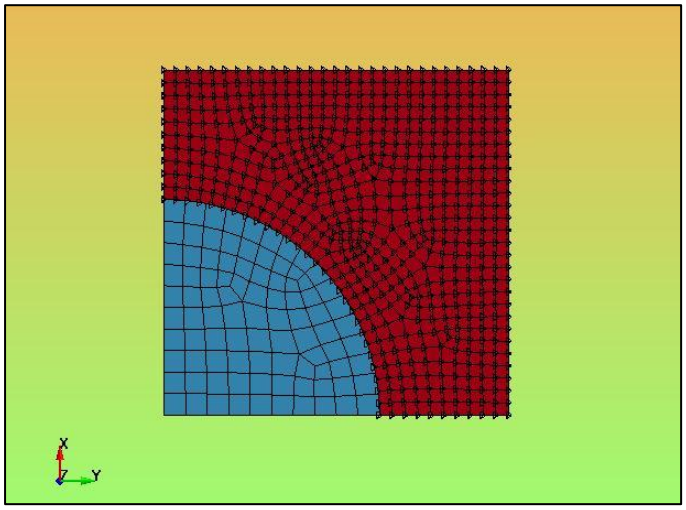

Figure 7.2 – All solid surface nodes constrained in the z-axis translational degree of freedom.

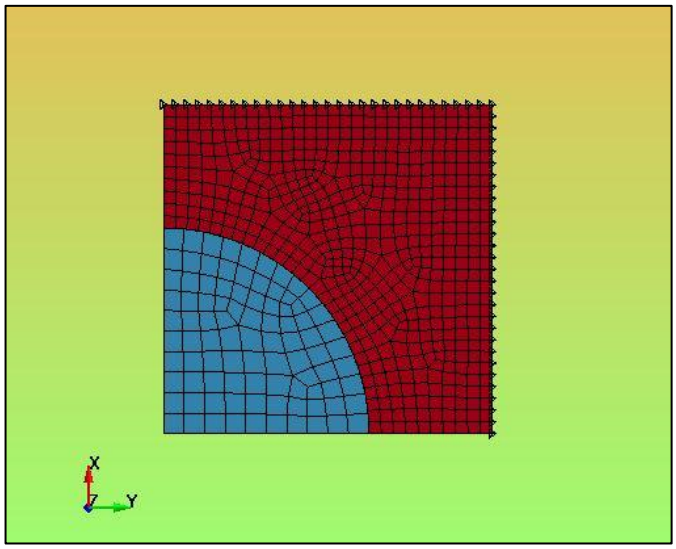

Figure 7.3 – External solid edges nodes constrained in the z-axis translational degree of freedom.

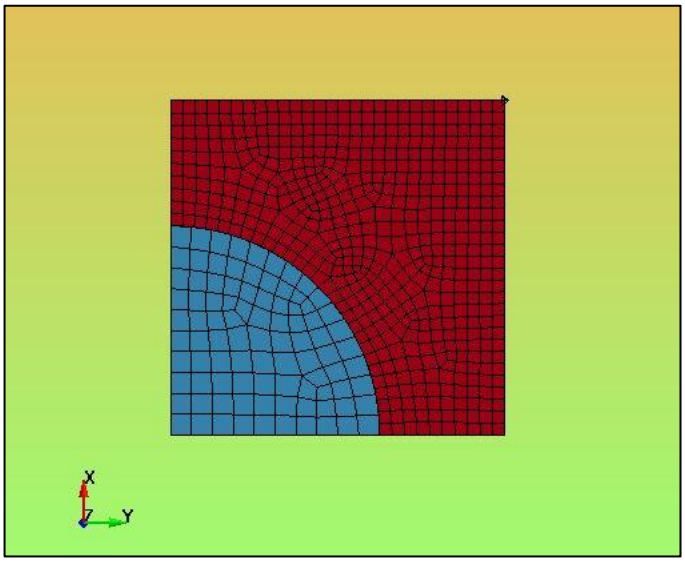

Figure 7.4 – External solid corner node constrained in the z-axis translational degree of freedom.

7.4 Mesh implementation

To concentrate on the fluid-structure interaction and the effects that the boundary conditions have on the solution, a finer mesh than the previous FSI simulations has been created. Elements and nodes increased in number (Table 7.1), but to decrease the simulation duration and sure to obtain a good interaction, the solid minimum thickness has been reduced to 3 μm.

	Straight Tube
Solid Elements	365700
Solid Nodes	402853
Fluid Elements	36400
Fluid Nodes	44110

Table 7.1 – FSI meshes for constraints test main characteristics.

7.5 Simulation times

Integration and saving timesteps remained the same than the previous chapter FSI simulations, and also the simulated time didn't change (Table 7.2).

	1.00E+07
dt of integration	1.00E-11
dt of saving	1.00E-09
Sim. time	6.00E+07
Average sim. duration	2h

Table 7.2 – FSI constraints test simulation times.

7.6 Results

Results for those simulations have been grouped for typology of z-translational constraint and then compared as a final analysis. For each calculation data has been collected for solid and fluid phases for sections every 2.5 diameters in the z longitudinal direction starting from the inlet section.
Since a fluid-structure interaction occurs in this models, the consequences of the imposition of a specific constraint have to be found in both fluid and solid results. That's the reason why the further analysis has been conducted having a look primarily to the pressure and velocity signals in the fluid phase, and then to the z-component of the resultant stress on each inspected section. After that some considerations have been made on the FFT of the fluid signals, to analyze the different effects on the acoustic impedance of the different examined boundary conditions.

7.6.1 Inlet solid surface constrained

Locking the all inlet surface nodes, the same solution analyzed in paragraph 6.6.1 is obtained, proving that the different meshes do not affect significantly the results.
It's easily visible in the first part of both pressure (Figure 7.5) and velocity (Figure 7.6) signals, plotted for sections after 5, 10 and 15 z/D non-dimensional distance from the inlet sections for a clearer view, the effect of the so called precursor wave travelling in the solid domain but acting on the fluid phase.

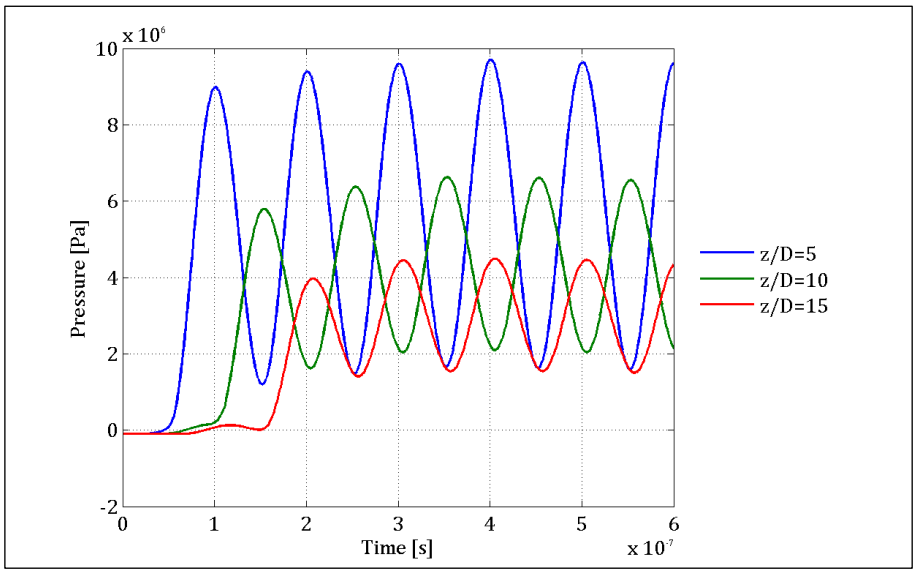

Figure 7.5 – Fluid pressure signal for inlet solid surface constrained model.

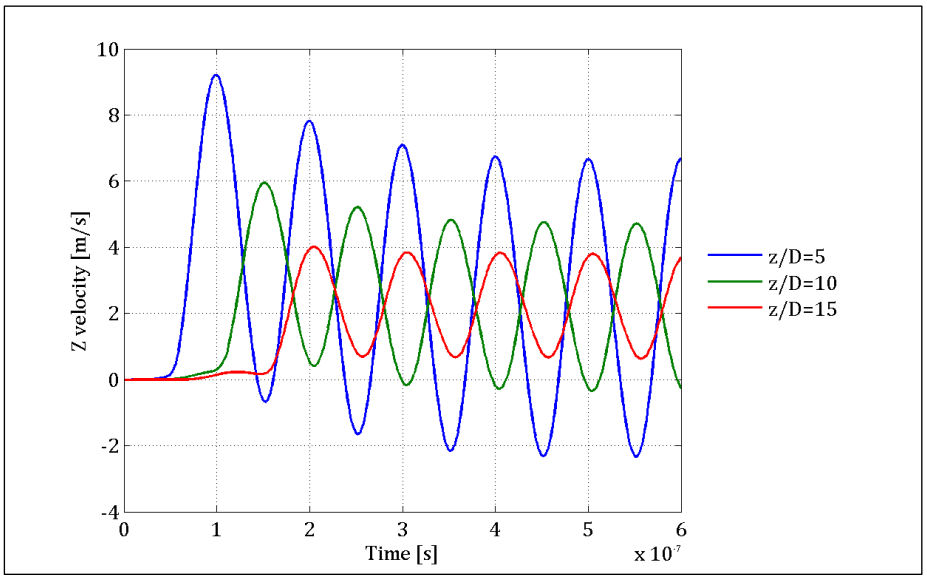

Figure 7.6 – Fluid velocity signal for inlet solid surface constrained model.

For what concerns the solid part, the z-component of the resultant stress on a section with the z-axis as normal has been extracted. This component travels, as already seen from the FSI simulations of the previous chapter, with almost twice the phase velocity of the waves travelling in the fluid part, causing the appearance of a precursor wave acting from the solid to the fluid domain. In Figure 7.7 is represented the variation with time of this stress component for every monitored section. This representation has been chosen to underline a phenomenon important for the comprehension of the effect of the constraint on the entire structure. In fact, looking at the peaks of every oscillation, it is easily observable that their value for every section seems to be ruled by another harmonic oscillation, causing, for example, the amplitude of the signal at 7,5 z/D to be higher than the other ones after a single input pressure oscillation. This effect is explicable taking into consideration the reflected waves from the inlet surface, in particular from the constraints of this surface. The amplitude of this reaction waves, which travel in the solid matrix too, has to be summed to wavelets already travelling in the solid medium, varying peaks amplitude and generating this phenomenon. A better understanding of this event will surely come after a comparison of those force signals between different constraints conditions carried out in paragraph 7.6.4.

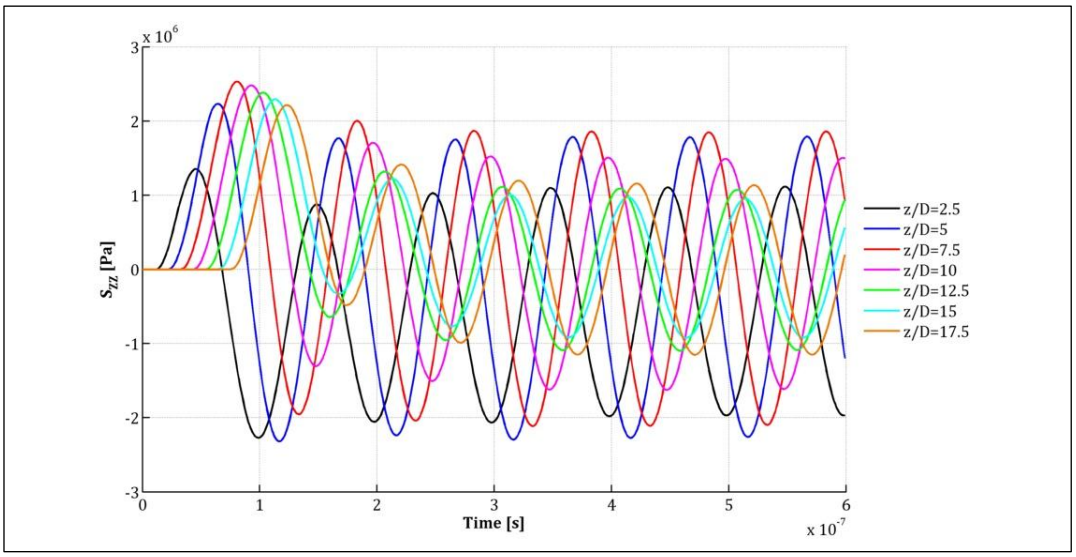

Figure 7.7 - Z-component of the resultant stress in every monitored section for the case of inlet solid surface completely constrained.

7.6.2 External edges constrained

Referring to Figure 7.5 and Figure 7.6, fixing the analysis on the precursor wave, it occurs that with this type of constraint its amplitude is bigger (Figure 7.8, Figure 7.9). This happens because the edge constraint, with respect to the total inlet surface one, makes the solid wave travel also into the solid part with the input wave amplitude. Resuming, this precursor wave is the sum of the inlet solid wave contribution and the wave generated by the expansion of the fluid channel (which was the only contribution in the solid phase constraining the all inlet solid surface).

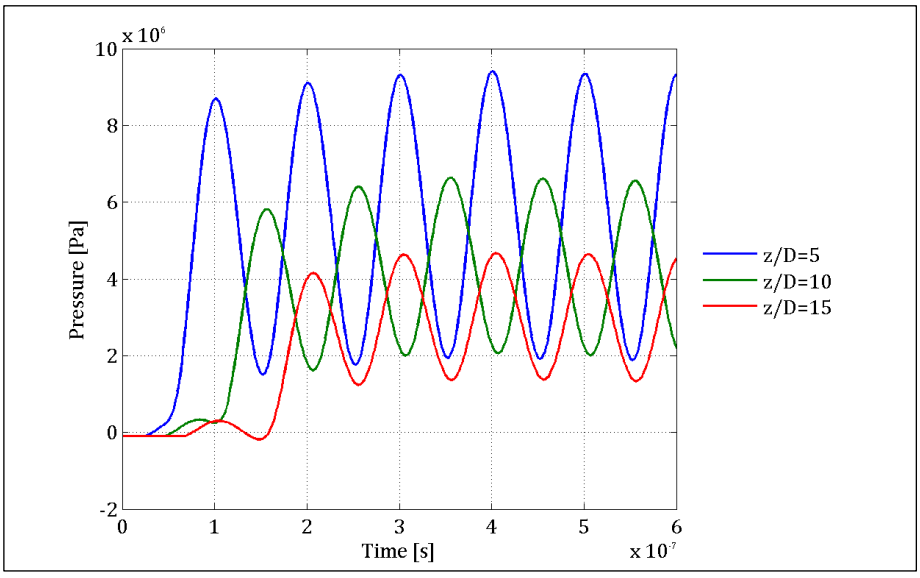

Figure 7.8 – Fluid pressure signal for the model with external edges of the inlet solid surface constrained.

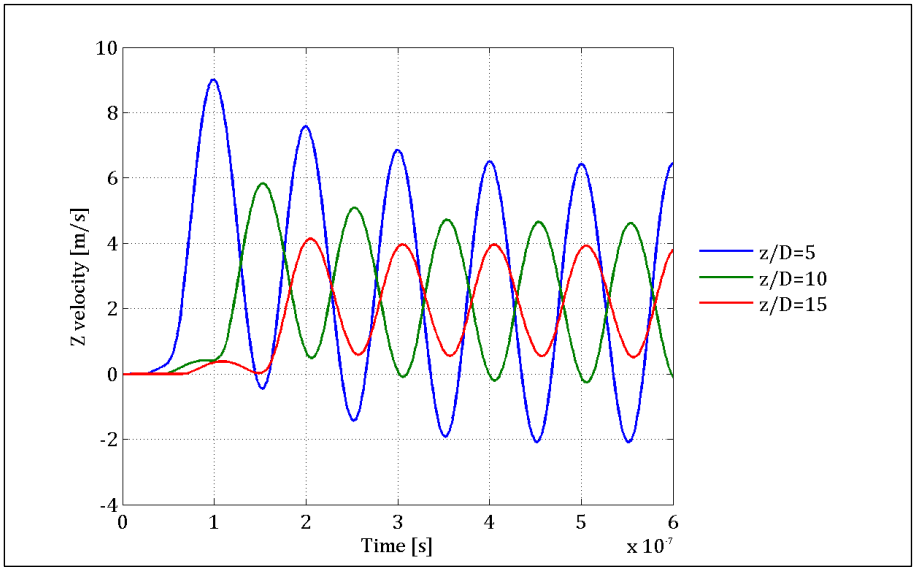

Figure 7.9 – Fluid velocity signal for the model with external edges of the inlet solid surface constrained.

Following the analysis made in the previous paragraph for the model with the entire inlet solid surface constrained, it can be stated, observing Figure 7.10, that for this combination of boundary conditions the maximum of the peaks is displayed after 5 z/D from the inlet solid surface, while in the previous configuration it was reached after 7,5 z/D. This is probably due to the increasing of the z-stress component amplitude caused by the different constraint and to its reaction stresses.

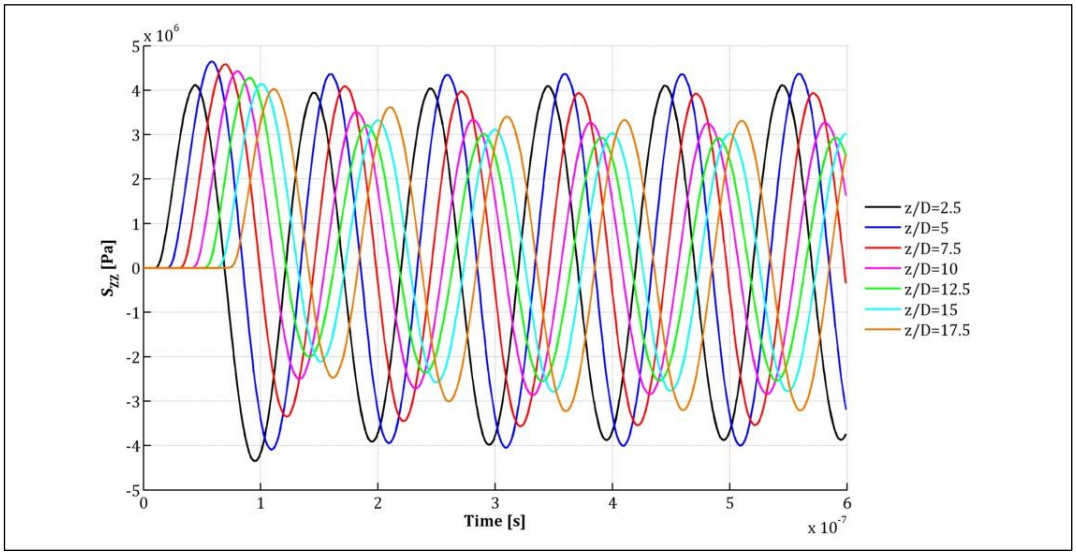

Figure 7.10 - Z-component of the resultant stress in every monitored section for the case of external edges of the inlet solid surface constrained.

7.6.3 External corner constrained

Reducing again the number of constrained nodes of the inlet section the solid input pressure is better transmitted to the structure, that's why the amplitude of the precursor wave increases compared with the other constraint conditions. This can be seen both from pressure and velocity signals for the fluid phase (Figure 7.11, Figure 7.12).

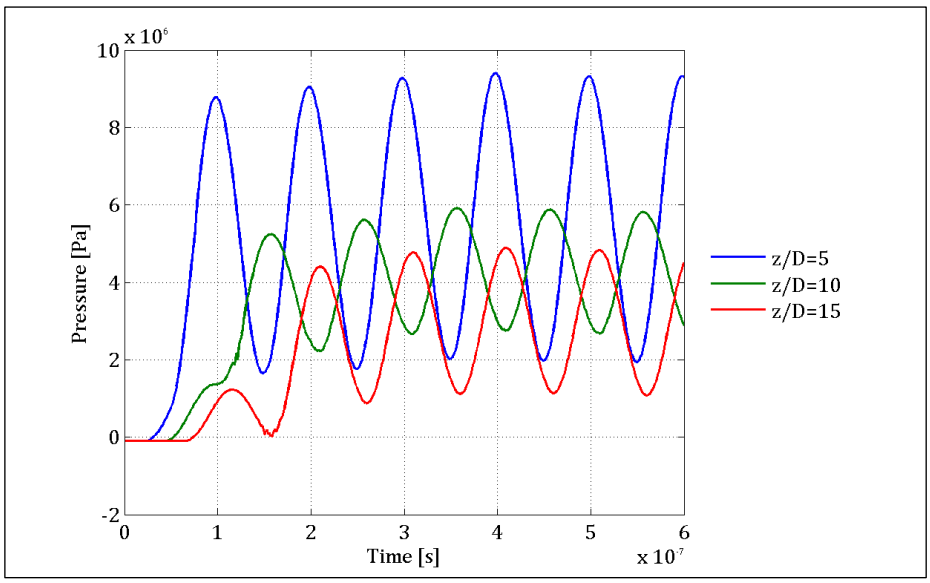

Figure 7.11 – Fluid pressure signal for the model with external corner of the inlet solid surface constrained.

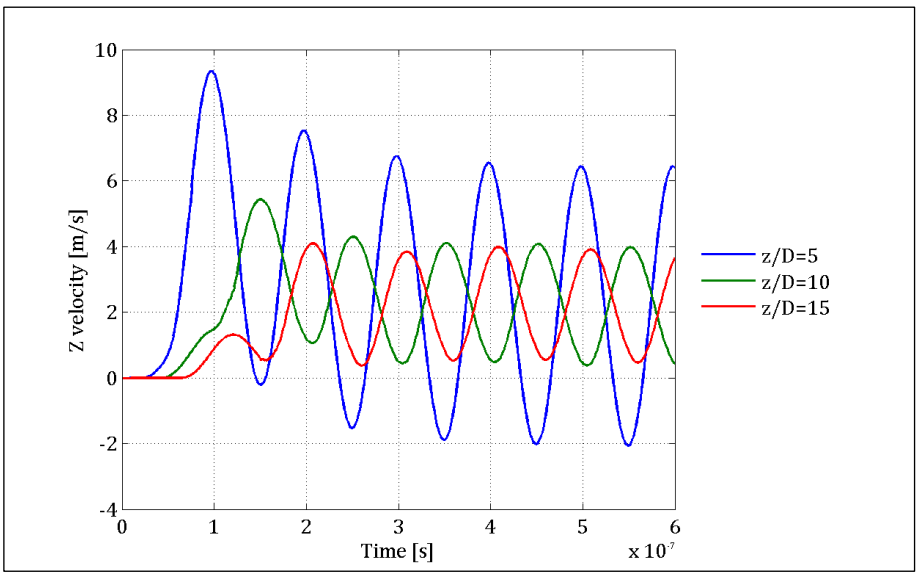

Figure 7.12 – Fluid velocity signal for the model with external corner of the inlet solid surface constrained.

Observing Figure 7.13, it is remarkable the strong increasing of the z-stress amplitudes, which are almost twice those emerged with the previous constraint

condition. The peak by the way is still present for each oscillation after 5 z/D from the inlet solid surface.

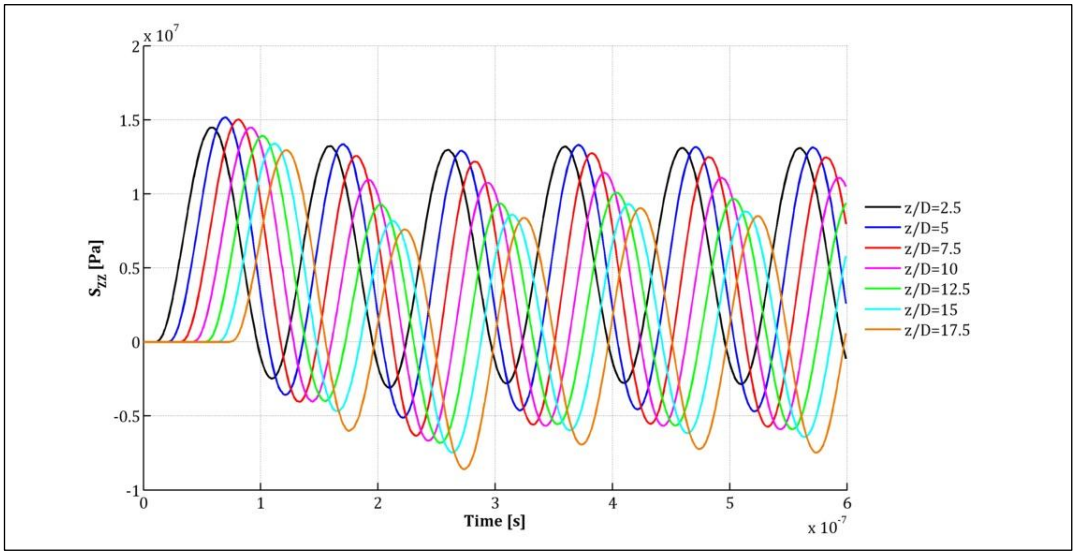

Figure 7.13 - Z-component of the resultant stress in every monitored section for the case of external corner of the inlet solid surface constrained.

7.6.4 Different constraints comparison

Analyzing the z-stress signals, for each examined section, the oscillations tend to stabilize around a mean value only after a transitional phase. This is due to the dissipative, viscous, nature of the fluid with which the solid interacts and acts as a dumper who stabilize its effect in time.
Furthermore, in the previous paragraphs, a variation of the pressure and velocity signals due to the different precursor waves affecting the fluid motion by the interaction with the fluid has been detected. A much stronger variation has been observed also in the z-stress signals, where not only the amplitudes have been influenced but even the shapes of the oscillations, detecting the effect of the reflected waves on the inlet constraints.
This would lead to the conclusion that those three constraints conditions conduce to three different structural reaction, and so the best way is to look for the boundary conditions that best fit the real solution.
Conversely, examining Figure 7.14 and Figure 7.15, those macroscopic differences can't be found in the charts of the real and imaginary parts of the acoustic impedance.

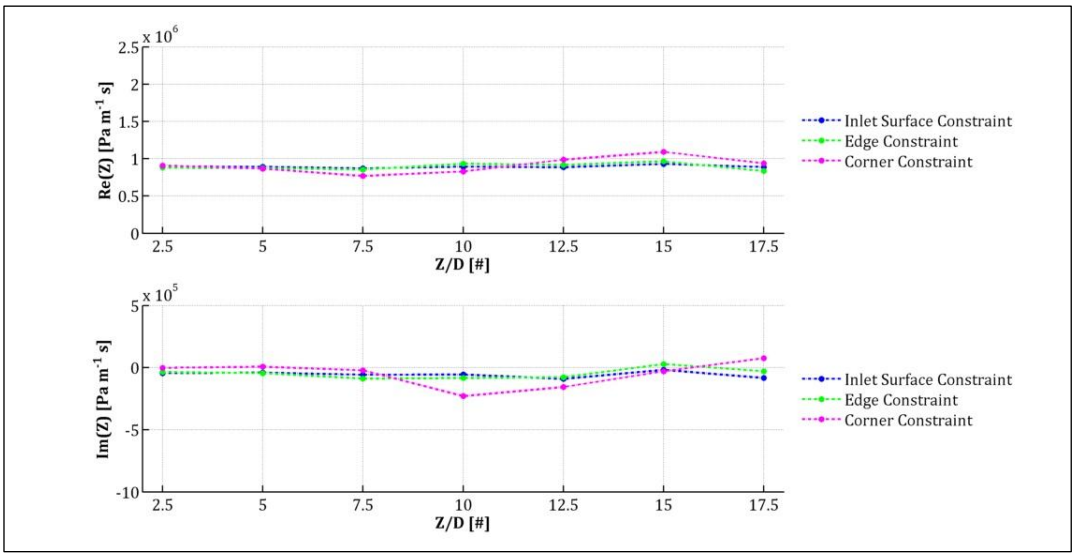

Figure 7.14 - Real and imaginary parts of the acoustic impedance Z for the fluid domain varying in space along the inspected model sections for every constraints condition examined for input frequency of 10^7 Hz.

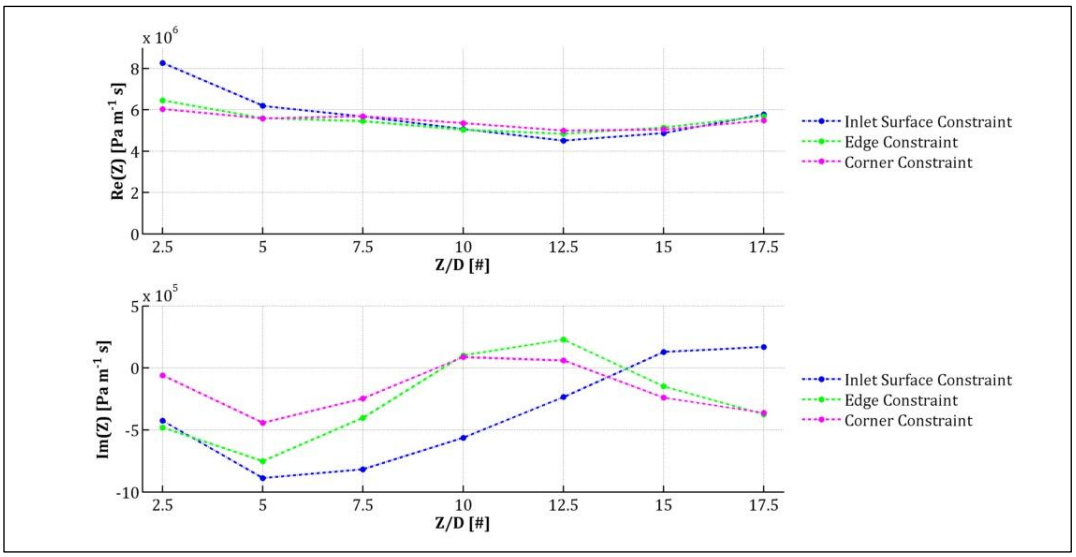

Figure 7.15 - Real and imaginary parts of the acoustic impedance Z for the solid domain varying in space along the inspected model sections for every constraints condition examined for input frequency of 10^7 Hz.

This because, accordingly to the meaning of acoustic impedance, there are no remarkable variations of sections or material properties, and the detected values are the following. For what concerns the real part in both fluid and solid domains the results trend gets near to those expected with the classic relation ρc. On the other hand, the values obtained for the imaginary part are one order of magnitude inferior to those of the real part, confirming the results already proved in the other chapters of this work for a straight tube geometry.

8 Conclusions

When this thesis work started, the studies conducted on this argument by the research team I joined were in a preliminary phase, testing some computational software able to model, catch and solve the main features and problems of the fluid-structure interaction between a solid matrix and the fluid phase permeating its pores.
With this purpose, exact analytical solutions, i.e. the Tijsseling and Skalak theories on water hammer waves for fluid filled pipes, have been found and adopted to compare the capacities of two software: the ANSYS CFD and Mechanical products, and LSDYNA. The latter resulted the most performing, becoming the decided numerical code for the solutions of the problems that this investigation would lead to.
The principal object of the research was to understand the influence of a porous soil's conformation on a pressure wave signal launched by a membrane through this fluid-solid structure, with particular interest on studying the impedance that the fluid filled ground exercised on this explorer wave. Many complex factors were composing this problem, affecting one another in different ways and not a priori estimable. A method for the evaluation of this parameter for these kind of domains, where the internal structure is not a priori predictable, had to be produced.
Conscious of the strong non-linearity of the problem that did not permit to superimpose the single effects, it has been decided to start from the basic elements forming the soil matrix and to analyze the effect that each one had on the quantity of interest: the acoustic impedance.
The study began with the analysis of the effect of simple geometry singularities, such as pores, constrictions or elbows in a single fluid channel ideally surrounded by a rigid body not reacting to the stresses exercised by the fluid on the interface. Since acoustic impedance is a function of frequency, input pressure waves were created each one with a different frequency to solicit the system with the aim of catching variations of its behavior.
Acoustic theory for sound in waveguides and channels has been adopted to prove the goodness of the results in terms of variations of the real and the imaginary parts of the acoustic impedance, according with other similar physic processes.
From this analysis a different behavior, with larger sound losses, is emerged for the frequency whose wavelength is comparable with the fluid domain dimensions.
In fact, as the wavelength of the signal tended to values similar to the channel diameter, the real part of the acoustic impedance became smaller, transforming a great part of the energy carried by the initial wave into dissipations, represented by the strong increasing of the imaginary impedance part. That's why, for those types of inspections, input signal wavelengths adopted need to be significantly different from the characteristic dimensions of the considered domains, in order to inspect with a single wave a larger portion of the desired material.
These results have been used as a measure of comparison for those obtained in the following part of this work, where the interaction between the fluid phase and the solid part has been added.

The elementary geometries modeled for the fluid analysis so far were now surrounded by an elastic solid matrix, in order to represent a single basic part of the porous soil.
Charging both the solid part and the fluid channel, two wave trains would superimpose creating resultant wave fields difficult to interpret. Therefore, a preliminary analysis of this case have been performed stressing the input surface of the fluid phase only.
This allowed to clearly understand the effect of the fluid perturbation on the solid matrix, and to obtain a solution comparable with the one detected in the previous fluid analysis.
Waves reflected by the singularities acted in most of the cases as those obtained from the fluid analysis but with different values, generating different acoustic impedance results.
Comparing the two solutions, one with a rigid body surrounding the fluid channels and the other with a reacting elastic solid interfacing with the same fluid geometries, it emerged that the pressure signal has higher losses in the FSI analysis for the real impedance part, which is the one transporting energy, in the order of 15%. This value, by the way, tended to decrease for the sections nearby the inspected singularities almost avoiding the differences between fluid and FSI approaches. Conversely divergences of even 20% are observable for sections where the domain is regular and no changes of cross-section properties are present.
Poisson effect, noticed in the FSI approach, produced precursor waves which summed to the fluid perturbations modifying the amplitudes observed.
Impedance phase variations also resulted of smaller entity, compared to the single fluid analysis, where the interaction between the solid and the fluid were imposed. This because of the different reaction to the incident waves between the rigid and the elastic boundaries: in the first case in fact more reflections which influenced the fluid pressure phase are generated.
Finally, as a further study, also the solid structure has been observed in addition to what done for the fluid phase.
The influence of different constraints and boundary conditions on the stress distributions in the solid matrix has been analyzed. In fact, constraining in a different way the inlet solid surface, different phenomena have been detected, as the initial transition phase in the solid domain due to the viscous fluid effect and the influence of the reflected waves on those imposed constraints on the solid and fluid stress distributions.
With regard to the precursor waves generated by the Poisson effect, the configuration with the input surface constrained only in the external corner node presented precursor waves with bigger amplitudes than the other tested constraints.
Those considerations are only part of a complete FSI analysis, which will be continued after this work, despite that it helped to better understand the interaction between fluid and solid parts subject to desired excitations.
This entire study has been conducted for fixed input frequency pressure waves and fixed domain dimensions. However, in order to simulate the system behavior under lower frequencies, these analysis can be useful also for domains with the same dimensional relation between, for example, the channel diameter and the wavelength of the input signal, and this could be the one of the further developments of this entire work.
The same considerations on the acoustic impedance can also be adopted for other similar fluid-solid structures, using this approach for other engineering purposes. This because the porous soil considered is only a sample of domain where a solid matrix and a fluid phase interact through an interface.

In conclusion, this is only a step into a long and difficult study to determine the acoustic impedance of a sample of porous soil. As we all know, to achieve the top of the stair, which is the final target, single steps have to be faced and completed, and this thesis aims to represent one of these steps, with the hope of being helpful to the team of my thesis relator.

9 References

[1] Kai Ming Li Keith Attenborough, *Predicting Outdoor Sound*. London and New York: Taylor & Francis, 2007.

[2] Frank J. Fahy, *Foundations of Engineering Acoustics*. Institute of Sound and Vibration Research, University of Southampton, Southampton, UK: Elsevier, 2001.

[3] S. Del Giudice, "Acoustic pipeline monitoring: theory and technology," Politecnico di Milano, 2014.

[4] C. Ianniello, L. Maffei G. Iannace, "Misura dell'impedenza acustica specifica normale di una superfice in campo libero mediante sequenze pseudocasuali periodiche," Università di Napoli, 1992.

[5] Society of Petroleum Engineers (SPE). PetroWiki. [Online]. http://petrowiki.org/PetroWiki

[6] Emanuela Gizzi, "Il fenomeno aeroacustico negli endoreattori a propellente solido," *Università degli studi di Roma La Sapienza*, 2009.

[7] Wikipedia.org. Wikipedia - Acoustic impedance. [Online]. http://en.wikipedia.org/wiki/Acoustic_impedance

[8] Sydney, Australia School of physics. Acoustic impedance, intensity and power. [Online]. http://www.animations.physics.unsw.edu.au/jw/sound-impedance-intensity.htm

[9] Sydeny, Australia School of physics. Acoustic compliance, inertance and impedance. [Online]. http://www.animations.physics.unsw.edu.au/jw/compliance-inertance-impedance.htm

[10] R. Skalak, "An extension of the theory of water hammer," New York, Columbia University, 1956.

[11] A. Tijsseling., E. Vardy L. Zhang, "FSI Analysis of liquid-filled pipes.," *Journal of Sound and Vibration*, 1999.

[12] Ke Yang, L. Zhang Q. S. Li, "Analytical Solution for Fluid-Structure Interaction in Liquid-Filled Pipes Subjected to Impact-Induced Water Hammer," *Journal of Engineering Mechanics*, 2003.

[13] A. S. Tijsseling, "Water hammer with fluid–structure interaction in thick-walled pipes," Eindhoven University of Technology, Eindhoven, 2007.

[14] A. S. Tijsseling D. Wiggert, "Fluid transients and fluid-structure interaction in flexible liquid-filled piping," American Society of Mechanical Engineers, 2001.

[15] A.S. Tijsseling, "Exact solution of linear hyperbolic four-equation system in axial liquid-pipe vibration," Department of Mathematics and Computer Science, Eindhoven University of Technology, Eindhoven, 2003.

[16] A.S. Tijssling C.S.W. Lavooij, "Fluid-Structure Interaction in liquid filled pipes system," The Netherlands and Delft University of Technology, 1991.

[17] A.G.T.J. Heinsbroek A.C.H. Kruinbrink, "Fluid-Structure Interaction in non-rigid

pipeline systems," Industrial Technology Division, Delft Hydraulics, 1992.

[18] A. S. Tijsseling, *Poisson coupling beat in extended water hammer theory*, Unibersity of Dundee, Ed. Dundee, UK, 1997.

[19] A. Tijsseling, A. R. Simpson, M. L. Stephens, J. P. Vitkovsky, A. Bergant, M. F. Lambert, "Skalak's extended theory of water hammer," *Journal of Sound and Vibration 310*, 2008.

[20] J. D. Achenbach, *Wave propagation in elastic solids*. Amsterdam - London: North Holland Publishing Company, 1973.

[21] K. F. Graff, *Wave Motion in Elastic Solids*.: Dover Pubblications, New York, 1975.

[22] Julius Miklowitz, *The theory of elastic waves and waveguides*. Amsterdam - New York - Oxford: North Holland Publishing Company , 1919.

[23] J. B. d'Alembert, *"Recherches sur la courbe que forme une corde tenduë mise en vibration"*., 1747.

[24] Inc. ANSYS, *ANSYS Mechanical Application User's Guide*., 2010.

[25] Inc. ANSYS, *"ANSYS CFX Solver Theory Guide"*., 2010.

[26] LIVERMORE SOFTWARE TECHNOLOGY CORPORATION LSTC, *"LS-DYNA Theory Manual"*., 2014.

[27] David H. Johnston, *Methods and Applications in Reservoir Geophysics*, David H. Johnston, Ed. Tulsa, U.S.A.: Society of Explorations Geophysicists, 2010.

Ringraziamenti

Durante i mesi di studio per la produzione di questo lavoro ho dovuto confrontarmi con situazioni, problemi ed imprevisti ogni volta diversi e non facilmente risolvibili. Da sportivo quale sono, ho considerato tutto ciò come un allenamento, in cui l'obiettivo di ogni giorno è spostare i propri limiti un po' più lontano. È proprio questo aspetto infatti che permette di ottenere non solamente risultati migliori, ma anche di temprare lo spirito ed abituarlo all'affrontare e ad accogliere la novità come un'occasione stimolante finalizzata al progresso.
Pertanto ringrazio il Prof. Passoni e l'Ing. Bozzi per questa opportunità di crescita e miglioramento personale concessami, per avermi trasmesso nuove conoscenze, e non ultimo per avermi fatto comprendere come affrontare le difficoltà incontrabili in campo ingegneristico.

Ringrazio l'Ing. Bizzozero, instancabile lavoratrice ed esempio per me durante questo periodo, l'Ing. Sturla e l'Ing. Votta per i consigli che hanno avuto la pazienza di fornirmi nei momenti di incertezza.

Per quanto riguarda i risultati e i metodi adottati in questo lavoro, essi non sono frutto della mera applicazione meccanica di un algoritmo, bensì di una serie di ragionamenti prodotti quotidianamente con lo scopo di comprendere al meglio le sfaccettature di un problema da risolvere, e perciò ne sono orgoglioso.

Come atto finale di un percorso estremamente formativo qui a Milano e al Politecnico, ringrazio le persone che più sono state presenti: Luca e Gianluca, i due compagni con cui ho condiviso ogni difficoltà incontrata ma soprattutto ogni soddisfazione ricevuta, Vincenzo, Giorgio e Roberto, con cui ho condiviso dei fantastici ricordi che porterò sempre con me, e i miei amici di Udine, in particolare Stefano, Claudio, Eleonora e Corinne, per i quali la lontananza ha rafforzato ancor più il rapporto.

L'alfa e l'omega di questo lavoro però sono i miei genitori, perché senza di loro non avrei mai avuto la fortuna di fare quello che ho fatto, né di essere quello che sono. Grazie.